UNIVERSITY OF CALIFORNIA, SAN DIEGO

**The imaging of nanostructures with novel x-ray methods**

A dissertation submitted in partial satisfaction of the
requirements for the degree
Doctor of Philosophy

in

Physics

by

Sebastian Dietze

Committee in charge:

Professor Oleg G. Shpyrko, Chair
Professor Eric E. Fullerton
Professor Ying Shirley Meng
Professor Ivan K. Schuller
Professor Sunil K. Sinha

2015

The dissertation of Sebastian Dietze is approved, and it is acceptable in quality and form for publication on microfilm and electronically:

_____

_____

_____

_____

_____

Chair

University of California, San Diego

2015

TABLE OF CONTENTS

LIST OF FIGURES

LIST OF TABLES

ACKNOWLEDGEMENTS

It is a pleasure to formally acknowledge and thank the many people who have made this possible. First, I would like thank my advisor, Professor Oleg Shpyrko, for his continuous support. I am grateful to have had the freedom to peruse my dreams. I would also like to thank my committee members, Professor Ivan K. Schuller, Professor Eric E. Fullerton, Professor Sunil K. Sinha, and Professor Ying Shirley Meng for their insight and advice. From them, I have learned a great deal more than the research presented in this dissertation.

In addition, I would like to thank my fellow graduate students and postdoctorates for their insightful discussions. In particular, I would like to thank Moses Marsh, Jong-Woo Kim, Dr. Andrej Singer, Leandra Boucheron, Siming Wang, Dr. Gabriel Ramírez, Dr. Edwin Fohtung, Dr. Jyoti Mohanty, Andrew Alvestad for the sleepless nights and hard work, without which the experiments would not have been possible. Several collaborators have help in this regard as well. In particular, the under appreciated staff at Advanced Photon Source of Argonne National Lab; Zhonghou Cai, Ian McNulty, and David Vine.

I would also like to thank my family for their support. I appreciate their encouragement that has gotten me this far. Finally, I would like to thank Veronica Burnett, for being their through the toughest times and reading through all of my work. She believed in me even when I doubted myself.

Chapter 4, in part, has been submitted for publication as it may appear in *J. Synchrotron Radiat.* (2015). S. H. Dietze and O. G. Shpyrko "Coherent diffractive imaging: Achieving atomic resolution." The dissertation author was the primary investigator and author of this paper.

Chapter 6, in large part, is a reprint of the material as it appears in S. H. Dietze, M. J. Marsh, Siming Wang, J.-G. Ramírez, Z.-H. Cai, J. R. Mohanty, Ivan K. Schuller, and O. G. Shpyrko. "X-ray-induced persistent photoconductivity in vanadium dioxide." *Phys. Rev. B* **90**, 165109 (2014) [1]. The dissertation author was the primary investigator and author of this paper.

## VITA

| | |
|---|---|
| 2008 | Bachelor of Science in Physics, University of Texas, Austin |
| 2008 | Elements of Computing, University of Texas, Austin |
| 2010 | Master of Science in Physics, University of California, San Diego |
| 2015 | Doctor of Philosophy in Physics, University of California, San Diego |

## PUBLICATIONS

**S. H. Dietze**, M. J. Marsh, Siming Wang, J.-G. Ramírez, Z.-H. Cai, J. R. Mohanty, Ivan K. Schuller, and O. G. Shpyrko. *Phys. Rev. B* 90, 165109 (2014). "X-ray-induced persistent photoconductivity in vanadium dioxide."

**S. H. Dietze** and O. G. Shpyrko, (Submitted 2015). "Coherent diffractive imaging: Achieving atomic resolution."

A. Tripathi, J. Mohanty, **S. H. Dietze**, O. G. Shpyrko, E. Shipton, E. E. Fullerton, S. S. Kim, and I. McNulty, *Proceedings of the National Academy of Sciences* 20, 13393 (2011). "Dichroic coherent diffractive imaging."

A. Ulvestad, H. M. Cho, R. Harder, J. W. Kim, **S. H. Dietze**, E. Fohtung, Y. S. Meng, and O. G. Shpyrko, *Applied Physics Letters* 104, 073108 (2014). "Nanoscale strain mapping in battery nanostructures."

J. W. Kim, S. Manna, **S. H. Dietze**, A. Ulvestad, R. Harder, E. Fohtung, E. E. Fullerton, and O. G. Shpyrko, *Applied Physics Letters* 105, 173108 (2014). "Curvature-induced and thermal strain in polyhedral gold nanocrystals."

A. Singer, M. J. Marsh, **S. H. Dietze**, V. Uhl, Y. Li, D. A. Walko, E. M. Dufresne, G. Srajer, M. P. Cosgriff, P. G. Evans, E. E. Fullerton, O. G. Shpyrko, *Phys. Rev. B* 91, 115134 (2015). "Condensation of collective charge ordering in Chromium."

ABSTRACT OF THE DISSERTATION

**The imaging of nanostructures with novel x-ray methods**

by

Sebastian Dietze

Doctor of Philosophy in Physics

University of California, San Diego, 2015

Professor Oleg G. Shpyrko, Chair

The use of x-rays to probe matter is an ever increasing popular technique due to their short wavelength that can achieve better than atomic resolution; chemical selectivity that permit the separation of material contributions; and tunable interaction strength allowing a wide class of materials to be probed including interfaced and bulk structures. As more powerful sources of x-rays have become available in the form of synchrotrons and linear accelerators, new and inventive experimental method have emerged to access the unknown. In this dissertation, three novel uses of x-rays are advanced to study a wide class materials.

Since the next generation of x-ray sources will feature highly brilliant x-ray beams, they will enable the imaging of local nanoscale structures with unprecedented resolution. A general formalism to predict the achievable spatial resolution

in coherent diffractive imaging (CDI), based solely on diffracted intensities, is provided. The coherent dose necessary to reach atomic resolution depends significantly on the atomic scale structure, where amorphous materials or disordered materials require less dose than crystalline materials. A reduction in dose can be larger than three-orders of magnitude as compared to the expected scaling for uniform density materials. Additionally, dose reduction for crystalline materials are predicted at certain resolutions based only on their unit cell dimensions and structure factors.

An extension of dichroic coherent diffractive imaging of thin films with perpendicular magnetic anisotropy is made from a uniform case to one that contains charge contributions. With the use of linear polarized x-rays near resonant edges, the charge and magnetic scattering can be reconstructed. First, an approximate manual separation is made before reconstruction to obtain the magnetic domains of a Au patterned GdFe multilayer thin film. This is then compared to a direct reconstruction using the two coherent modes contributed by the right-hand and left-hand circular polarization. These methods lead to very similar results for the magnetic domain reconstruction, proving the viability of this technique. Thus, dichroic CDI may be applied to a much wider class of materials than was previously possible.

Finally, persistent photocoductivity was induced during nano-diffraction. The resistivity of vanadium dioxide ($VO_2$) decreased by over one-order of magnitude upon localized illumination with x-rays at room temperature. Despite this reduction, the structure remained in the monoclinic phase and had no signature of the high-temperature tetragonal phase that is usually associated with the lower resistance. Once illumination ceased, relaxation to the insulating state took tens of hours near room temperature. However, a full recovery of the insulating state was achieved within minutes by thermal cycling. This behavior is consistent with random local-potential fluctuations and random distribution of discrete recombination sites used to model residual photoconductivity.

# Chapter 1

# Mathematical Formalisms

## 1.1 Table of constants, variables, and operators

**Table 1.1**: Frequently used constants

| | |
|---|---|
| $\pi$ | the irrational constant $3.14159\ldots$ |
| $i$ | the imaginary constant $+\sqrt{-1}$ |
| $r_e$ | classical electron radius, $1.6022 \times 10^{-19}\,\mathrm{C}$ |
| $e$ | Coulomb of electric charge, $2.8179 \times 10^{-15}\,\mathrm{m}$ |
| $c$ | speed of light, $2.9979 \times 10^{8}\,\mathrm{m\,s^{-1}}$ |
| $\hbar$ | reduced Planck constant, $6.5821 \times 10^{-16}\,\mathrm{eV\,s}$ |

**Table 1.2**: Frequently used variables

| | |
|---|---|
| $E$ | energy |
| $\lambda$ | wavelength |
| $\omega$ | angular frequency |
| $k$ | wavenumber |
| $n$ | index of refraction |
| $r$ | real space dimension, length |
| $q$ | Fourier space dimension, inverse length |

**Table 1.3**: Frequently used operators

| | |
|---|---|
| $\mathscr{F}$ | Fourier Transform or general wave propagator |
| $\mathscr{P}_Z$ | wave propagator along z-direction |
| $\sum_j$ | sum over index j |
| $\prod_j$ | product over index j |
| $\Re$ | real component |
| $\Im$ | imaginary component |
| $\mathbf{r}$ | tensor, usually a vector |
| $\hat{\mathbf{r}}$ | $\ell^2$ normalized vector |
| $\mathbf{r}^\top$ | transpose of tensor |
| $\mathbf{r}_\perp$ | perpendicular component |
| $\mathbf{r}_\parallel$ | parallel component |
| $\langle f \rangle$ | mean |
| $\lvert f \rvert$ | absolute value or square root of $\ell^2$-norm |
| $f^*$ | complex conjugate |
| $\mathcal{O}$ | order of magnitude |
| $\nabla$ | partial derivatives over all dimensions, operator |
| $\nabla^2$ | Laplacian operator |
| $\otimes$ | convolution operator |
| $\star$ | cross correlation operator |

## 1.2 Fourier transform and properties

A significant portion of this thesis makes use of the Fourier transform operator and its properties. For clarity, the necessary background is described here. The Fourier transform is defined as follows,

$$F(\mathbf{q}) = \mathscr{F}\left\{f(\mathbf{r})\right\} \equiv \int d\mathbf{r}\, f(\mathbf{r}) e^{-i\mathbf{q}\cdot\mathbf{r}}, \tag{1.1}$$

where $f(\mathbf{r})$ is a signal in real space and $F(\mathbf{q})$ is its corresponding frequency spectrum in Fourier space. The adjoint or inverse operator is given by,

$$f(\mathbf{r}) = \mathscr{F}^{-1}\left\{F(\mathbf{q})\right\} \equiv \tfrac{1}{2\pi} \int d\mathbf{q}\, F(\mathbf{q}) e^{i\mathbf{q}\cdot\mathbf{r}}. \tag{1.2}$$

Fourier transforms are linear operators such that,

$$aF(\mathbf{q}) + bG(\mathbf{q}) = \mathscr{F}\left\{af(\mathbf{r}) + bg(\mathbf{r})\right\}, \tag{1.3}$$

where $a$ and $b$ are complex constants. This has the consequence that, a constant phase factor, $a = e^{i\phi}$, may be multiplied to the signal without changing the spectrum's amplitude, $|F|$. As is clear from eq. (1.1), if the signal is multiplied by a constant phase ramp, $e^{i\mathbf{q}_0\cdot\mathbf{r}}$, the Fourier space coordinates are shifted by $\mathbf{q}_0$,

$$F(\mathbf{q} - \mathbf{q}_0) = \mathscr{F}\left\{f(\mathbf{r})e^{i\mathbf{q}_0\cdot\mathbf{r}}\right\}. \tag{1.4}$$

An equivalent translation of the signal can be obtained by multiplying a phase ramp to the spectrum, without changing its modulus. One additional trivial property can be obtained by taking the complex conjugate of eq. (1.1) and replacing $\mathbf{q} \to -\mathbf{q}$ then

$$F^*(-\mathbf{q}) = \mathscr{F}\left\{f^*(\mathbf{r})\right\}. \tag{1.5}$$

In other words, the spectrum is mirrored when appropriate complex conjugates are taken. Notice, that this has the consequence that if $f(\mathbf{r})$ is real, then $|F(\mathbf{q})| = |F(-\mathbf{q})|$ must be centrosymmetric. Finally, another straightforward property can be obtained using eq. (1.1) and integration by parts,

$$(iq_j)^n F(\mathbf{q}) = \mathscr{F}\left\{\frac{d^n f(\mathbf{r})}{dq_j^n}\right\}, \tag{1.6}$$

where $q_j$ represents a Cartesian component of $\mathbf{q}$. Extending the Fourier transform operator to vectors thus leads to $i\mathbf{q}F(\mathbf{q}) = \mathscr{F}\left\{\nabla f(\mathbf{r})\right\}$.

Some additional useful properties are stated here without proof. Firstly, we note Parseval's theorem,

$$\int d\mathbf{q}\,|F(\mathbf{q})|^2 = \int d\mathbf{r}\,|f(\mathbf{r})|^2. \tag{1.7}$$

This is a normalization conditional and as will be seen later implies conservation of photons for diffraction. Secondly, A very useful property is the convolution theorem, given by

$$\mathscr{F}\left\{f(\mathbf{r})g(\mathbf{r})\right\} = F(\mathbf{q}) \otimes G(\mathbf{q}) \equiv \int d\mathbf{q'}\,F(\mathbf{q'})G(\mathbf{q} - \mathbf{q'}). \tag{1.8}$$

A very similar expression can be obtained for the cross-correlation, to give another useful property, namely the Wiener-Khintchine theorem,

$$\mathscr{F}\left\{f^*(\mathbf{r})g(\mathbf{r})\right\} = F(\mathbf{q}) \star G(\mathbf{q}) \equiv \int d\mathbf{q'}\, F^*(\mathbf{q'})G(\mathbf{q}+\mathbf{q'}). \tag{1.9}$$

This immediately implies that when only the intensity of the frequency spectrum is known, the autocorrelation of the original function instead of function itself is directly known. Finally, Babinet's principle is noted, which can be seen from the linearity principle eq. (1.3) and noting that the Fourier transform of constant is, by definition, a scaled delta function, $a\delta(\mathbf{q}) = \mathscr{F}\left\{a\right\}$. Therefore, it is clear that the Fourier intensity of a signal and its complimentary signal, $1 - F(\mathbf{q})$, are the same except for at $q = 0$,

$$\left|\mathscr{F}\left\{1 - f(\mathbf{r})\right\}\right|^2 = \left|\delta(\mathbf{q}) - F(\mathbf{q})\right|^2 = \left|F(\mathbf{q})\right|^2 + G(q=0). \tag{1.10}$$

To make use of the Fourier transform algorithmically, it is necessary to define the discrete version. Given $\prod_{m=1}^{M} N_m$ samples in real space, $f_{j_1,\ldots,j_M}$, on an $M$-dimensional evenly spaced Cartesian grid with coordinates $x_{j_m} = j_m \delta x_m$, it is sufficient to describe these points using the Fourier coefficients $F_{k_1,\ldots,k_M}$, on an $M$-dimensional evenly spaced Cartesian grid with coordinates $q_{k_m} = k_m \delta q_m$, where $\delta q_m = 2\pi / N_m \delta x_m$ (see section 3.2). Using the Fourier transform definition (eqs. (1.1) and (1.2)), the discrete Fourier transforms (DFT) are given by,

$$F_{k_1,\ldots,k_M} = \prod_{m=1}^{M} \delta x_m \sum_{j_m=0}^{N_m} f_{j_1,\ldots,j_M} e^{-2\pi i k_m j_m / N_m} \tag{1.11a}$$

$$f_{j_1,\ldots,j_M} = \prod_{m=1}^{M} \tfrac{1}{N_m \delta x_m} \sum_{j_m=0}^{N_m} F_{k_1,\ldots,k_M} e^{2\pi i k_m j_m / N_m}. \tag{1.11b}$$

Although, these are often simplified further, this form is used here to emphasize appropriate units. The previously described properties of Fourier transforms still hold using the discrete version.

## 1.3 Vector identities

Some well known useful vector calculus identities are given here without proof, which will be used in later chapters.

$$\nabla \times \nabla \times \mathbf{A} = \nabla(\nabla \cdot \mathbf{A}) - \nabla^2(A) \tag{1.12}$$

$$\nabla \cdot (c\mathbf{A}) = \mathbf{A} \cdot \nabla c + c\nabla \cdot \mathbf{A} \tag{1.13}$$

$$\nabla \times (c\mathbf{A}) = \mathbf{A} \times \nabla c + c\nabla \times \mathbf{A} \tag{1.14}$$

## 1.4 Representing complex images

Complex images in this thesis are represented by the hsv-color space (fig. 1.1), where any complex number, $Ae^{i\phi}$, is expressed by an amplitude and phase. The value or intensity of the image is the amplitude, where low values are dark (center of fig. 1.1) and high values are bright. The hue of the image is the phase, such that any arbitrary color is $\phi = 0 = 2\pi$ and its complimentary color is $\pi$ shifted.

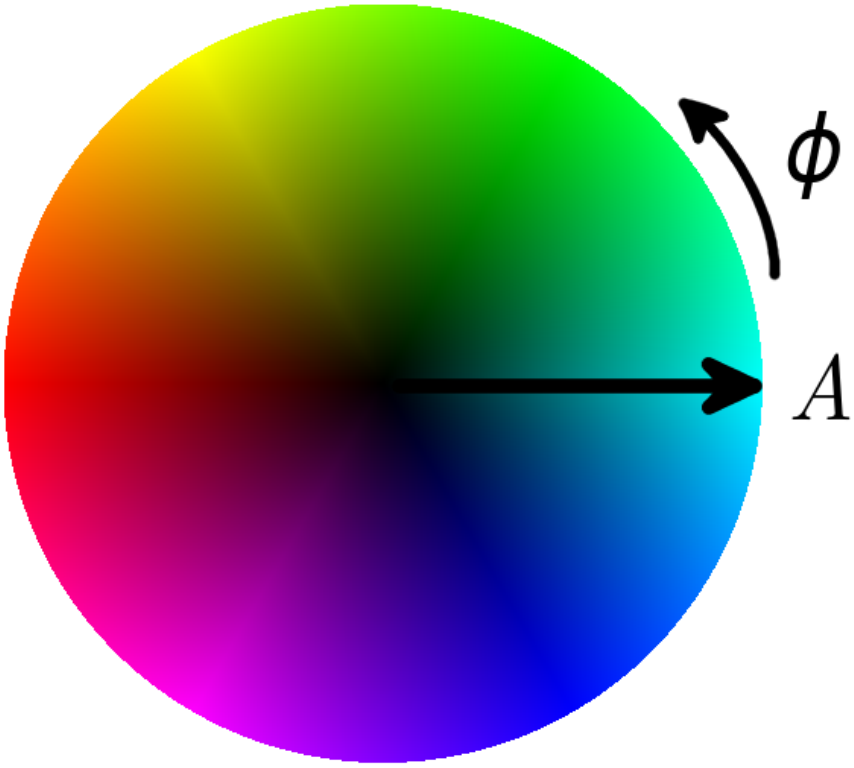


**Figure 1.1**: Color space to display complex images where amplitudes are given by the value or intensity and phase is given by the hue or color.

# Chapter 2

# Electromagnetic Interaction

## 2.1 Scalar wave equation

The most complete description of how electric fields $\mathbf{E}$ and magnetic fields $\mathbf{H}$ exist within matter containing free charge and magnetism is given by Maxwell's equation [2, 3]. In differential form in the International System of Units, these equations are written as

$$\nabla \cdot \mathbf{B} = 0, \tag{2.1a}$$

$$\nabla \cdot \mathbf{D} = \rho, \tag{2.1b}$$

$$\nabla \times \mathbf{H} = \mathbf{j} + \frac{\partial \mathbf{D}}{\partial t}, \tag{2.1c}$$

$$\nabla \times \mathbf{E} = -\frac{\partial \mathbf{B}}{\partial t} \tag{2.1d}$$

The derivation of the wave equation from Maxwell's equations can be found in almost any book on electrodynamics or optics [4, 5], which is reproduced here to emphasize the necessary assumptions. To proceed, consider what solutions exist in neutral materials, with no free charge, such that $\rho = 0$ and $j = 0$. In addition, assume that the electric and magnetic fields are weak enough in magnitude to induce a linear response of the material. Then, $\mathbf{D} = \epsilon\mathbf{E}$, where $\epsilon$ is the electric permittivity which in general is a matrix to account for effects such as birefringence. Similarly, $\mathbf{B} = \mu\mathbf{H}$, where $\mu$ is the magnetic permeability and again could be a matrix to account for Faraday rotation. For now, let this further be restricted to

isotropic materials, then Maxwell's equations simplify to a very symmetric form

$$\nabla \cdot (\mu \mathbf{H}) = 0, \tag{2.2a}$$

$$\nabla \cdot (\epsilon \mathbf{E}) = 0, \tag{2.2b}$$

$$\nabla \times \mathbf{H} = +\frac{\partial \epsilon \mathbf{E}}{\partial t}, \tag{2.2c}$$

$$\nabla \times \mathbf{E} = -\frac{\partial \mu \mathbf{H}}{\partial t}. \tag{2.2d}$$

Thus far, the spatial and time dependence of these variables has not been specified. Let the material variables $\epsilon$ and $\mu$ vary slowly in space and time compared to the electric and magnetic field solution. In other words, it is required that

$$\left| \frac{\partial \epsilon}{\partial t} \mathbf{E} \right| \ll \left| \epsilon \frac{\partial \mathbf{E}}{\partial t} \right| \tag{2.3a}$$

$$|\nabla \epsilon \cdot \mathbf{E}| \ll |\epsilon \nabla \cdot \mathbf{E}| \tag{2.3b}$$

$$|\nabla \epsilon \times \mathbf{E}| \ll |\epsilon \nabla \times \mathbf{E}| \tag{2.3c}$$

and similarly for the magnetic permeability and magnetic field. Taking the curl of eq. (2.2d), using the vector calculus identities eqs. (1.12) to (1.14), and eqs. (2.2b) and (2.2c) this becomes the wave equation,

$$\nabla^2 \mathbf{E} - \frac{n^2}{c^2} \frac{\partial^2 \mathbf{E}}{\partial t^2} = 0, \tag{2.4}$$

where $n = (\mu\epsilon/\mu_0\epsilon_0)^{1/2}$ is the refractive index and $c = (\mu_0\epsilon_0)^{-1/2}$ is the speed of light. An identical equation can be derived for $\mathbf{H}$ by starting with the curl of eq. (2.2c). Since these equations are true for any component of the electric and magnetic field independently, it is enough to consider a single component to obtain a scalar form. More commonly, this is written by looking at Fourier components in frequency space. Using $\tilde{\psi}(\mathbf{r}, \omega) = \mathscr{F}\{\psi(\mathbf{r}, t)\}$ and eq. (1.6), the Helmholtz equation is derived,

$$\nabla^2 \tilde{\psi} + k^2 \tilde{\psi} = 0, \tag{2.5}$$

where the wavenumber $k = n\omega/c$ and the refractive index is frequency dependent $n = n(\mathbf{r}, \omega)$. Notice, that this is identical to the time-independent Schrödinger equation, from which scattering can also be derived in a semiclassical perspective.

Although, the solution that exist for eq. (2.5) have not yet been found, suffice it to say the wave equation, as the name implies, has solutions that are wave-like. For instance, it is easy to see that a plane wave travelling along the z-direction, $\psi \propto e^{i(kz-\omega t)}$, is one solution when the refractive index is constant. More precisely, it is an exact solution in uniform, neutral, isotropic media without free charges and is approximately true when the wavelength, $\lambda = 2\pi/k$, is much smaller than variation in the electric permittivity and magnetic permeability. Similarly, the material should not change in time compared to $2\pi/\omega = 2\pi/k_0 c$.

## 2.2 Scalar diffraction

Many attempts have been made to find simple solutions to the Helmholtz equation for various boundary conditions, including monochromatic [6, 7, 8, 9] and a generalization to multichromatic using angular spectrum approach. The basis of these works starts by converting eq. (2.5) to it's integral form using Green's theorem such that the solution at any point $\mathbf{r}$ can be written in terms of solution on a given surface,

$$\tilde{\psi}(\mathbf{r}) = \int_S ds\, (G\frac{\partial\tilde{\psi}}{\partial\eta} - \tilde{\psi}\frac{\partial G}{\partial\eta}). \tag{2.6}$$

Selecting an appropriate Green's function, $G$, that also satisfies the homogeneous wave equation and making use of boundary conditions and special surfaces allows for a simple solution. Generally, the Green's function takes the form of a spherical wave, since it goes to zero at large distances allowing simple boundary conditions. It is necessary to assume that the field distribution, $\tilde{\psi}$, and/or its derivative, $\frac{\partial\tilde{\psi}}{\partial\eta}$, are zero at any material boundaries and that the field distribution is unchanged in free space compared to no boundaries being present. This is of course not strictly true, as EM radiation will interact with materials, but it is a good approximation when not looking too closely at the solution near boundaries. The first Rayleigh-Sommerfeld solutions reproduces Huygens-Fresnel principle,

$$\tilde{\psi}(\mathbf{r}_\perp, z) = \frac{-iz}{\lambda}\int_S d\mathbf{r}'_\perp\, \tilde{\psi}(\mathbf{r}'_\perp)\frac{\exp\left(ik|\mathbf{r}-\mathbf{r}'_\perp|\right)}{|\mathbf{r}-\mathbf{r}'_\perp|^2}, \tag{2.7}$$

where $|\mathbf{r} - \mathbf{r}'_\perp| = \sqrt{(x-x')^2 + (y-y')^2 + z^2}$. This expression can be thought of as each point in a wave-front creating a new spherical wave and coherently adding with appropriate phase factor.

This may also be written in terms of a convolution. Letting $\mathscr{P}_Z(\mathbf{r}'_\perp) = \frac{-iz}{\lambda}\frac{\exp\left(ik\left|\mathbf{r}'_\perp + z\hat{\mathbf{z}}\right|\right)}{\left|\mathbf{r}'_\perp + z\hat{\mathbf{z}}\right|^2}$ be a propagator that adjusts phase and amplitude to a wave starting at $\mathbf{r}' = \mathbf{r}'_\perp + z\hat{\mathbf{z}} = \mathbf{0}$, then eq. (2.7) becomes

$$\tilde{\psi}(\mathbf{r}_\perp, z) = \tilde{\psi}(\mathbf{r}'_\perp) \otimes \mathscr{P}_Z(\mathbf{r}'_\perp). \tag{2.8}$$

eqs. (2.7) and (2.8) describes the propagation of a field distribution, a wave created by a virtual source, due to boundaries such as apertures.

## 2.3 Modification by thin films

The propagation of a field is described by eq. (2.7) and can be considered as a weighted sum of the original field. It is obvious that the sum is dominated by regions where $z/|\mathbf{r} - \mathbf{r}'_\perp| \approx 1$. In other words, a significant contribution of the new field distribution is determined only by the original field distribution within a neighborhood of $|\mathbf{r}_\perp - \mathbf{r}'_\perp| \approx 2z$. In addition, the exponential term will reduce this, as it fluctuates rapidly for $|\mathbf{r}_\perp - \mathbf{r}'_\perp| > z$. Thus, if a field propagates through a thin film of thickness, $z$, the mixing of waves only occurs within this neighborhood and the exiting distribution is determined up to resolution of the order of the film thickness by a modification of the field at each location independently.

The previous considers a monochromatic wave propagating approximately in the $\hat{\mathbf{z}}$ direction. In this case, the field distribution may be written in the form $\tilde{\psi} = A(\mathbf{r})e^{ik_0 z}$, where $A(\mathbf{r})$, is a slowly varying function. The Helmholtz equation (eq. (2.5)) can then be rewritten as,

$$\nabla^2 A + 2ik_0\frac{\partial A}{\partial z} + k_0^2(n^2 - 1)A = 0. \tag{2.9}$$

Since $A$ is slowly varying, $\nabla^2 A \approx 0$. Thus an analytic solution exists, which determines how the thin film modifies the field distribution. In the case of x-rays, $n = 1 - \delta n$, such that $n^2 - 1 \approx -2\delta n$. Accounting for free space propagation, the

exiting field distribution is given by.

$$A(\mathbf{r}_\perp, z) = A(\mathbf{r}_\perp, z=0)\exp\left(ik_0\int_0^z dz\, n(\mathbf{r})\right)). \tag{2.10}$$

In this case, the entering field is modified by a projection or accumulation of the refractive index of the thin film. This description is most accurate when the variation in the projected refractive index is small, $\left|\int dz\, \nabla n(\mathbf{r})\right| \ll 1$. Or roughly speaking, it could be said that $|\nabla n(\mathbf{r})| \ll k$, which is the same condition as the wave equation to be valid. In practical terms, since x-ray are weakly interacting, eq. (2.10) is valid when the film is thinner than roughly 1 µm when not interacting resonantly.

## 2.4 Small angle propagation to near and far field

Although, eqs. (2.7) and (2.8) are quite general when considering wave propagation, a much simpler form can be arrived at when considering propagation distances much larger than the characteristic size of the field distribution, $z >> r'_{max}$. In this case, $|\mathbf{r} - \mathbf{r}'_\perp|^2 \approx r^2$ and $|\mathbf{r} - \mathbf{r}'_\perp| \approx r + r'^2_\perp/2r - (xx' + yy')/r$. Then, eq. (2.7) can be written as,

$$\tilde{\psi}(\mathbf{r}_\perp, z) = \frac{-iz}{\lambda r^2}e^{ikr}\int d\mathbf{r}'_\perp\, \tilde{\psi}(\mathbf{r}'_\perp)e^{ikr'^2_\perp/2r}e^{-i(z/r)\mathbf{q}_\perp\cdot\mathbf{r}'_\perp}, \tag{2.11}$$

where $\mathbf{q}_\perp = \frac{k}{z}\mathbf{r}_\perp$. This is considered the Fresnel approximation which calculates wave propagation to the near field. eq. (2.8) has no equivalent in this limit since a convolution cannot be restricted in this manner. However, a very useful approximation is the small angle limit, $r' \approx z$, since forward propagating waves are of interest here. Thus, this is directly applicable for low divergence beams and the propagation of waves cut by apertures. Then eq. (2.11) further reduces to

$$\tilde{\psi}(\mathbf{r}_\perp, z) = \mathscr{F}_{\mathbf{r}'_\perp\to\mathbf{q}_\perp}\left\{\tilde{\psi}(\mathbf{r}'_\perp)\right\} \otimes \tilde{\mathscr{P}}_Z(\mathbf{q}_\perp), \tag{2.12}$$

with $\tilde{\mathscr{P}}_Z(\mathbf{q}_\perp) = \mathscr{F}\left\{\mathscr{P}_Z(\mathbf{r}'_\perp)\right\} = -i\exp\left(ikz[1 - \frac{q_\perp^2}{2k^2}]\right)$. This is equivalent to eq. (2.8) with the Fresnel propagator $\mathscr{P}_Z(\mathbf{r}'_\perp) = \frac{-i}{\lambda z}\exp\left(ikz[1 + \frac{r'^2_\perp}{2z^2}]\right)$. Numerical propagation of fields are based off of eqs. (2.8) and (2.12) and called angular

spectrum method and direct method, respectively [10, 11, 12]. It is noteworthy that the quadratic phase term in the propagator may also be interpreted as part of the fractional Fourier transform [13].

When the propagation of the wave is extremely far, such that the Fresnel number $r'^2_{max}/z\lambda \ll 1$ then the diffraction is considered to be in the Fraunhofer regime or far field. In this case $kr'^2_{\perp}/2r \ll 2\pi$ such that this exponential term in eq. (2.11) becomes approximately unity. The propagation is then a single Fourier transform. As an example a plane wave with wavelength 1 nm is propagated through an aperture. At $z = 0$ or Fresnel number $F = \infty$, immediately after the aperture, the wave simply takes the shape of the aperture (fig. 2.1 (a)). At a distance of $z = 100\,\mu\text{m}$, $10^5$ times the wavelength, the distribution of the wave strongly resembles the original (fig. 2.1 (b)). At a distance of $z = 2\,\text{mm}$, the wave distribution is still recognizable to have come from the aperture, but there is significant cross interference (fig. 2.1 (c)). In the far-field limit, the wave is represented by its Fourier spectrum (fig. 2.1 (d)).

## 2.5 Born approximation

The solution to the Helmholtz equation (eq. (2.5)) and it's equivalent semi-classical description, the time-independent Schrödinger equation, can also be solve by using the method of Green's functions when a wave interacts with a localized materials, instead of propagating through an aperture (section 2.2). Thus, the integral form of the Helmholtz equation is the Lippmann-Schwinger equation. Since the most general Green's function that are appropriate here are spherical and plane waves, the solution is given by

$$\psi(\mathbf{r}) = \psi_0(\mathbf{r}) - \frac{k_0}{4\pi\hbar c}\int d^3\mathbf{r}'\,\frac{e^{ik_0|\mathbf{r}-\mathbf{r}'|}}{|\mathbf{r}-\mathbf{r}'|}V(\mathbf{r}')\psi(\mathbf{r}'), \tag{2.13}$$

where $\psi_0 = Ae^{ik_0 z}$ is the free space solution and the potential can be equated with the index of refraction, $V(\mathbf{r}) = \hbar c k_0(n^2(\mathbf{r}) - 1)$. Since, this is a transcendental equation, this cannot be solved directly. However, for small potentials, it can be solved iteratively, by starting with the free space solution on the right-hand

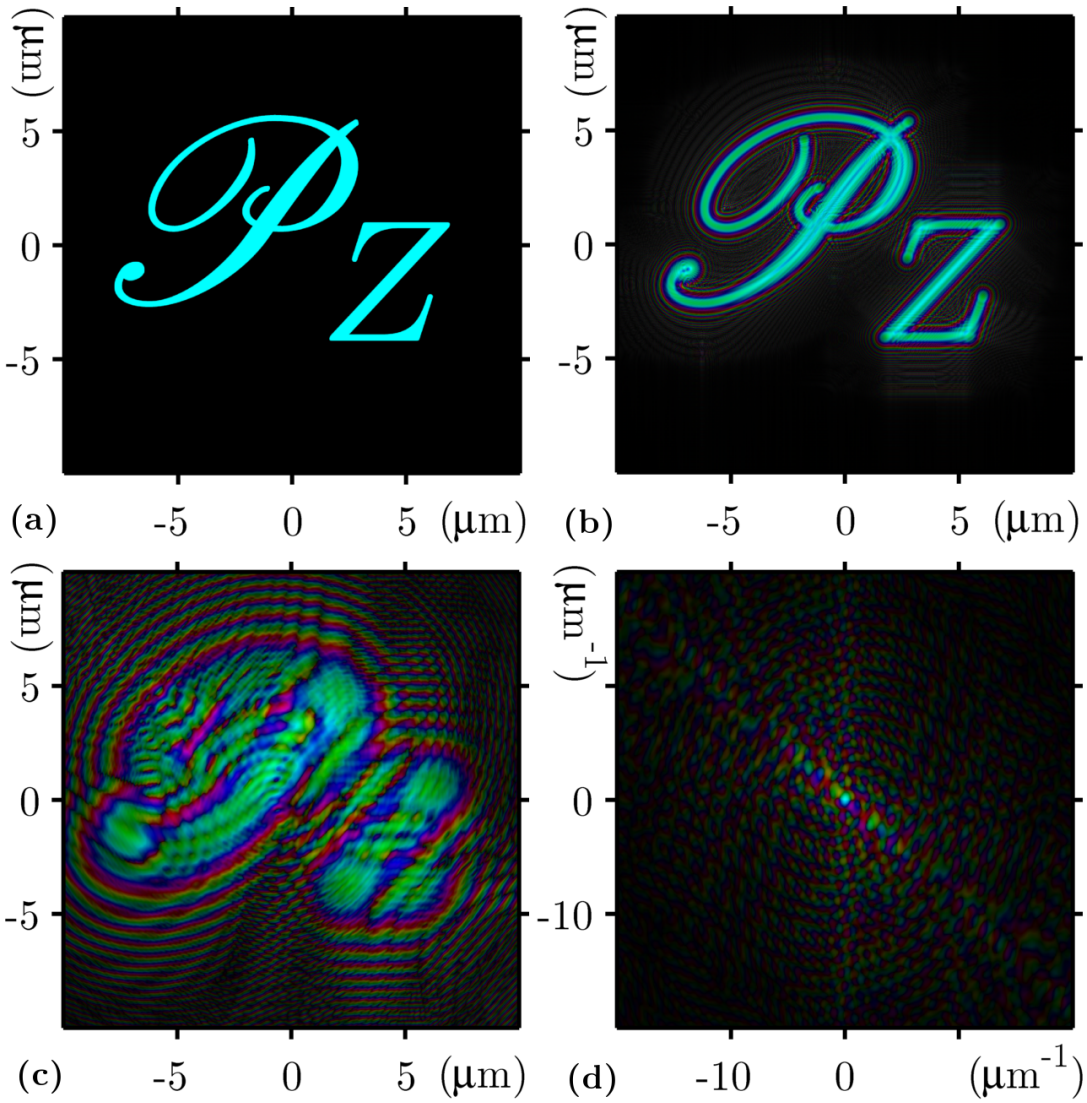


**Figure 2.1**: Propagation of a plane wave with wavelength 1 nm through an aperture, where amplitude is on square root scale and the complex image is displayed using hsv colorscale. (a) The wavefield just after the aperture $z = 0$ with Fresnel number $F = \infty$; (b) propagated a distance $z = 100\,\mu\text{m}$, $F = 640$; (c) $z = 2\,\text{mm}$, $F = 32$; and (d) in the far field limit $z = \infty$, $F = 0$

side. In the context of a scattering experiment, eq. (2.13) represents a plane wave that is illuminating a target, which produces a set of spherical waves. When the scattering far from the target is desired, such that the far-field condition holds, the translated spherical waves can be approximately express by spherical waves with an additional phase offset. Thus, eq. (2.13) can be written as

$$\psi(\mathbf{r}) \approx Ae^{ik_0 z} - \frac{Ak_0}{4\pi\hbar c}\frac{e^{ik_0 r}}{r}\int d^3\mathbf{r}'\, e^{-i\mathbf{q}\cdot\mathbf{r}'}V(\mathbf{r}'). \tag{2.14}$$

This is the first Born approximation [14, 5]. Thus the scattering is a sum of spherical waves, the same as given by Huygens-Fresnel. It represents the limit of a very weakly interacting material, such that the incoming beam is neither significantly attenuated nor do the photons scatter more than once.

## 2.6 Thomson and Rayleigh scattering

The scattering of electromagnetic radiation can be directly linked to a classical explanation. Any charged particle in the presence of an electromagnetic field will accelerate, due to the Lorentz force. The resulting electric dipole moment of the charged particle will in turn radiate itself such that some of the power from the incoming radiation is redirected [15]. When the particle is in free space and much smaller than the wavelength of radiation, the Thomson differential scattering cross section is

$$\frac{\mathrm{d}\sigma}{\mathrm{d}\Omega} = \left(\frac{-e^2}{mc^2}\right)^2 P, \tag{2.15}$$

where $P = \left|\hat{\boldsymbol{\epsilon}}_f^* \cdot \hat{\boldsymbol{\epsilon}}_i\right|^2$. There are two important points to note about this formula. First, this has a polarization term that was previously ignored in the scalar diffraction theory, where $\hat{\boldsymbol{\epsilon}}_i$ and $\hat{\boldsymbol{\epsilon}}_f$ are the incoming and outgoing radiation polarizations, respectively. Secondly, the cross section is inversely proportional to the particles rest mass. Although protons and electrons have the same charge magnitude, since the proton is roughly one thousand times heavier, the scattering from a material can then be considered to be exclusively from electrons.

Electrons are, however, generally not free and are instead bound to nuclei in the form of atoms. This has several consequences. First, the illumination of

bound electrons can be most simply be described as a driven harmonic oscillator system. Such a system has a well known solution, such that the Thomson cross section is modified by a resonant term,

$$\frac{\omega^4}{(\omega_0^2 - \omega^2)^2 + (\gamma\omega)^2}, \tag{2.16}$$

where $\omega_0$ are characteristic oscillation frequencies and $\gamma$ is the damping rate of the oscillator. In the limit of strong binding as compared to the photon energy, Rayleigh scattering is reproduced, which is most famous for explaining the color of our sky. A more complete description of resonant (anomalous) scattering is derived by treating the atom as a quantum mechanical system. Such a system will have discrete energy level (shells) for electrons to exist, such that absorbed energy can excite electrons to a higher shell or into the continuum at certain thresholds. Finally, since atoms have finite size, the scattered radiation from each electron will become increasingly out of phase with increasing scattering angle compared to the incoming radiation. It is thus convenient to considered scattering from atoms instead of individual electrons. Using the first Born approximation, the "kinematic" scattering is given by a sum over all atoms in the system,

$$F(\mathbf{q}, E) = -\frac{r_e}{R} \sum_m^{\text{atoms}} f_m(\mathbf{q}, E) e^{-i\mathbf{q}\cdot\mathbf{r_m}}, \tag{2.17}$$

where $r_e = \frac{e}{m_e c^2}$ is the classic electron radius and $\mathbf{q} = \mathbf{k}_f - \mathbf{k}_i$ is the wavevector transfer. The scattered intensity is $I(\mathbf{q}) = I_0 |F(\mathbf{q})|^2 P(\mathbf{q})$. The factor, $f(\mathbf{q}, E) = f^0(\mathbf{q}) + f'(E) + if''(E)$, contains all the information of the atomic structure and resonances. The first term is the atomic form factor, which in the limit of forward scattering goes to Z, the atomic number. The primed terms are the dispersive corrections, where $f'$ and $f''$ describe refraction and absorption in the system. Since the resonant features of $f(\mathbf{q}, E)$ are specific to each atom, this gives x-ray scattering a unique capability of separating contributions from different atom types.

When considering transmission through a material (eq. (2.10)) and forward projection of the Born approximation (eq. (2.14)), the scattering factors can be related to the complex index of refraction, such that

$$n(\omega) = 1 - \delta + i\beta = 1 - \frac{r_e \lambda^2 N}{2\pi} f(q = 0, E = \hbar\omega), \tag{2.18}$$

where $N$ is the atomic density of the material. Thus the scattering factors can be measured by measuring the absorption through a material and by use of the Kramers-Kronig relation [16].

## 2.7 Scattering from crystals

The kinematic scattering equation (eq. (2.17)), is sufficient to describe scattering from any collection of atoms, where the radiation interaction is weak. However, an even simpler form can be given when atoms are arranged in a periodic fashion such as crystalline materials. In this case, the positions can be given as $\mathbf{r}_m = \mathbf{R_n} + \mathbf{S}_j$, where $\mathbf{R_n} = \sum_k^3 n_k \mathbf{a}_k$ is the Bravais lattice vector given in terms of the primitive vectors that describes the location of a unit cell and $\mathbf{S}$ is the basis vector which describes the location of atoms within a unit cell [17]. The kinematic scattering is then written as

$$F(\mathbf{q}, E) = -\frac{r_e}{R} \sum_j^{\text{primitive}} f_j(\mathbf{q}, E) e^{-i\mathbf{q}\cdot\mathbf{S_j}} \sum_n^{\text{cells}} e^{-i\mathbf{q}\cdot\mathbf{R_n}}. \tag{2.19}$$

When the crystal has infinite size, the sum over all of the cells is only non-zero at very specific locations, $\mathbf{Q}_{hkl} = h\mathbf{b}_1 + k\mathbf{b}_2 + l\mathbf{b}_3$. In other words, the scattering consists of sharp peaks, known as Bragg peaks, at locations of the reciprocal lattice, whose cell is described by the vectors $\mathbf{b}_i = 2\pi \frac{\mathbf{a}_j \times \mathbf{a}_k}{\mathbf{a}_j \cdot (\mathbf{a}_j \times \mathbf{a}_k)}$. The sum over the primitive cell is known as the structure factor, $S(\mathbf{q})$, and gives the amplitude at each Bragg peak. Thus, by measuring the location and intensities of the Bragg peaks, the periodic structure can in principle be recovered, which is the aim of crystallography.

When the crystal is of finite size, the crystal can be described by an infinite periodic structure multiplied by a shape function, $C(\mathbf{r})$, which is one inside the crystal region and zero outsize. The scattering is then given by

$$F(\mathbf{q}, E) = -\frac{r_e}{R} \sum_{hkl} S(\mathbf{Q}_{hkl}) \tilde{C}(\mathbf{q} - \mathbf{Q}_{hkl}), \tag{2.20}$$

where $\tilde{C}(\mathbf{q}) = \mathscr{F}\{C(\mathbf{r})\}$, which falls off rapidly away from $q = 0$ with approximate width given by the inverse size of the crystal. Since the inverse size of the crystal is

almost always much smaller than the Bragg peak separations, the Bragg intensities contain very little interference between each other.

## 2.8 Coherence

Diffraction implies that there is a specific phase relationship between different regions, from which scattering occurs. The free space waveform is $\psi(\mathbf{r},t) = A(\mathbf{r},t)e^{-i\omega t}$, where $A(\mathbf{r},t)$ is the envelope, a slowly varying complex amplitude. The coordinates here represent the surface of all amplitudes that are produced from a single sources at a given time. It is equivalent to describe the envelope with volume coordinates and to remember that some coordinates are connected by the propagation of the wave through time and space. The scattered intensity from a collection of scatterers can be expressed as

$$I(\mathbf{q}) = \sum_j I(\mathbf{r}_j) + \sum_{j\neq k} \Gamma(\mathbf{r}_j, \mathbf{r}_k). \tag{2.21}$$

The first part is an incoherent sum of average intensities from each scatterer, with $I(\mathbf{r}_j) = \langle |A(\mathbf{r}_j)|^2 \rangle$. The average is in general an ensemble average, but can be taken as a time average for ergodic systems. The second sum contains information due to correlations, where $\Gamma(\mathbf{r}_j, \mathbf{r}_k) = \langle A^*(\mathbf{r}_j)A(\mathbf{r}_k)\rangle e^{i\mathbf{q}\cdot(\mathbf{r}_j-\mathbf{r}_k)}$ is the mutual coherence function. Although a complete description of coherence is not derived here, it is noted that the complex degree of coherence, $\gamma(\mathbf{r}_j, \mathbf{r}_k) = \frac{\Gamma(\mathbf{r}_j,\mathbf{r}_k)}{\sqrt{I(\mathbf{r}_j)I(\mathbf{r}_k)}}$, is a measure of how the complex amplitudes are synced in space and time [18]. When $\mathbf{r}_j = \mathbf{r}_k$, this is equal to one, otherwise it is between zero and one, by Schwarz's inequality. The complex degree of coherence is a useful measure, as it gives the coherence length, the separation over which interference is possible. It is also related to the interference fringe visibility, a measure of coherent scattering compared to an incoherent background.

It is useful to consider the coherence far away from a narrowband, finite sized source, as is the case for x-ray radiation used for diffraction. Using the Van Citteret-Zernike theorem [19, 20], the transverse, or spatial, coherence length can

be given as

$$l_{\perp} \approx \frac{\lambda_0}{\Delta\theta}, \tag{2.22}$$

where $\lambda_0$ is the mean wavelength of the radiation and $\Delta\theta$ is the apparent angular size of the source. This can alternatively be obtaining from the smallest source that can be resolved from Heisenberg's uncertainty principle and can be measured by Young's double slit experiment. Below approximately 15 keV, third generation synchrotron sources can obtain coherence lengths on the order of 100 µm and 5 µm in the vertical and horizontal directions, respectively [21].

Similarly, given the statistical nature of the bandwidth, the longitudinal, or temporal, coherence length can be found

$$l_{\parallel} = w\frac{\lambda_0^2}{\Delta\lambda}, \tag{2.23}$$

where $\Delta\lambda$ is the full-width at half maximum of the wavelength distribution and $w$ is a constant determined by the distribution type. For a Gaussian line, $w = \sqrt{\frac{2\ln 2}{\pi}}$, while for a Lorentzian line, $w = \frac{1}{\pi}$, thus it is usually sufficient to approximate this constant as one half. This is equivalent to the length where two waves, with a difference in wavelength, become phase shifted by $\pi$, as given by a Michelson interferometer. Hard x-ray beams use Bragg diffraction as a monochromator, such that the Darwin width determines the energy resolution, typically near $\Delta E = 10^{-4}E$. The longitudinal coherence length is then roughly 1 µm.

For crystallography, it is unnecessary to have such a large coherence length. For instance, in a highly ordered crystals, the coherence length only needs to be larger than a few unit cell dimensions, easily achievable by rotating anode tube sources, which have coherence lengths on the order of 50 nm. When illuminating a large crystal, the scattering between different coherence volumes is incoherent. Thus, the effect is akin to illuminating a large number of independent crystals of size equal to the coherence volume, which will determine the Bragg peak widths. Due, to the large number of coherence volumes, the fringe visibility of each peak is greatly reduced. On the other hand, there are several techniques (coherent diffractive imaging, holography, photon correlation spectroscopy) where the coherence needs to be very high, such that the correlation between points in the entire illuminated volume can be determined.

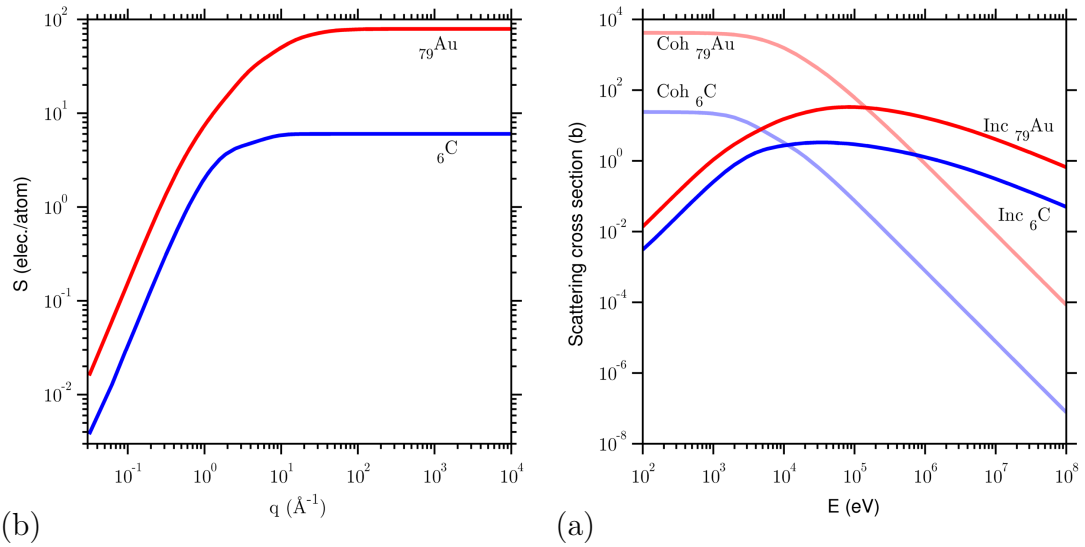


**Figure 2.2**: Examples of Carbon and Gold (reproduced from [23]) (a) the incoherent scattering function which account for binding of electrons in atoms and (b) showing the coherent and incoherent cross sections for photons.

## 2.9 Compton scattering

When considering the scattering of photons, it is also important to consider the process of energy transfer. It is well known that a photon can inelastically scatter from a particle such that the scattered photon energy is

$$E' = \frac{E_0}{[1 + \varepsilon(1 - \cos\theta)]}, \tag{2.24}$$

where $\theta$ is the scattering angle and $\varepsilon = \frac{E_0}{mc^2}$. This is known as Compton scattering, which is an incoherent process. For electrons, the rest mass energy is $mc^2 = 511$ keV and thus the energy transfer is very low when considering photon energies well below 100 keV. The Klein-Nishina differential cross-section [22], calculated for free electron Compton scattering is given by,

$$\frac{d\sigma_{KN}}{d\Omega} = \frac{r_e}{2[1 + \varepsilon(1 - \cos\theta)]^2}\left[1 + \cos^2\theta + \frac{\varepsilon^2(1 - \cos\theta)^2}{1 + \varepsilon(1 - \cos\theta)}\right]. \tag{2.25}$$

When taking electron binding into account in atoms [23], the atomic incoherent cross-section can be written as

$$\sigma_{KN} = \int d\sigma_{KN}(\theta) S(\theta, E), \tag{2.26}$$

where $S$ is the incoherent scattering function, which corrects binding at low photon energies. In the limit $q \to 0$, $S \to 0$ and for $q \to \infty$, $S \to Z$, the atomic number. Two examples have been show (fig. 2.2a) for carbon and gold, a light and heavy element receptively. A comparison of the coherent and incoherent total scattering cross sections (fig. 2.2b) shows that for heavy elements, incoherent scattering is minimal below 20 keV. On the other hand, for light elements, incoherent scattering, may become significant at as low as 2 keV and should be subtract for quantitative analysis, particularly when resolution better than 1 nm is desired.

## 2.10 Absorption

In section 2.6, it was noted that the scattering factor is complex due to binding of electrons in atomic shells. This leads to absorption of photons by the atomic system. The energy of this absorbed radiation goes into the excitation of an electron, either into the continuum or to a higher shell, if a very specific photon energy is used. The absorption cross section is quite large, dominating all other cross sections below roughly 50 keV. However, this is usually not a problem as it leads to characteristic fluorescence emission, which has lower energy than the incident radiation. Since fluorescence is of lower energy, it can easily be absorbed and only the surface contributes to this emission, which radiates evenly into the entire $4\pi$ solid angle. Although, the fluorescence can be measured and is extremely useful in determining local material structure, it generally does not spoil the coherent scattering signal as it is either too weak, can be further reduced with absorption, or subtracted during analysis.

## 2.11 Thermal diffuse scattering

Thus far, the assumption of scattering has been that the object is completely static. This is of course not true, since atoms are in constant motion, even at absolute zero temperature. The total intensity measured will be an incoherent sum of each instantaneous time snap shot, which is proportional to a time averaged

intensity. This type of analysis is relevant for any type of motion; however, here the motion in solids is considered, where the time averaged atomic positions are fixed, such that $\mathbf{r}_m(t) = \mathbf{R}_m + \mathbf{u}_m(t)$ and $\langle \mathbf{r}_m \rangle = \mathbf{R}_m$. The displacement amplitude of atoms is temperature dependent and roughly less than ten percent of the interatomic distance, when the material is in solid form. The scattered intensity is then [24, 25]

$$\begin{aligned} I =& \left| \sum_m f_m(q,E) e^{-M_m} e^{-i\mathbf{q}\cdot\mathbf{R}_m} \right|^2 \\ &+ \sum_{m,n} [f_m(q,E) e^{-M_m} e^{-i\mathbf{q}\cdot\mathbf{R}_m}][f_n^*(q,E) e^{-M_n} e^{i\mathbf{q}\cdot\mathbf{R}_n}](1 - e^{q^2\langle u_{m\parallel} u_{n\parallel}\rangle}). \end{aligned} \tag{2.27}$$

The first term is the coherent scattering from a static collection of atoms, attenuated by the Debye-Waller (DW) factor, $M_m = q^2\langle u_{m\parallel}^2 \rangle/2$, where $u_{m\parallel}(t) = \hat{\mathbf{q}} \cdot \mathbf{u}_m(t)$ is the change in atomic position projected along the scattering wavevector direction. The DW factor is a Gaussian smearing of the electron density of each atom due to thermal motion. It is frequently combined with the atomic form factor to create a temperature dependent form factor.

Since the total number of atoms in the system does not change, the total Fourier intensity is also conserved by Parseval's theorem (eq. (1.7)). Thus, the missing photons due to the DW factor in the coherent scattering, are scattered elsewhere. This is given by the second term in eq. (2.27), which is considered the thermal diffuse scattering (TDS). The term $\langle u_{m\parallel} u_{n\parallel} \rangle$ represents a correlation of the atomic motions, which encodes information about phonons. As an example, the scattering from a one dimensional periodic structure made of point atoms is show in fig. 2.3. When the atoms are static (fig. 2.3 black line), the scattering is given by strong Bragg peaks, whose width are proportional to the inverse particle size, without additional TDS. When the atoms have uncorrelated random motion (fig. 2.3 blue dashed line), the speckle visibility is reduced, where higher order Bragg peaks are attenuated by the DW factor. When phonons are present (fig. 2.3 red dashed line), correlations exist. A phonon is a periodic modification of the atomic lattice and will produce satellite peaks near the Bragg peaks, much like in the static deformation of charge density waves. Since many phonon modes exist,

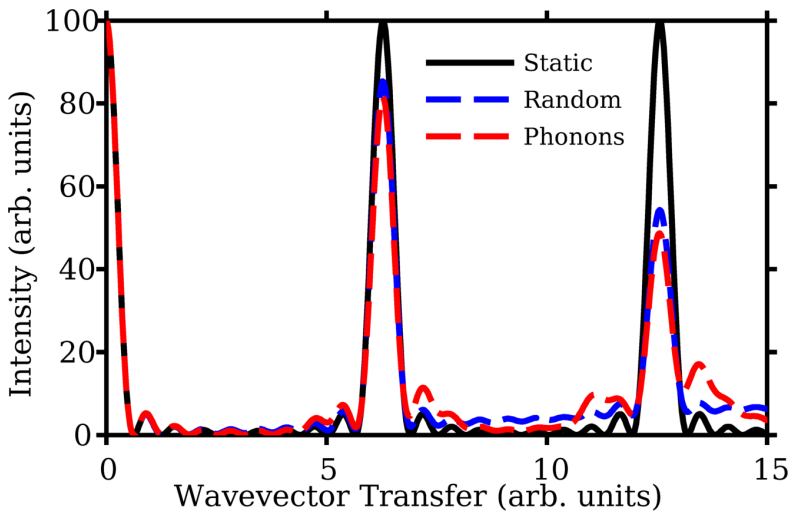


**Figure 2.3**: Thermal diffuse scattering. The scattering from a static one dimensional periodic atomic structure (black line) gives strong Bragg peaks. When the atoms have uncorrelated random motion (blue dashed line), the speckle visibility is reduced, where higher order Bragg peaks are attenuated by the DW factor. When phonons are present (red dashed line), correlations exist and additional intensity appears between Bragg peaks.

over time they produce additional broad incoherent intensity near the Bragg peaks.

Roughly speaking, the ratio of maximum intensity from TDS to coherent scattering is $\frac{E_p}{E_\mu}$, the ratio of phonon energy to the rest mass energy of the atoms. This is quite small for wavevector transfers below the inverse interatomic distance, in the range of $10^{-7}$ to $10^{-5}$. However, given sufficient flux, TDS can easily be measured between Bragg peaks of crystalline materials, and can be used to fit theoretical phonon modes given by dispersion curves [26, 27].

# Chapter 3

# Phase Retrieval

## 3.1 Phase problem

Traditional microscopes use optics to create an image from the illumination of an object. For x-rays, particularly "hard" x-rays with energy greater than 4 keV, matter has a refractive index near one and x-rays can penetrate easily. Thus, aberration free optics are difficult to manufacture at desired resolutions and can quickly degrade with exposure. Coherent diffractive imaging (CDI) is a type of microscopy that makes use of coherent radiation to image an object by diffraction. The objective lens is removed and a diffraction pattern is collected, instead of a real space image. For coherent radiation, the relationship between the wavefield at the sample and detector is straight forward and described by diffraction theory. If the full wavefield is known at the detector, a back propagation to the object is trivial. However, since detectors can only measure the intensity of the field at the detector plane and not the phase information, an immediate propagation to the object plane cannot be made. In fact, the phase information is at least as important as the intensity information since it encodes the curvature of the wave, and thus the direction it came from. To illustrate this, two images representing the projection of an object, are propagated to the far field. Their phases are then switched and an inverse propagation is done (fig. 3.1). It is clear that the two images appear mostly switched. This is because the phase information contains the wavefront distortion or in which direction the photons are traveling. To accurately determine

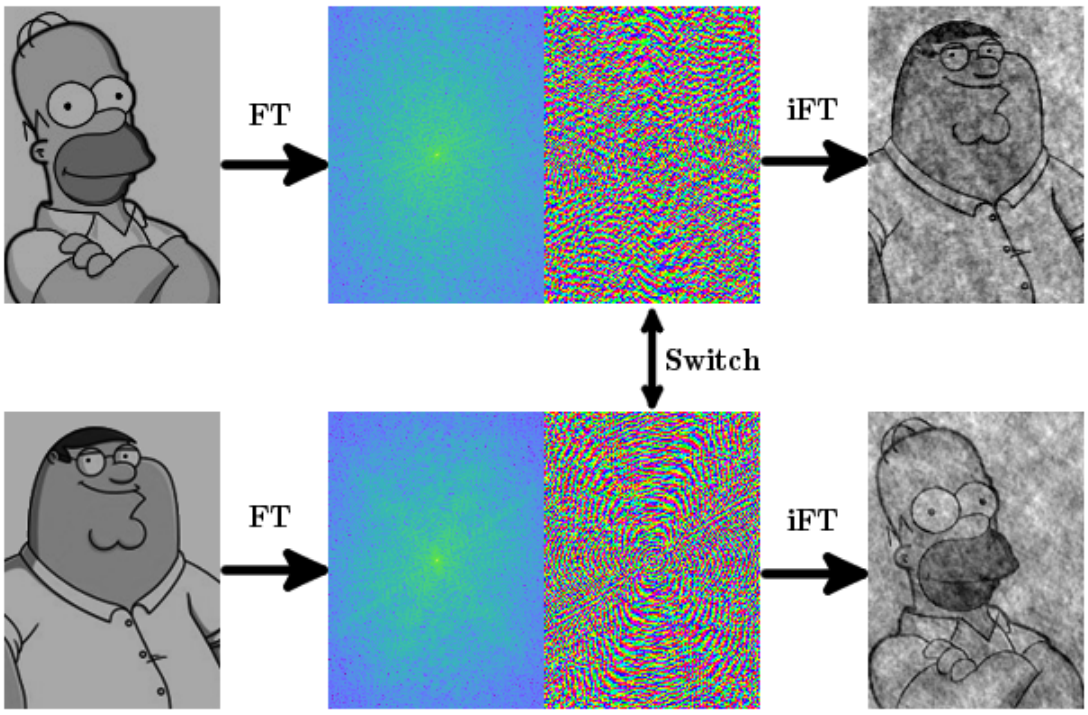


**Figure 3.1**: Two images, in this case Homer Simpson from The Simpsons and Peter Griffin from Family Guy, are propagated to the far field via Fourier transform where the wavefield is complex, containing amplitude and phase. If the phases are switched and the complex wavefield is propagated back, the two images appear mostly switched showing the phase is very important in order to know the object from which scattering occurred.

the object, the complementary phase information to the measured intensity must be determined. This type of nonlinear and non-convex problem is considered to be of great difficulty, as it requires the recovery of a vary large number of variables.

## 3.2 Sampling and uniqueness

It is well known that in order to maintain fidelity of a signal, a sufficient sample-rate must be used to accurately describe a bandlimited frequency spectrum without artifacts [28, 29]. In other words, if the frequency spectrum of a signal contains no amplitude beyond a frequency $\omega_m$, the signal is adequately represented when sampled at a rate of $\frac{\pi}{\omega_m}$. This statement is equally valid when considering

a localized signal of finite size, $\Delta t$, which is fully described by the full complex frequency spectrum with the Nyquist sampling rate of $\frac{2\pi}{\Delta t}$. When only the intensity for a frequency spectrum of a signal is measured, it is not the signal itself that is measured, instead it is its autocorrelation [30, 31]. For a strictly localized signal, it's autocorrelation is twice as large [32]. Thus, in order to accurately represent a signal it is expected that the intensity of the frequency spectrum be sampled at half the Nyquist sampling rate [33]. Although, an oversampling rate of two is generally required for phase retrieval, higher oversampling does not give additional information. In fact, for special cases, oversampling of less than two can be used for phase retrieval [34].

Even when a signal is adequately oversampled to describe the signals autocorrelation, a unique solution is not guaranteed during phase retrieval. For instance, the minimum ambiguity present for all far-field diffraction intensities are a constant phase offset (eq. (1.3)), a translational shift of the signal represented by a phase ramp in the frequency spectrum (eq. (1.4)), and a complex conjugated mirror image known as a twin (eq. (1.5)). These can be considered trivial ambiguities, as they do no alter the shape of the signal in any way. In one dimension, non-trival ambiguities have been shown to exists. Since the Fourier spectrum is sampled at discrete points, which can be expressed as a polynomial expansion, it is possible to factorize the $m$ samples of the frequency spectrum into $m$ prime factors. More importantly, the autocorrelation of the signal can be factored into $2m$ factors, where half of the roots are the inverse of the other half. This leading to a maximum of $2^m$ possible solutions [35]. In general, such a case can not be made for more than one dimension, where the solution is almost always unique. This is true either when the signal is known to be positive or when signal is known to be the most compact solution [36]. Counter examples have been found when the signal has certain symmetries, such as the first order Bessel function which can be factorized [37], however, such cases would be rare in actual measurements.

## 3.3 Projections onto constraint sets

There are many algorithms that attempt to solve the phase problem by minimizing an error between recovered and measured intensities, such as the steepest descent or conjugate gradient method. Although, such algorithms have had some success for CDI, they tend to stagnate in local minima. Another class of algorithms, termed projections onto constraint sets, attempt to solve the missing phase by a guided search in a constrained subset of possible solution. In the case of CDI, an object, $O(\mathbf{r})$, representing the signal in real space is desired to be recovered from the the diffraction intensity, $I(\mathbf{q}) = |\mathscr{F}\{O(\mathbf{r})\}|^2$, of the frequency spectrum. Thus, the subset of possible solutions to the full complex diffraction pattern at the detector is any frequency spectrum constrained by the measured intensities,

$$\mathscr{F}\{O_{j+1}(\mathbf{r})\} = \sqrt{I(\mathbf{q})}\frac{\mathscr{F}\{O_j(\mathbf{r})\}}{|\mathscr{F}\{O_j(\mathbf{r})\}|} = \sqrt{I(\mathbf{q})}e^{i\theta_j(\mathbf{q})}. \tag{3.1}$$

In the far-field, this is referred to the Fourier constraint. In addition, the subset of possible solutions to the object, is any pattern constrained by physical limitations. To meet the oversampling condition, a support must exist, such that all amplitudes outside a finite region are zero. The more area that can accurately be set to zero, the fewer possible solutions exist, thus it is desired to obtain a tight support. There are a number of ways this can be obtained.

First, a poor resolution image may be obtained from another technique to obtain a starting point for the reconstruction and define a tight support. A tight support can also be obtained by an autocorrelation [38] or locator set [39]. However, this method produces a twin that must be discriminated, which does not work well for the case of many isolated objects. As an alternative, a loose support may be used as a starting point and updated during reconstruction to exist only in regions where a smoothed version of the object is above a particular threshold. Thus, the support will effectively shrinkwrap a well defined object [40]. It is common for the the support to shrink too much when appropriate parameters are not use, particularly when the object contains a large variation in amplitude. A tight support can usually be accurately obtained by using the shrinkwrap method during a reconstruction of a poor resolution object from low-q diffraction data.

Since this data generally has very good SNR, this objects reconstructs with little possibility of stagnating and with little noise at the given resolution.

Additional constraints may be used when they are self consistent. When they are not, a convergence is likely not achieved. However, when they are, the reconstruction converges quicker since it's searchable subspace has been reduced. Other constraints may include limiting phase in real space. For instance, away from absorption resonances, the scattering from materials can often be considered to be nearly real and positive. Likewise, under special cases, magnetic scattering can also be considered to consist of only 0 and $\pi$ phase information. There may also be amplitude constraints that can be implemented. For instance, in transmission geometry, the object can only attenuate and not increase the amplitude. Thus the object must have amplitude less then or equal to one. Similarly, when reconstructing an electron density, the value should not exceed that of the heaviest atom known to be in the material. Finally, a very useful constraint in transmission geometry is the so called complex constraint [41]. For a single material, the unwrapped phase and amplitude must have a specific relationship due to the refraction and absorption of that material. Although the objects amplitude and phase may certainly vary due to thickness variations, their ratio should be maintained.

The objective is then to find the solution in one subset that when propagated also exists as part of the other subset. The iterative process of propagation between object and diffraction pattern and applying constraints is represented in fig. 3.2. In practice, an initial guess is made for the object (top left of fig. 3.2), such as random values inside the finite support, and propagated to the detector plane. The intensity of the frequency spectrum is then compared to the the measured intensity to establish an error metric. The amplitude of the spectrum is then replaced by the square root of the measured intensity, while keeping the current recovered phases (bottom right of fig. 3.2). The full complex field is then propagated back to the object plane, where the object is updated and constrained by real space limits. The details of each step are determined by the particular algorithm used, the most famous of these being the Hybrid input-output (HIO) algorithm [42] and the Difference Map (DM) algorithm [43]. Both of these are

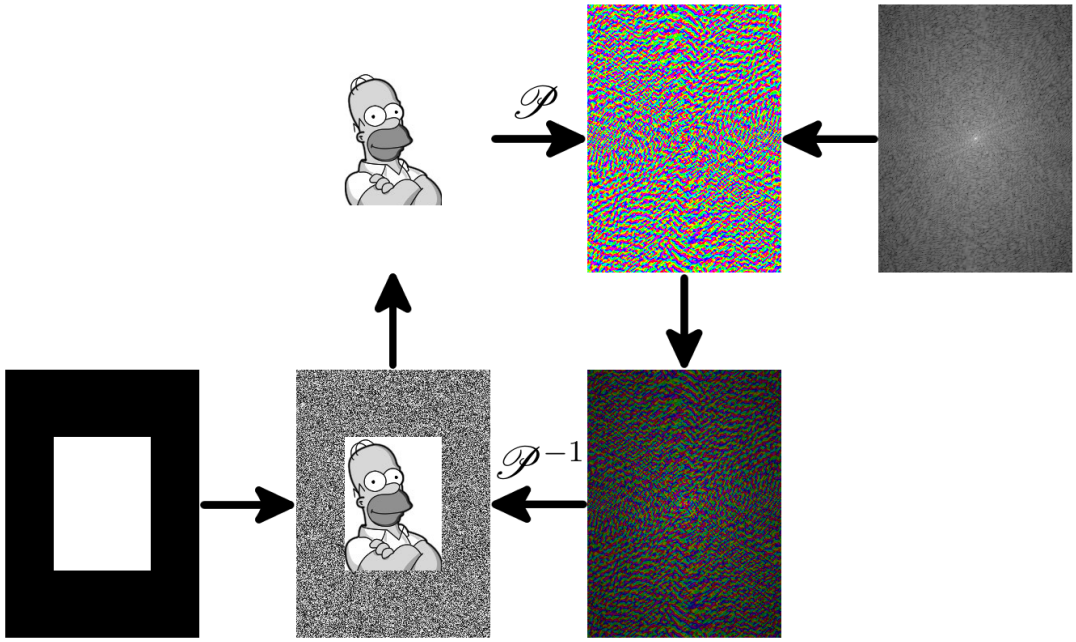


**Figure 3.2**: Iterative phase retrieval algorithm. The current guess of phases at the detector are combined with the measured amplitudes (top right) to obtain the full complex field. This field is propagated the object, where constraints are applied such as a support (bottom left) to obtain the full complex field at the object. This is then propagated to the detector once more and a new iteration begins.

high performance algorithms that avoid stagnation, as they are generalization to the aptly termed error reduction (ER) method, which is equivalent to the steepest descent method [44].

## 3.4 Ptychographic coherent diffractive imaging

The principle of CDI thus far relies on a localized object being illuminated with a known wavefield, usually a plane-wave within the object's oversampled region. If however, a sample of interest is not localized, the illumination must be made localized in order to maintain the oversampling condition of CDI. In principle, if the localized illumination wavefield is known, then CDI is once again directly applicable. Experimentally, such a condition may be achieved if a well known pinhole can be directly place in contact with a sample surface. However, obtaining

the exact pinhole shape can be difficult in itself, particularly since over time x-rays tend to slowly erode materials, changing the pinhole shape. In addition, with this geometry only a single location can be imaged at a time, without much control over the location a priori.

Ptychographic coherent diffractive imaging (PCDI), is a method that extends CDI to unknown localized illumination functions, by taking diffraction patterns from many overlapping regions of the sample. Thus, an arbitrarily large region can be imaged, by simply illuminating more regions. The phase retrieval is accomplished by constraining the real space solution to be the same in the overlapping regions, thereby simultaneously recovering both the object and the illumination function.

Although, ptychography can in principle be used in reflection geometry, it's most common application is for small angle transmission geometry. Recall that the transmission of x-rays through a sample can be described as the propagation of a field through that material, as shown in section 2.3. Thus, to good approximation, the wavefield just after the sample is simply a modification of the incoming illumination wavefield due to absorption and refraction, without any cross interaction of the wavefield itself. In other words, the exiting wavefield just after the sample, termed the view, is given by a simple multiplication of the illumination function (probe) and the modification made by the sample projection (object),

$$\psi_j(\mathbf{r}_\perp) = P(\mathbf{r}_\perp - \mathbf{r}_{\perp,j})O(\mathbf{r}_\perp). \tag{3.2}$$

The probe is in general a non-trivial full complex wave, defined at the sample plane, which is propagating along the z-direction. As indicated, the probe may be shifted relative to the object to produce multiple views, as is necessary for ptychography. The exiting wavefield then propagates to a detector with spatial resolution where the intensity (photons) can be measured,

$$I_j(\mathbf{q}_\perp) = \left|\mathscr{F}\left\{\psi_j(\mathbf{r}_\perp)\right\}\right|^2. \tag{3.3}$$

Here, $\mathscr{F}$ stands for a general propagation operation. For instance in traditional microscopy, this operator will be the result of passing through various optical elements to produce a real space image. For diffraction techniques, there are no

optical elements and the operator could be the Fresnel integral for diffraction to the near field or a Fourier transform for far-field scattering, which will be the case considered here.

It is the objective of PCDI to take a series of measured intensities, $I_j$, and reconstruct the object and probe. Similarly to CDI (eq. (3.1)), the constraint on the frequency spectrum at the detector is any wavefield that satisfies the measured intensities,

$$\mathscr{F}\left\{\psi_j(\mathbf{r}_\perp)\right\} = \sqrt{I_j}e^{i\theta_v} \tag{3.4a}$$

$$\mathscr{F}\left\{P(\mathbf{r}_\perp)\right\} = \sqrt{I_{\mathrm{WF}}}e^{i\theta_p}, \tag{3.4b}$$

where $I_{\mathrm{WF}} = \left|\mathscr{F}\left\{P(\mathbf{r}_\perp)\right\}\right|^2$ is the measured diffraction intensity without the sample in place. During the reconstruction of the object and probe, the view is updated according to whatever algorithm is used. The most successful algorithms are the ptychographic iterative engine (PIE) and it's extended version, ePIE [45, 46], which are considered projections onto constraint sets.

## 3.5 Optimize contrast

When scattering from extended objects, an optimal experimental condition exists that leads to the highest number of photons scattered. A balance exists between allowing a large number of transmitted photons while having a sufficient variation in the sample to allow scattering. The object modifies the incoming illumination due to absorption and refraction, $O(\mathbf{r}_\perp) = e^{-k_0(\beta_l + i\delta_l)z_l(\mathbf{r}_\perp)}$, where the index indicates an Einstein sum over all elements present. For the following, a single element is used as an example; however, it can be extended to any material. Let the material have an average thickness, $\langle z \rangle$, where each position in the object varies from this by $\Delta z$. The fraction of transmitted photons will be given by

$$\int w(\Delta z)|O(z)|^2, \tag{3.5}$$

where $w$ represents the normalized distribution of material thickness variation. Even though, some photons can be considered to have scattered in the forward

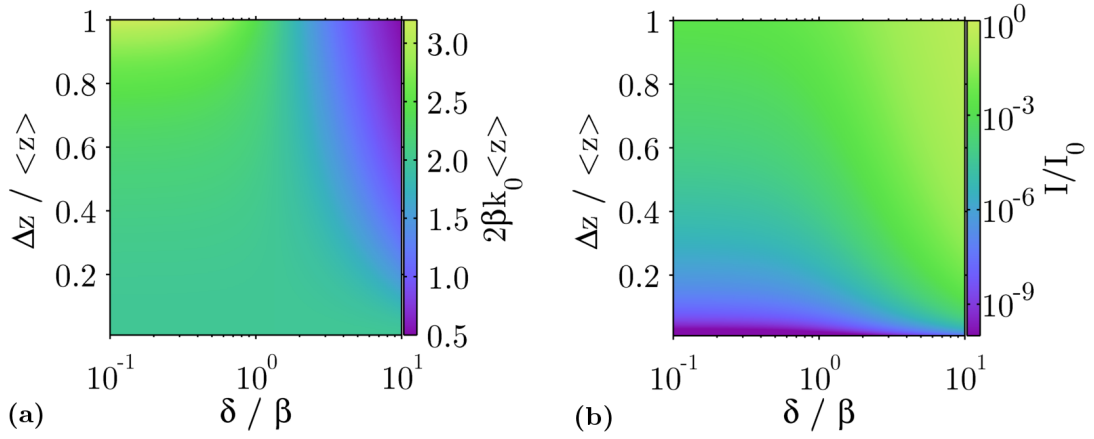


**Figure 3.3**: Optimal Scattering. (a) The ideal absorption power, from which the optimal average thickness can be determined. (b) The fractional photons scattered for the ideal thickness given in (a).

direction, they are not useful since a beamstop is generally used to block the bright direct beam. Thus, the intensity that is not at the zero frequency can be considered scattered photons. Then, by Parseval's theorem and the definition of the Fourier transform at zero frequency, the non-scattered fraction is given by

$$\left| \int w(\Delta z) O(z) \right|^2 . \tag{3.6}$$

Although, the scattering and absorption will depend on the exact distribution of thickness in the material, here it is assumed that the variations in thickness have a flat distribution between $-\Delta z$ and $\Delta z$. An analytic solution then exists to the number of scattered photons,

$$\frac{I}{I_0} = e^{-2\beta k_0 \langle z \rangle} \left[ \frac{\sinh(2\beta k_0 \Delta z)}{2\beta k_0 \Delta z} - \frac{\cosh(2\beta k_0 \Delta z) - \cos(2\delta k_0 \Delta z)}{2(k_0 \Delta z)^2 (\beta^2 + \delta^2)} \right] . \tag{3.7}$$

In general, scattering is increased when the variation in thickness is large and when absorption is small compared to refraction. To some degree, these parameters may be tunable. The optimal thickness of a thin film (fig. 3.3 (a)) and fractional photons scattered (fig. 3.3 (b)) is shown for a most parameters likely to occur.

## 3.6 Weak objects

When an object has low contrast, the number of scattered photons are expected to be low. This leads to difficulty in reconstruction either due to poor photon statistics in plane-wave CDI or due to insufficient real space constraint in PCDI. For transmission geometry, consider an almost uniform object, such that $z_l(\mathbf{r}) = \langle z \rangle_l + \delta z_l(\mathbf{r})$. Using the Helmholtz propagation through a thin film (eq. (2.10)), the object is then,

$$O(\mathbf{r}) = \langle O \rangle [1 + \delta O(\mathbf{r})], \tag{3.8}$$

where $\langle O \rangle = \prod_l \exp\left(-i a_l f_l \langle z \rangle_l\right)$, such that $|\langle O \rangle|^2$ is the constant attenuation factor. The variation in the object is expressed as $\delta O(\mathbf{r}) \approx \sum_l i a_l f_l \delta z_l$, which must have amplitude significantly smaller than one to be valid. The scattering factor of material $l$ is $f_l$ and $a_l = \lambda N_l r_e$. The measured intensities (eq. (3.3)) are

$$I_j(\mathbf{q}) = |\langle O \rangle|^2 \left[ I_{\mathrm{WF}}(\mathbf{q}) + 2\Re\left\{ \mathscr{F}\left\{P(\mathbf{r} - \mathbf{r}_j)\right\}^* \mathscr{F}\left\{\delta\psi_j(\mathbf{r})\right\}\right\} + \left|\mathscr{F}\left\{d\psi_j(\mathbf{r})\right\}\right|^2 \right] \tag{3.9}$$

where $d\psi_j(\mathbf{r}) = P(\mathbf{r} - \mathbf{r}_j)\delta O(\mathbf{r})$ and $I_{\mathrm{WF}} = \left|\mathscr{F}\left\{P(\mathbf{r})\right\}\right|^2$ is the diffraction intensity of the illumination function, which can easily be measured by removing the object. Through the relationship between $\delta\psi_j$ and $\psi_j$ in eq. (3.8) and using the Fourier constraints eq. (3.4), eq. (3.9) can be written as

$$\cos\left(\Delta\theta_j(\mathbf{q}) - \theta_c\right) = \frac{I_j(\mathbf{q}) + |\langle o \rangle|^2 [I_{\mathrm{WF}}(\mathbf{q}) - \delta I_j(\mathbf{q})]}{2|\langle o \rangle| \sqrt{I_{\mathrm{WF}}(\mathbf{q})} \sqrt{I_j(\mathbf{q})}}, \tag{3.10}$$

where $\Delta\theta_j = \theta_v - \theta_p$ is the phase difference between the desired solutions of the view and probe diffraction patterns, $\theta_c = \sum_l a_l \langle z \rangle_l \Re\left\{f_l\right\}$ is a constant phase factor, and $\delta I_j = \left|\mathscr{F}\left\{d\psi_j\right\}\right|^2$ is small but not insignificant. Thus, eq. (3.10) gives the magnitude between the phase difference and thus could be used as a constraint when $\delta I_j$ can be reasonably estimated.

The most problematic part of weak scattering is the simultaneous reconstruction of the probe. As an extreme example, for a completely uniform object, each projection contains no new information. Thus, the plane of the object becomes ambiguous and any Fresnel propagated probe will have the same far-field

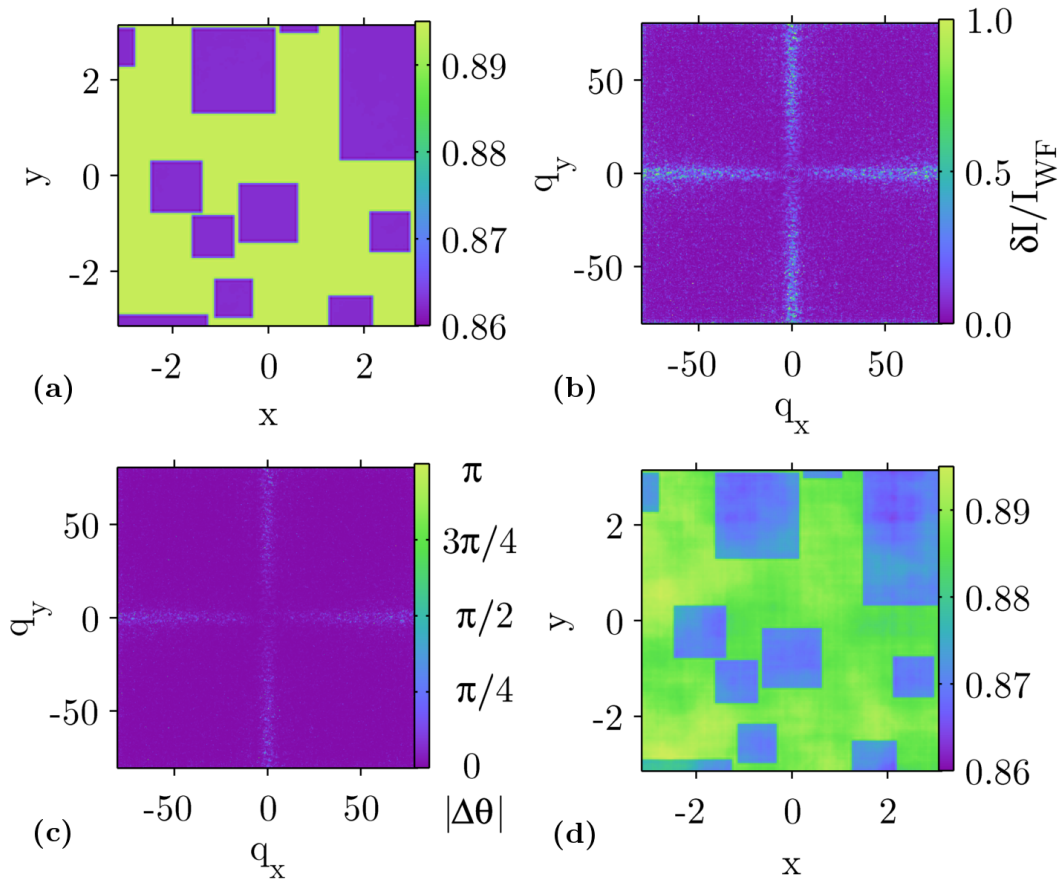


**Figure 3.4**: Weak scattering. (a) A section of a low contrast object. (b) Normalized scattering and (c) phase difference between white field and diffraction from a view. (d) same section as (a) recovered using known probe and measured intensities without additional phase difference.

diffraction pattern. As will be shown in section 3.8, when information is missing in the diffraction intensities, this ambiguity persists for weakly scattering objects. The most effective way of overcoming weak scattering is to start with a probe function that is very close to the actual probe function. This can be done in a number of ways. First, a strongly scattering sample can be put in place of the weakly scattering sample. A reconstruction of this sample will give a good approximation to the probe used for the weakly scattering sample (up to changes in beam characteristics and difference in placements of the sample). Second, the pinhole shape and size can be determined and a propagated to the object plane. The simplest method is to assume a circular pinhole where the size can be approximated from measuring the fringes produced by scattering from the pinhole alone. Secondly, the pinhole can be measured in a microscope. This however has several problems as sufficient resolution requires significant effort. Since the measurements are made ex situ, possibly with a technique that sees the pinhole edge differently due to absorption differences, this is not ideal. This is particularly true since pinholes are known to change over time scales of a day with x-ray illuminated due to residue and damage. If the complete coherent diffraction intensity is measured, it is a simple task to reconstruct the pinhole with the constraint of a real object.

Once the illumination function is known, a very good starting guess of the object can be obtained by using the constraint of eq. (3.10). To demonstrate this, a weakly scattering object, with a few percent contrast (a portion of which is shown in fig. 3.4 (a)), is illuminated with a probe. It's scattering is very similar to the scattering without the object, where the normalized differential scattering, $\delta I_j / I_{WF}$ (fig. 3.4 (b)) is small for many frequencies and thus the difference in phase between the probe scattering and view scattering is also small (fig. 3.4 (c)). In fact, if the phase difference is set to zero, such that the view scattering is given by its measured amplitude and the probe scattering phase, an approximate object can be recovered immediately (fig. 3.4 (d)).

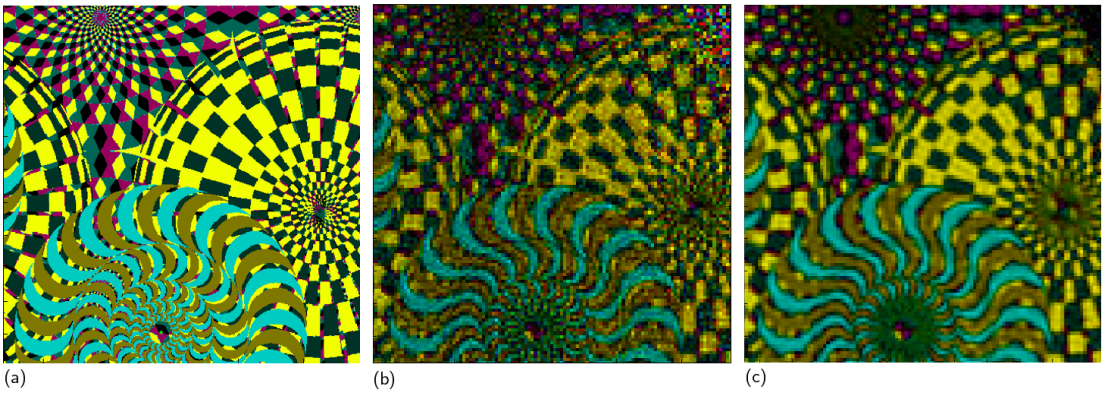


**Figure 3.5**: Illustration of a reconstruction with noise in the measured diffraction intensity. (a) a portion of the exact solution, (b) a single reconstruction from a noisy diffraction pattern, (c) several reconstructions of the same diffraction pattern averaged together.

## 3.7 Noise

When noise, whether detector noise or photon shot noise, is present in the diffraction pattern, the exact solution can no longer be obtained. A solution that strictly satisfies the Fourier constraint (eq. (3.1)) of a noisy diffraction pattern, will not strictly satisfy the real space constraint of being fully confined within a finite support. As a consequence a true minima does not exist during phase retrieval and several solutions can be obtained with comparable error between the measured and recovered Fourier amplitudes. The number of solutions possible depends on the number of local minima and thus the amount of noise present in the diffraction pattern. As will be discussed in the next chapter in detail, due to the distribution of photon scattering in a diffraction pattern, high spatial frequencies are more susceptible to noise, effectively resulting in loss of spatial resolution.

As an example, a complex two dimensional object (a portion of which is shown in fig. 3.5 (a), using the HSV-color space in section 1.4), is propagated to the far-field and Poisson statistics applied, such that the signal-to-noise ratio falls below one at roughly one half of the inverse pixel size. When a single phase retrieval is performed to a solution with a minimized error, significant noise is present in the reconstruction (fig. 3.5 (b)). Although significantly small features can be seen

in the reconstruction, it is yet unknown which features are present in all possible solution and which are simply noise. When many phase retrievals are performed and averaged together (fig. 3.5 (c)), the distinction becomes clear. Effectively, the recovered phase will have larger variations between reconstructions at spatial frequencies with low SNR. Thus, when many reconstructions are averaged together, the recovered Fourier signal intensity is reduced in these regions. The recovered intensity normalized by the true solution intensity is then the Fourier transform of the point spread function, smearing out features on the order of $\frac{2\pi}{q_c}$ in size, where $q_c$ is the cut off frequency where the SNR falls below one.

## 3.8 Missing information

When an incomplete diffraction pattern is measured, where some intensity information is missing, it is possible not only to obtain a set of solutions that nearly satisfy the constraints, it is possible for several solutions to exactly satisfy the constraints. The simplest of these examples is when high spatial frequencies are not measured. This case is very similar to the effect of noise in the diffraction pattern, where uncertainty in the recovered diffraction pattern exists at high spatial frequencies. As a consequence, features smaller than the inverse of this frequency can not reliably recovered.

The more troubling case is when low spatial frequencies are not measured, as is the case when a beamstop is necessary to block the direct beam in transmission experiments. As a very simple example, when a plane wave is used to illuminated an object, the direct beam is only present at the zero frequency. If only this information were lost, a simple ambiguity between a signal and its complimentary signal exists in the reconstruction, by Babinet's principle (eq. (1.10)). However, when the beamstop is of finite size, additional ambiguities arise. Roughly speaking, the number of low frequency modes that could be present in the solution is given by $\prod \frac{q_m \Delta X}{\pi}$ where the product is over all dimensions, $\Delta X$ is the size of the object, and $q_m$ is the spatial frequency below which no measurement was made. Sometimes, the modes can be constrained with additional information about the real space

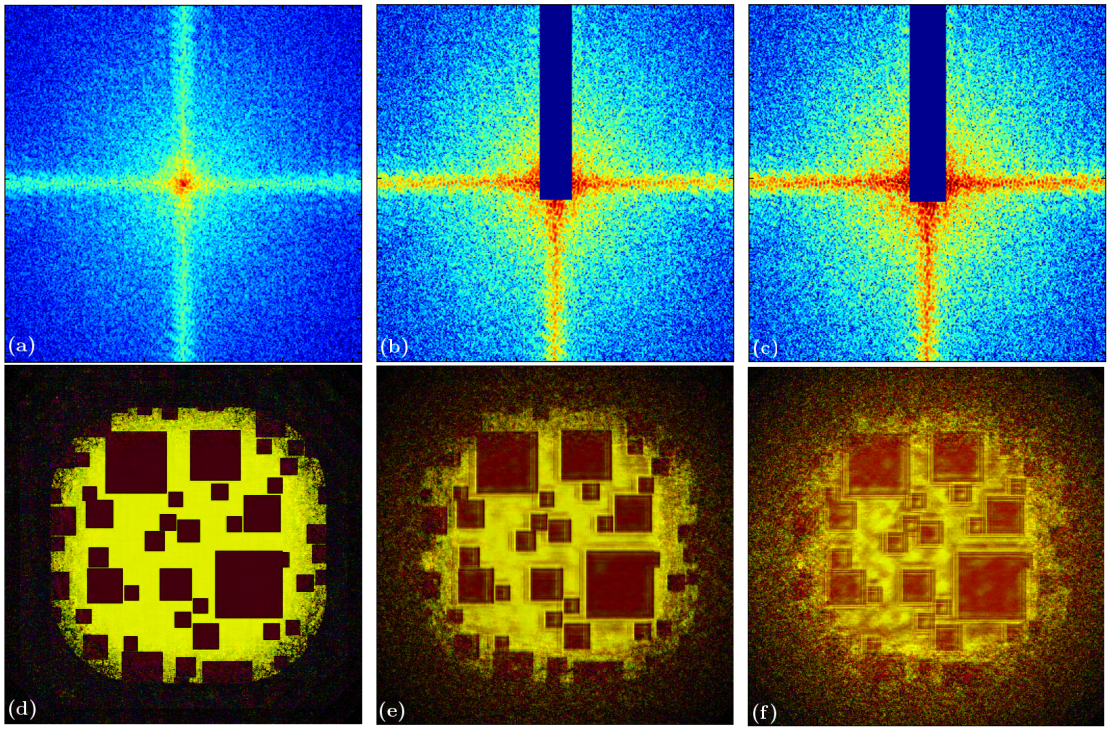


**Figure 3.6**: Reconstruction with central beamstop for a high contrast object. (a) The diffraction intensity with no beamstop and (e) its corresponding reconstruction. (b) The diffraction intensity with a beamstop 47 pixels wide and (e) its corresponding reconstruction showing some low frequency modes. (c) The diffraction intensity with a maximum possible beamstop 53 pixels wide and (e) its corresponding reconstruction showing some erroneous features.

object, such as known symmetry or a low spatial resolution image of the object from another technique [47].

For PCDI, the situation is somewhat different since an additional contraint already exists, namely the overlap of neighboring view. As an example, the reconstructions of a high contrast (fig. 3.6) and low contrast (fig. 3.7) object is shown. Diffraction patterns were simulated with $10^9$ scattered photons at 1080 eV from gold squares with thickness of 10 µm (high contrast) and 10 nm (low contrast). As the beamstop size grows, additional low frequency features appear in the reconstruction. Since sharp edges produce scattering at high spatial frequencies, these features tend to survive the longest. The high contrast object, can tolerate a much larger beamstop due to the weak scattering problem discussed in section 3.6. In

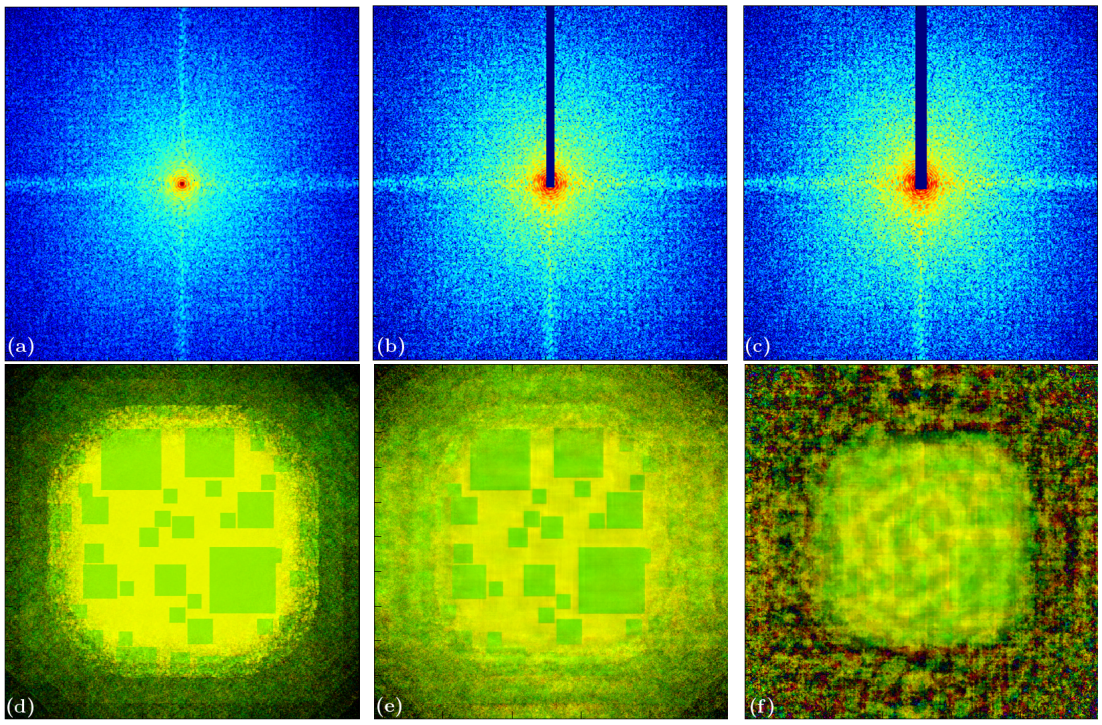


**Figure 3.7**: Reconstruction with central beamstop for a low contrast object. (a) The diffraction intensity with no beamstop and (e) its corresponding reconstruction. (b) The diffraction intensity with a beamstop 11 pixels wide and (e) its corresponding reconstruction showing some low frequency modes. (c) The diffraction intensity with a maximum possible beamstop 17 pixels wide and (e) its corresponding reconstruction showing some erroneous features.

short, although the diffraction patterns of the high and low contrast objects have the same signal-to-noise ratio, the high contrast diffraction contains more unique information compared to the low contrast diffraction with the same beamstop size.

## 3.9 Coherent modes

There are a number of cases where the observed scattering can be described as a sum of orthogonal coherent modes. By orthogonal, it is meant that the modes do not interfere with each other, such that the total scattering is a sum of their respective intensities. For instance, a nearly coherent illumination of a sample can be expressed as a linear combination of coherent modes [48, 49, 50, 51]. This is frequently used to improve reconstruction of objects, since the coherence length can be comparable to the object size for synchrotron radiation [21]. It is mathematically equivalent, if the role of the object and probe are switched. Thus, this is directly applicable to situations where the sample switches between states within the time of exposure. In the most general case, the measured intensity can be expressed as a total of n modes, which is any combination of probe and object mode,

$$I = \sum_{k=1}^{n} \left| \tilde{\psi}_k \right|^2, \tag{3.11}$$

where $\tilde{\psi}_k = \mathscr{F}\{\psi_k\}$, is the wavefield at detector from the k-th mode. This idea has been extended to ptychography [52]. Later, in section 5.7, it will be shown that this is directly applicable to the case of certain magnetic scattering and how it can be used to reconstruct the charge and magnetic components of a sample simultaneously.

## 3.10 Mixed modes

There is an additional ambiguity that arises from using modes. Namely, the entire special unitary group, SU(n), is equivalent in this case. The unitary operator applied to the set of modes, $\tilde{\boldsymbol{\psi}}' = \mathbf{U}\tilde{\boldsymbol{\psi}}$ with $\tilde{\boldsymbol{\psi}} = [\tilde{\psi}_1, \ldots, \tilde{\psi}_n]^\top$, conserves

the $\ell^2$-norm of eq. (3.11). In the most general case,

$$\mathbf{U}(\phi, \alpha, \theta) = \mathbf{I}(\phi)\mathbf{R}(\alpha)\mathbf{I}(\theta) \tag{3.12}$$

where $\mathbf{R}$ represents an operator that takes a normalized linear combination of modes and $\mathbf{I}$ represents an operator that takes phase shifts of the individual modes. This is equivalent to a generalized rotation.

It is instructive to look at a two mode example to see the properties of this operation. Since in CDI a constant phase shift are of no importance, the two mode example can be written as,

$$\begin{bmatrix} \tilde{\psi}'_1 \\ \tilde{\psi}'_2 \end{bmatrix} = \mathbf{U}(\epsilon) \begin{bmatrix} \tilde{\psi}_1 \\ \tilde{\psi}_2 \end{bmatrix} = \frac{1}{\sqrt{1+|\epsilon|^2}} \begin{bmatrix} 1 & \epsilon \\ -\epsilon^* & 1 \end{bmatrix} \begin{bmatrix} \tilde{\psi}_1 \\ \tilde{\psi}_2 \end{bmatrix}, \tag{3.13}$$

where $\epsilon$ is any complex constant. If two consecutive operations are done in this manner using $\epsilon_1$ and $\epsilon_2$, the transformation can be written in an equivalent manner, $\mathbf{U}(\epsilon_2)\mathbf{U}(\epsilon_1) = \mathbf{I}(\theta/2)\mathbf{U}(\epsilon')\mathbf{I}(\theta/2)$, where

$$\mathbf{I}(\theta/2) = \begin{bmatrix} e^{i\theta/2} & 0 \\ 0 & e^{-i\theta/2} \end{bmatrix} \tag{3.14}$$

$e^{i\theta} = \frac{1-\epsilon_1^*\epsilon_2}{\left|1-\epsilon_1^*\epsilon_2\right|}$, and $\epsilon' = \frac{\epsilon_1+\epsilon_1}{1-\epsilon_1^*\epsilon_2}$. This has two consequences, namely any single operation is easily reversible simply by using $\epsilon_2 = -\epsilon_1$. Secondly, the entire SU(2) group cannot be access from any arbitrary other point in the same group with a single unitary operator described by eq. (3.13). That said, the operator $\mathbf{U}(\epsilon' e^{-i\theta})$ is equivalent to $\mathbf{U}(\epsilon_2)\mathbf{U}(\epsilon_1)$, with the exception of a constant phase shift. Since constant phase shifts are unimportant for CDI, any two modes can be fully unmixed by a single operator of the form in eq. (3.13).

The mixing of modes during phase retrieval is generally not a problem. When there are multiple modes in the probe, these can be left mixed, since it is usually not desired to obtain the probe modes. However, when multiple object modes are present, it is desirable to obtain the pure, unmixed results. Constraints on the mode's real space solution generally results in a convergence to the correct pure modes.

# Chapter 4

# Atomic Resolution

## 4.1 Introduction

X-rays have been used to successfully determine the atomic structure of crystalline materials of increasing complexity for over 100 years. Obtaining the unit cells of simple crystals was one of the first great achievements of x-rays [53]. This method routinely allows the refinement of atomic positions in highly ordered crystals with better than 1 pm precision [54, 55]. Furthermore, protein crystallography has obtained the structure of extremely important organic molecules such as DNA [56] and penicillin [57], which have greatly impacted our understanding of life and medicine. However, crystallography only determines the average atomic positions in perfectly periodic crystalline structures. Thus, these methods have not been able to address the materials that cannot be crystallized, the location of defects in crystals, or the atomic positions in disordered materials.

Atomic resolution has been achieved for surfaces using scanning probes [58] and for very thin films using transmission electron microscopy [59]; however, interfaces can differ significantly from the bulk. Since x-rays penetrate bulk materials, have sufficiently short wavelength, and have chemical sensitivity, they are ideal for atomic-scale three-dimensional microscopy. Both x-ray full field imaging and scanning transmission microscopy have had great success [60, 61]. Although they can still be improved, these techniques can never reach atomic resolution due to their reliance on optical elements [62]. Instead of using incoherent radiation to image

only ordered materials, it is possible to image any material, up to the diffraction limited resolution, using coherent x-ray diffractive imaging (CXDI). In order to accomplish this, one must solve for missing phase information in the measured diffraction intensity and back propagate the full complex field to the sample [63]. Since the interaction between particles and fields are well understood at the atomic level, a quantitative image of the atomic structure can be formed. The iterative phase retrieval method has rapidly improved and CXDI is now widely used to obtain the local distribution of electron densities and lattice strain of nanocrystals [64, 65, 66]. In addition, CXDI has achieved great success in imaging non-periodic structures [67, 68, 69].

The necessary dose to image a sample at a particular resolution, $\delta x$, has previously been suggested to scale as $\delta x^{-n}$, where $n = 4$ or 5 [70, 71, 72]. This implies that a very large increase in x-ray flux, compared to current available sources, is necessary to reach atomic resolution. We will show that with increasing disorder, atomic resolution can be achieved at doses well before the power-law scaling predicts. In section 4.2 we will discuss a method to predict the number of photons required to image a particle at a desired resolution. As an example, we generate the atomic positions of two materials, simulate their diffraction pattern at various photon doses and use phase retrieval algorithms to obtain a reconstructed image of the atomic positions. In section 4.4, we show the results of the reconstructions, which validate the predictions made. Finally, in section 4.5 we discuss the performance of currently available x-ray sources and anticipate what next-generation sources in the near future will be able to achieve.

## 4.2 Image quality

It is important to understand image quality for any microscope and to predict what can be achieved under various conditions in order to find limiting factors. In this case, we restrict ourselves to images formed from far-field diffraction patterns, such as in CXDI. The far-field Kinematic scattering is proportional to the Fourier transform of the electron density, $F(\mathbf{q}) = -\frac{r_0}{R}\sum_m f_m e^{-i\mathbf{q}\cdot\mathbf{r_m}}$, where $f_m$

is the atomic scattering factor of atom $m$. The expected image resolution can be estimated from the spatial frequency, $q_c$, where the average signal-to-noise ratio (SNR) drops below some threshold (see Appendix 4.6 for a detailed derivation of this condition). For direct-space imaging, a threshold of five is common [73], while for CXDI this threshold is usually set to one [68], which is also used here. This condition may be written in terms of the number of photons scattered and collected, $I(q_c)\eta a t \approx 0.5(1+\sqrt{1+4\varsigma^2}) \equiv \Sigma$, where $I(q) = I_0\langle P(\mathbf{q})|F(\mathbf{q})|^2\rangle$ is the azimuthally averaged scattered flux, $t$ is the exposure time, $a$ is the area of the detector pixels, $\eta$ is the detector efficiency, $\varsigma$ is the noise level of the detector, and $P$ is a geometric factor due to polarization of the incoming x-rays. Although this relation is strictly valid only for isotropically scattering samples, it also holds true for scattering from crystalline materials, which have strong Bragg diffraction peaks. This is because the cutoff spatial frequency is limited by regions with low SNR (i.e. regions between Bragg peaks), which are relatively uniform.

Let us assume we have a curved detector that evenly samples the Ewald sphere. To meet the oversampling condition needed for CXDI, the area of each detector pixel should be $a = R^2(\frac{\lambda}{s\Delta x})^2$, where $R$ is the distance from the sample to the pixel, $\lambda \leq 4\delta x$ is the photon wavelength, $\Delta x$ is the maximum size of the sample, and $s$ is the minimum 1D oversampling ratio. Thus, the exposure time needed to adequately measure a single slice of the Ewald sphere at the desired resolution, $\delta x = \pi/q_c$, is

$$t = \frac{s^2\Sigma}{I_0\eta\lambda^2\upsilon\langle P(\mathbf{q}_c)|f(\mathbf{q}_c)|^2\rangle\Delta x}, \tag{4.1}$$

where $f(\mathbf{q}) = \frac{\lambda}{2\pi}\frac{R}{\sqrt{V}}F(\mathbf{q})$ is the normalized scattering factor and $\upsilon \equiv \frac{V}{\Delta x^3}$ is the percent volume fraction of the particle. For unpolarized x-rays, $P(\phi) = \frac{1}{2}(1+\cos^2\phi)$, which can equivalently be achieved with linear polarization and sufficient rotational freedom of the sample.

By using the normalized scattering factor, it is easier to see the general trend in Eqn. 4.1. The $\lambda$ factor is necessary due to the transformation from frequency space, $\mathbf{q}$, where the scattering factor is well defined to the scattering angle, $(R,\theta,\phi)$, where the detector is well defined. The factor $\sqrt{V}$, is necessary to normalize

the intensity by the size of the particle. When the correlation length is much smaller than the total size of the particle, such as in amorphous materials or highly disordered crystals, then the scattered intensity scales with the number of uncorrelated volumes. Thus, apart from fluctuations in the coherent speckle which encode the location of each atom, the normalized scattering factor is independent of particle size, in this limit. However, perfect single crystals will not exhibit this simple behavior. Instead, increasing the amount of material redistributes the scattering by narrowing the Bragg peaks, which includes the (000) peak present for all materials. As will be seen later, the required exposure time to reach a particular resolution is then directly proportional to the particle size.

When the scattering angle is small, such that the measured Fourier slice is roughly planar, the data represents a projection of the sample and Eqn. 4.1 represents the imaging time necessary to distinguish a two dimensional (2D) pixel of size $\delta x^2$ in the projection with statistical significance. In order to extend this to three dimensions, the contribution of a three-dimensional voxel in the sample must provide statistically significant information in the projection. If the sample is roughly uniform, the scattering from a single slice of thickness $\delta x/\Delta x$, gives the appropriate voxel contribution. Thus, dividing Eqn. 4.1 by this factor gives the necessary condition to obtain the three dimensional (3D) resolution, $\delta x^3$. By extension, it would also be the condition to obtain the same voxel resolution from the set of tomographic projections necessary to obtain the full 3D spatial information, using dose fractionation [74, 75].

It is possible to obtain a similar, more general result by considering taking a series of two-dimensional slices, each satisfying Eqn. 4.1. To sample the three-dimensional Fourier space, the sample must be rotated perpendicular to the incoming radiation direction while oversampling all voxels up to the largest spatial frequency needed for a particular resolution. Thus, the rotation angle step size is given by $\delta\alpha = \frac{\delta q}{q_c} = \frac{2}{s}\frac{\delta x}{\Delta x}$. Due to the curvature of the sampling, to measure the full 3D diffraction pattern the other orthogonal direction should be rotated as well through an angle $\pm\phi_m = \pm \arcsin\left(\frac{\lambda}{4\delta x}\right)$. The necessary number of slices is then

$N = s\frac{\Delta x}{\delta x}(\pi + \phi_m)$, such that the total exposure time is,

$$Nt = \frac{s^3(\pi + \phi_m)\Sigma}{I_0\eta\lambda^2\upsilon\langle P(\mathbf{q})|f(\mathbf{q})|^2\rangle\delta x}. \tag{4.2}$$

Up to a prefactor, this is the same result as expected from dose fractionation. The total exposure time needed can be reduced by increasing the available flux or by making use of scattering resonances. Additionally, it is only weakly dependent on the sample size because any gain in scattered intensity due to more material is negated by the additional sampling required. In practice, however, it will be easier to image smaller samples with the use of focusing to achieve a higher x-ray flux. Furthermore, using a wavelength nearly four times the resolution desired and obtaining scattering in the full $4\pi$ solid angle can reduce the required sampling time, as long as the atomic scattering factors do not drastically reduce with lower energies. However, in reality, the detector cannot be changed for each experiment. Since the detector will have a specific pixel size and radius of curvature, the value $(\frac{s}{\lambda})^2$ is fixed in the measured data. The data may be binned post-measurement to obtain a different oversampling ratio. The necessary sampling time (Eqns. 4.1 and 4.2) will still be correct, with the new oversampling ratio and the detector noise adjusted for the number of pixels binned together, $\varsigma' = \sqrt{\sum \varsigma^2}$. Although we have considered $\Delta x$ as the maximum length of the sample and $s$ the minimum 1D oversampling, for highly asymmetrical samples where the percent volume fraction, $\upsilon$, is small, it is possible to bin data along only one or two dimensions, as appropriate, to reduce the necessary sampling time.

In real experiments, limits in the sample rotation and a necessity to block the direct beam will result in missing data in Fourier space. This tends to reduce image quality by allowing a set of possible solutions. In some cases, this can be overcome by additional information such as constraints on the set [47] or redundancy from overlapping projections such as in ptychography [69]. In addition, since the scattering factors away from resonances are primarily real, the scattered intensity is centrosymmetric, which can be used to fill in missing information or to increase SNR [76].

To consider the general trend of Eqn. 4.2, take for instance a uniform spherical particle whose scattering factor is proportional to $j_1(q\Delta x)(q\Delta x)^{-1}$, where

$j_1(q\Delta x)$ is the spherical Bessel function of the first kind. Since we are interested in resolutions much smaller than the particle itself, we can consider the limiting case $q\Delta x \gg 1$. In this case, the scattering intensity due to the particle form factor decays as $q^{-4}$. Using Eqn. 4.2, we see that for a uniform density particle, the total time needed to image a particle would be, $Nt \propto \delta x^{-5}$. This assessment is discouraging, since reaching atomic resolution for even high-Z materials would require on the order of $10^5$ improvement in average flux, which will not be feasible for any x-ray source within the next few decades. Fortunately, as we will see in section 4.4, this is not the case because the particle is in fact made of discrete objects, resulting in order at the atomic scale.

## 4.3 Method

We created the atomic positions of three particle types. First, a crystalline Au particle (fig. 4.1(a)) was created using the known face-centered cubic unit cell parameters [77]. Several defects were introduced, including one screw dislocation of nominal width 5 Å with slip plane (111) and Burger's vector $[1\bar{1}0]a/2$. Additionally, two vacancies and two interstitials, with local distortion size of 5 Å were added. The particle was shaped into an asymmetric spheroid with nominal diameter of 20 nm, containing $2 \times 10^5$ atoms. Secondly, an amorphous Au particle (fig. 4.1(a)) was created using the ideal amorphous solid model with hard spheres [78]. First, a single atom is generated and $4 \leq l \leq 12$ atoms distributed randomly around it, such that they are all "touching" the central atom. This cluster forms a seed, upon which further atoms are added without violating minimum interatomic distances. The number of atoms in the seed strongly influences the final packing ratio of the particle generated. Here we use $l = 9$ resulting in a packing ratio of 0.60. The amorphous Au particle, like the crystalline particle, consists of $2 \times 10^5$ atoms and is the same size and shape. The simulated x-ray diffraction shows the clear distinction between the two Au particles (fig. 4.1 (c)). The crystalline particle displays sharp Bragg peaks, which result in regions of very high and very low scattered photons. The amorphous particle displays the expected liquid structure factor, with more

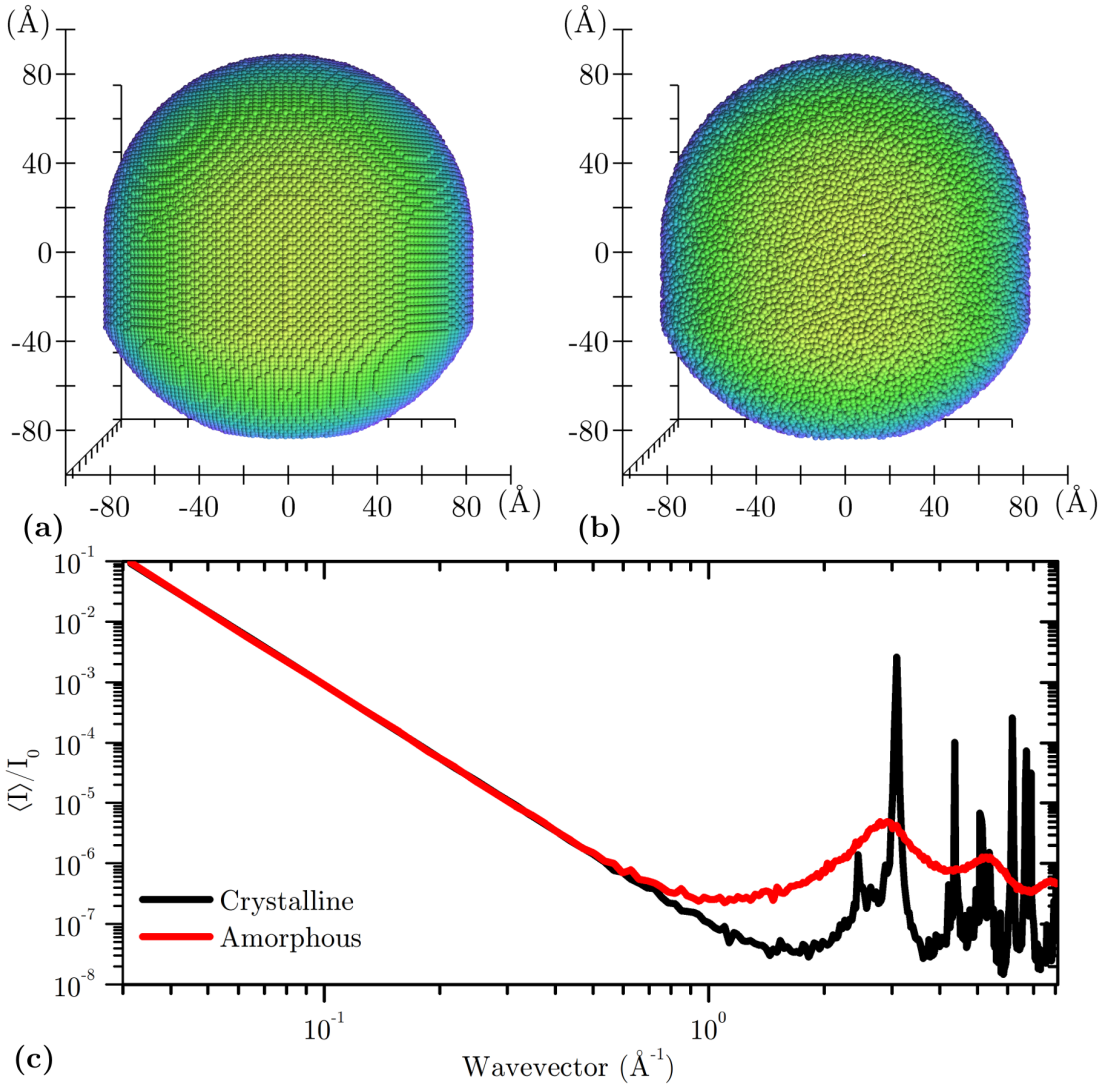


**Figure 4.1**: Normalized and azimuthally averaged scattered intensity for a crystalline particle (a) and an amorphous particle (b) with equal size and electron density. The high degree of order in crystalline materials results in sharp bragg peaks [(c) black line] leaving regions of Fourier space with very little scattered photons. On the other hand, the disorder in amorphous materials spreads out the scattering in Fourier space [(c) red line], which will result in better SNR near atomic resolution.

evenly scattered photons as compared the crystalline particle. Finally, a G-Actin protein is obtained from crystallography measurements, which is the best refined average G-Actin protein without hydrogen. It contains 3965 carbon, nitrogen and oxygen atoms in addition to 31 sulfur, 3 phosphorus, and 1 strontium atom.

Once we had the positions of all atoms [Fig. 4.2(a)], we simulated diffraction data by doing an explicit Fourier transform (FT) onto a regular Cartesian 3D grid [Fig. 4.2(b)]. For each atom type in the particle, the FT is done separately and scaled using an estimated q-dependent scattering factor and Debye-Waller factor at 10 keV photon energy near room temperature [79, 80]. Although we have ignored higher order thermal diffuse scattering (TDS) beyond the Debye-Waller factor, it's contribution can be significant for low-Z materials when approaching the Debye temperature [24]. TDS will contribute an incoherent background to the scattering intensity due to phonons in the material. This can become a significant problem in regions of low coherent scattering, such as between Bragg peaks in highly-ordered crystalline materials. Since CXDI is optimal for relatively small particles, on the order of a few hundred nanometres or less, the error introduced by TDS is expected to be minimal for materials like Au at room temperature. However, there will be many cases where TDS will need to be subtracted by using other measurements, theoretical predictions, or approximately by observing loss in coherent speckle visibility [26, 27].

Since the grid oversamples the diffraction pattern, it is smoothly varying between neighboring voxels on the grid and the diffraction intensity was calculated only for the center of each voxel and not integrated over the entire voxel volume. Actual measured data will be a recombined series of 2D slices. To achieve appropriate oversampling at large spatial frequencies during rotation of the sample, small spatial frequencies will be oversampled much more. We simply counted the number of times each voxel on the 3D grid would be sampled and multiply it to our simulated 3D diffraction pattern before applying Poisson statistics. This circumvents the extremely costly technique of simulating a series of 2D diffraction patterns and then mapping those pixels to the 3D Cartesian grid. Since mapping the data is done by methods of interpolation [81], additional errors will be intro-

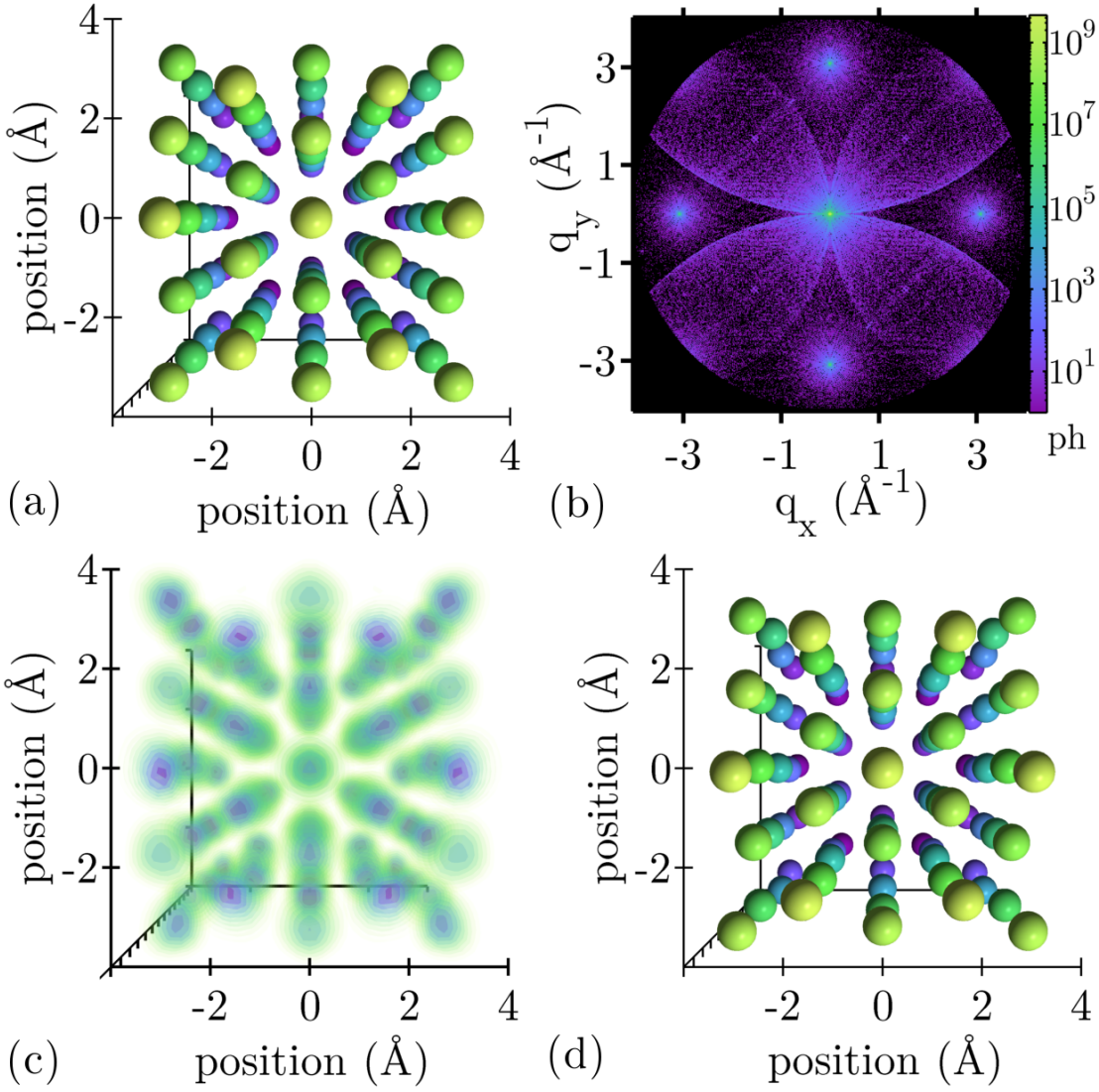


**Figure 4.2**: Method of simulation. (a) Atomic positions are generated, where color is used to better indicate depth, which are (b) Fourier transformed to a regular Cartesian 3D grid (scattered photons shown on log scale). (c) An inverse Fast Fourier transform of the full complex scattered wave gives the electron density from which (d) the atomic positions and atomic number can be recovered.

duced in measurements. Alternatively, a cylindrical grid can be used, which more accurately represents the measured sampling, in conjunction with the fast polar-FT [82, 83] for phase retrieval. However, this is significantly more computationally costly due to the ill-defined inverse polar transform and very memory intensive due to the storage of the highly over-sampled data near the origin.

To illustrate the minimum error that is introduced by discretizing the diffraction data, the electron density is obtained by performing the inverse fast Fourier transform (FFT) of the simulated full complex diffraction data [Fig. 4.2(c)]. Since no effort was made to match voxel positions with atom positions, the recovered electron density for each atom location extends beyond a single pixel. The approximate location of the atoms and their atomic number [Fig. 4.2 (d)] can be recovered from the discrete electron density map, when atoms are sufficiently separated compared to the pixel size. First, local maxima in the map are obtained. For each maxima, surrounding pixels are used to calculate a center of mass and the map is subpixel shifted in an attempt to center the atom in the nearest pixel. This process is done iteratively several times, until the shift becomes negligible. At this point, the atom is contained within a single pixel whose position and atomic number can easily be identified. The recovered locations have a mean absolute error (MAE) and maximal error (ME) of 0.12 Å and 0.22 Å, respectively, which is far below the voxel size used of 0.78 Å.

Reconstruction of the electron density from simulated diffraction intensities is done using the Hybrid input-output (HIO) algorithm [42] and Difference Map (DM) algorithm [43]. The only real space constraint used is a support that is allowed to change through the shrinkwrap method [40]. Although it is possible to start the recovery from a completely random guess, recovering a set of discrete objects is notoriously time consuming. The reconstruction process essentially traverses randomly through a very large phase space until it comes close to the solution [43]. To reduce the number of total iterations needed for many reconstructions, we start most of the reconstructions with a linear combination of a uniform density within a support that defines the particle's edge and the actual solution convolved with a point spread function and randomly sub-pixel shifted. In addi-

tion, a random complex value is added to each voxel with variations on the order of the maximum electron density. An average reconstruction is formed by combining the best 11 of 15 total reconstructions after adjusting for any complex conjugated mirror image, constant phase offset, and relative particle translation [84, 85]. From this, the mean absolute error (MAE) between the recovered and actual phase of the diffraction pattern is calculated and averaged azimuthally along shells of constant $|\mathbf{q}|$. Here, an MAE of 0 would be perfect correlation between measured and recovered, 2 is a perfect anti-correlation (i.e. $\pi$ phase shift), and 1 is equal correlation and anti-correlation or no correlation at all. We defined the resolution of the recovered electron density as $\pi/q_c$, where $q_c$ is the lowest spatial frequency where the MAE becomes greater than 0.5. This is equivalent to the phase retrieval transfer function (PRTF) commonly used to define resolution when the solution is not known, except that the PRTF measures how well the set of solutions compare to each other instead of a known solution [68, 69]. Thus, if the recovered solutions always stall in the same local minima during phase retrieval, the PRTF will indicate a better resolution than actually achieved. We use the PRTF to check that we have not biased our solutions with the given starting guess.

## 4.4 Results and discussion

To test the predictions of Eqn. 4.2, we have simulated the diffraction data for several materials and used CXDI to reconstruct their atomic position. For this, we assume a photon energy $E = 10$ KeV, a perfect photon capture efficiency of the detector $\eta = 1$, and no detector noise $\varsigma = 0$. Here we use a 1D oversampling $s = 2$, which is sufficient to achieve high probability of reconstruction success, but in some cases can be lower [34].

The crystalline Au diffraction intensity was simulated with a wide range of time-integrated photon flux (TIPF) between $6 \times 10^{14}\,\mathrm{ph/\mu m^2}$ and $1 \times 10^{19}\,\mathrm{ph/\mu m^2}$. The resolution obtained using CXDI of these simulations matches extremely well to the predictions from Eqn. 4.2 until the expected resolution becomes lower than the pixel size. The resolution versus TIPF initially

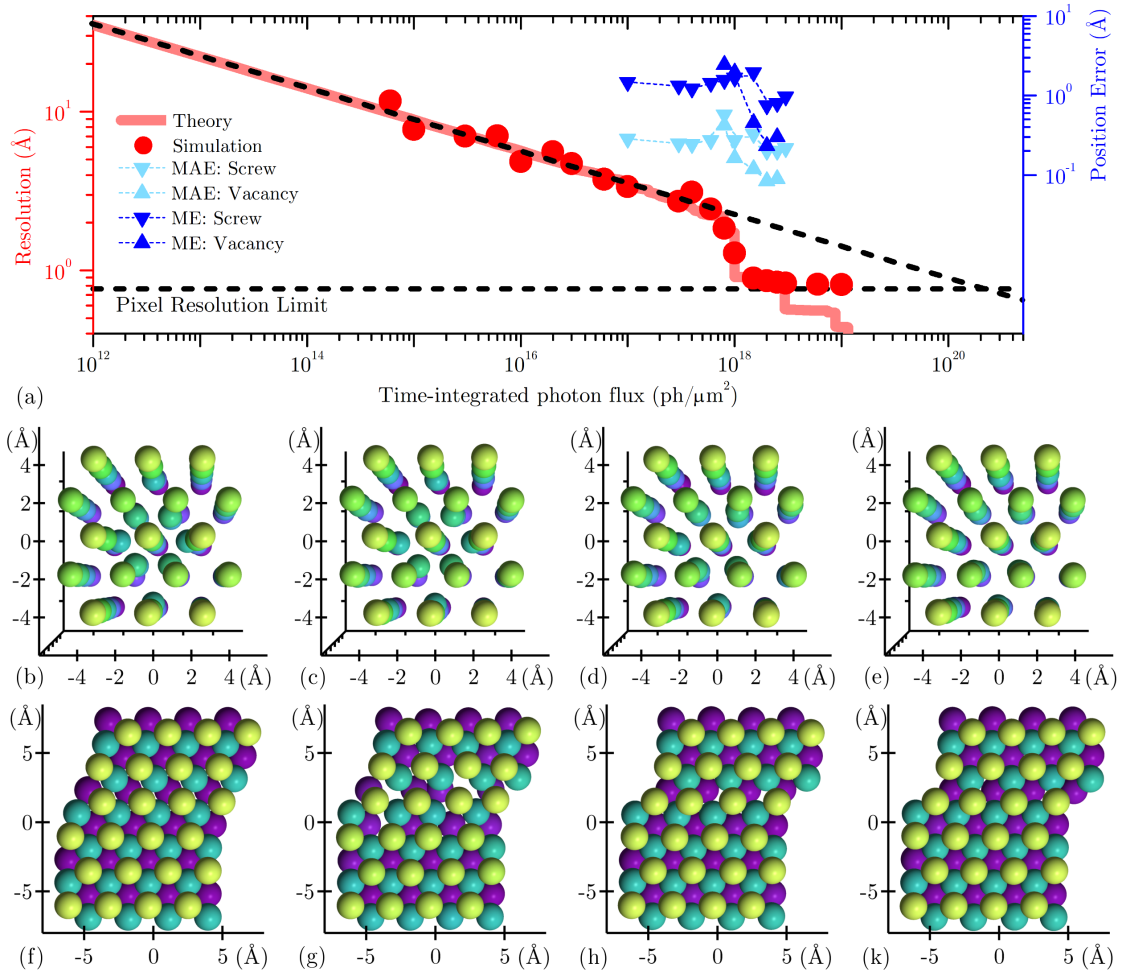


**Figure 4.3**: Crystalline Au particle. (a) Achievable resolution, where the solid line is the theoretical model described by eq. (4.2) which follows much of the expected $\delta x^{-5}$ fall off for a uniform particle. The circles are reconstructions using CXDI from simulated photon statistics, where the horizontal dashed line indicates the pixel size. a subset of recovered atomic positions near a vacancy (b)-(e) and near a screw dislocation (f)-(k) are shown, where atomic position ME and MAE (a) are also given. (b) For the actual atomic position near a vacancy, there is an atom missing at the center surrounded by an inward distortion of neighboring atoms within 5 Å. (c) This is fully recovered by $2 \times 10^{18}$ ph/μm$^2$. (d) With $1.5 \times 10^{18}$ ph/μm$^2$, the vacancy and distortion can still be identified. (e) By $10^{18}$ ph/μm$^2$, the vacancy is no longer present and only a slight distortion of neighboring atoms is seen. (f) For the actual atomic position near a screw dislocation, a continuous shift of atoms occurs as seen from the [111] direction with characteristic width of 5 Å. (g) This is effectively recovered by $2 \times 10^{18}$ ph/μm$^2$ within the expected resolution. (h) With $4 \times 10^{17}$ ph/μm$^2$, the dislocation can still be recognized. (k) Finally, at $10^{17}$ ph/μm$^2$, only a periodic atomic structure is recovered.

follows a power law decay proportional to $\delta x^{-5}$ [Fig. 4.3(a)], as expected. This power law decay would continue forever for scattering from a sample with uniform electron density. However, for a sample with correlations, in this case long-range order producing Bragg peaks, the cutoff frequency that determines resolution will jump across the regions of increased SNR, as indicated by the sharp drop at $1 \times 10^{18}\,\mathrm{ph/\mu m^2}$ in Fig. 4.3(a), for instance. The resolution at which this curve becomes discontinuous is directly tied to the spatial frequencies of the Bragg peaks. Additionally, the size of the jumps will depend primarily on the relative intensity of the Bragg peaks. From the expected $q^{-4}$ fall off of the intensity away from Bragg peaks, we can estimate the start of the jump by the spatial frequencies where the azimuthally averaged intensity between two Bragg peaks is at its minima. The start of the first jump (derived in Appendix 4.7) is

$$q_1 \approx \frac{q_b}{2}\left(\frac{40\rho+1}{30\rho+1}\right), \tag{4.3}$$

where $\rho = \frac{\left|F_{(000)}\right|^2}{m_b|F_b|^2}$ is the ratio of intensity from the (000) Bragg peak and the lowest non-forbidden reflections at $q_b$, with multiplicity of $m_b$ due to symmetry. Since, the intensities can be obtained from the structure and atomic form factor this can be calculated a priori for known structures. The end of the jump will be given by

$$q_2 \approx \frac{18}{11}q_b - \frac{5}{8}q_1. \tag{4.4}$$

Although the Bragg peaks become more narrow with larger particle size, it does not modify the start and end location of the jump. The reduction in TIPF to reach atomic resolution is thus always the same, albeit the absolute TIPF needed changes.

For crystalline Au, the first jump is due to the {111} Bragg peaks at $q_{111} = 2.67\,\mathrm{\AA^{-1}}$ with $\rho \approx 0.177$. Thus, $q_1 \approx 1.7\,\mathrm{\AA^{-1}}$ and $q_2 \approx 3.3\,\mathrm{\AA^{-1}}$. In other-words, we expect a jump once we reach approximately 1.9 Å resolution and jump to approximately 0.95 Å resolution. As also observed in [Fig. 4.3(a)], this jump results in a factor of 30 reduction in TIPF to reach atomic resolution as compared to the power law decay.

Since achievable resolution from Eqn. 4.2 and from simulated results are a measure of average resolution, we show local resolution of a recovered vacancy and screw dislocation compared to known atomic positions. The known vacancy, as viewed nearly from the [110] direction, is missing a central atom and distorts a small neighborhood of atoms around it [Fig. 4.3(b)]. At $2 \times 10^{18}\,\mathrm{ph/\mu m^2}$, the vacancy is fully recovered, including the full neighboring distortion [Fig. 4.3(c)]. The MAE and ME are within recoverable atom position limits [Fig. 4.3(a)]. At $1.5 \times 10^{18}\,\mathrm{ph/\mu m^2}$, the vacancy is questionable [Fig. 4.3(d)]. A low atomic number atom is present at the center where the vacancy should be and only a slight distortion of the neighboring atoms is observed. This may be misinterpreted as a substitution without additional information. Finally, the vacancy is not recovered for $10^{18}\,\mathrm{ph/\mu m^2}$ [Fig. 4.3(e)]. Only a very slight distortion from the perfectly periodic lattice is recovered. The screw dislocation when viewed from the [111] direction appears as a continuous shift of atoms from one unit cell to the next [Fig. 4.3(f)]. At $2 \times 10^{18}\,\mathrm{ph/\mu m^2}$, this distortion is fully recovered within the pixel resolution [Fig. 4.3(g)]. At $4 \times 10^{17}\,\mathrm{ph/\mu m^2}$, the distortion can be recognized due to its spatial extent, but the atomic position are not correct [Fig. 4.3(h)]. In fact, the distortion is partly in the incorrect direction. Finally, at $1 \times 10^{17}\,\mathrm{ph/\mu m^2}$, the distortion can not be seen any more and a nearly perfectly periodic structure is recovered [Fig. 4.3(k)].

Similarly, the amorphous Au diffraction intensity was simulated with a wide range of TIPF between $3 \times 10^{14}\,\mathrm{ph/\mu m^2}$ and $1 \times 10^{18}\,\mathrm{ph/\mu m^2}$. Again, the resolution obtained using CXDI of these simulations matches very well to the predicted resolution from Eqn. 4.2 until the expected resolution becomes lower than the pixel size. Below approximately $1 \times 10^{16}\,\mathrm{ph/\mu m^2}$ the result is identical to crystalline Au, following the $\delta x^{-5}$ power law decay, since the average electron density is the same for both above 5 Å resolution [Fig. 4.4(a)]. Similar to crystalline Au, amorphous Au exhibits a discontinuity in resolution compared to TIPF because of short-range atomic order resulting in a broad peak in the liquid structure factor. Although the exact discontinuity cannot be determined theoretically, the first jump will be in the vicinity of the closest interatomic distance and will be significantly larger

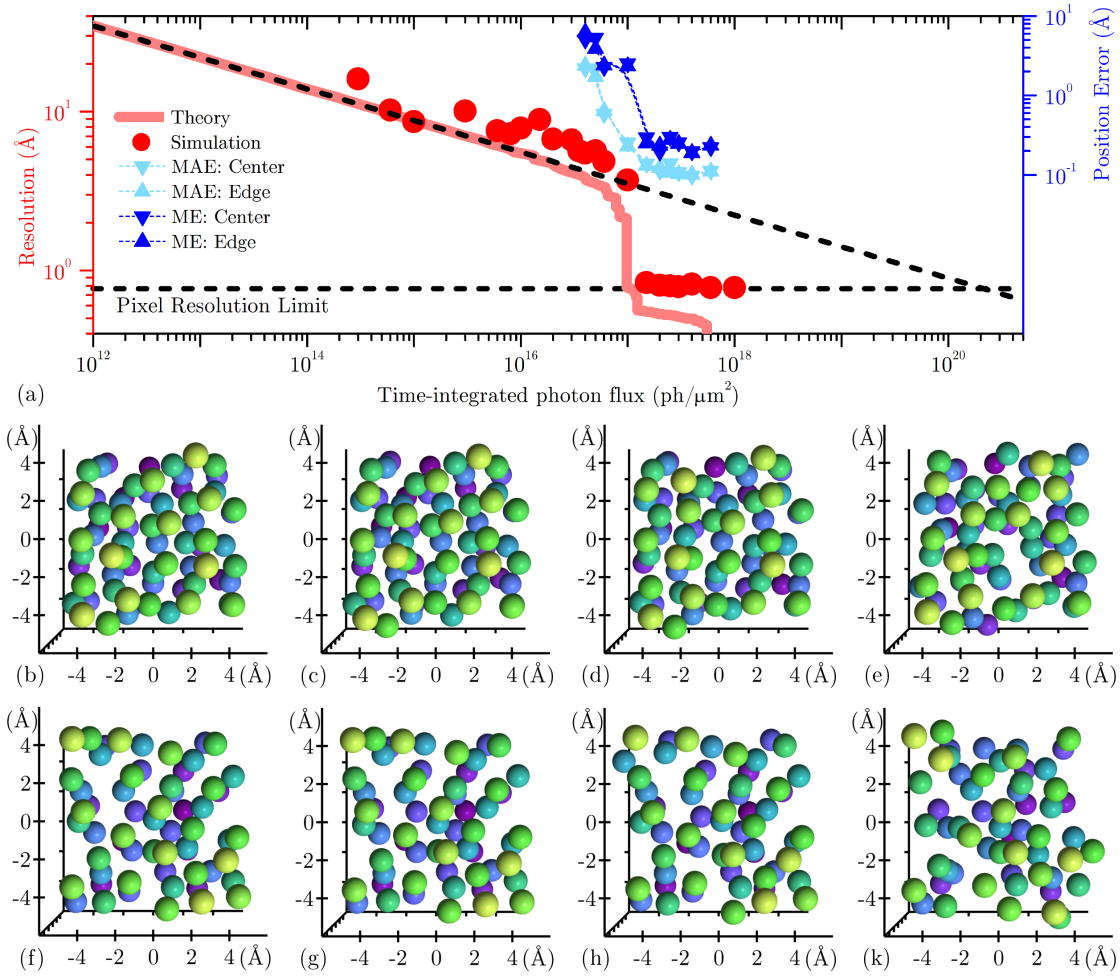


**Figure 4.4**: Amorphous Au particle. (a) Achievable resolution at various photon statistics, where the solid line is the theoretical model described by Eqn. 4.2 and circles are reconstructions using CXDI from simulated photon statistics. The horizontal dashed line indicated the pixel size, below which the current simulations cannot reach and the dashed line which follows much of the theoretical curve indicates the expected $\delta x^{-5}$ fall off for a uniform particle. To show local resolution, a subset of recovered atomic positions at the center (b)-(e) and edge (f)-(k) of the particle are shown, where atomic position ME and MAE (a) are also given. The actual atomic position at the center (b) and edge (f) of the particle are fully recovered by $1.5 \times 10^{17}$ ph/μm$^2$ (c) and (g). At $10^{17}$ ph/μm$^2$ (d) and (h), all but one atom matches the known solution for the center and edge, respectively. Finally at $6 \times 10^{16}$ ph/μm$^2$ (e) and (k), a large number of atomic positions are incorrect.

compared to the crystalline case. For amorphous Au, a jump from 3 Å to the resolution limit of 0.78 Å occurred at $1 \times 10^{17}$ ph/µm$^2$. The jump results in three orders of magnitude reduction in TIPF to reach atomic resolution as compared to the power law decay.

Again, we show local resolution of the recovered particle, this time at its center and at the top edge. The actual atomic positions [Fig. 4.4(b) and (f)] are fully recovered by $1.5 \times 10^{17}$ ph/µm$^2$ [Fig. 4.4(c) and (g)]. At $10^{17}$ ph/µm$^2$ [Fig. 4.4(d) and (h)], all but one atom matches the known solution in both the center and edge region. Finally, at $6 \times 10^{16}$ ph/µm$^2$ [Fig. 4.4(e) and (k)] a large number of atomic positions are incorrect.The ME [Fig. 4.4(a)] shows a clear discontinuity at $1 \times 10^{17}$ ph/µm$^2$, just as predicted by Eqn. 4.2.

Finally, the G-Actin protein diffraction intensity was simulated with a wide range of TIPF between $1 \times 10^{16}$ ph/µm$^2$ and $1 \times 10^{21}$ ph/µm$^2$. The resolution obtained using CXDI of these simulations [Fig. 4.5(a)] matches well to the predicted resolution from Eqn. 4.2. The actual atomic positions are shown in Fig. 4.4(b). Color is again used to indicate depth while size of the spheres indicated the atomic number. Although the electron density is fully recovered by $1 \times 10^{21}$ ph/µm$^2$, the atomic positions cannot be entirely recovered [Fig. 4.5(c)]. Since the closest inter-atomic distances for G-Actin are approximately 1.5 Å, less than the size of two pixels, many atoms are grouped together when identified using the local maxima technique.

Although the exact expected resolution is depended on the material used, some generalizations can be made since inter-atomic distances are similar for all solids. First, the major difference between different materials will be the overall electron density. The two primary examples given thus far are Au with an electron density of 4.18 nm$^{-3}$ within the smallest sphere enclosing the particle and G-Actin with an electron density of $6.89 \times 10^{-2}$ nm$^{-3}$ within the smallest sphere enclosing the particle. Since, the x-ray scattering per sampling condition is effectively proportional to the electron density, G-Actin will require roughly three orders of magnitude more dose than Au. Other examples, such as aluminium (Al), which have very similar crystal structure to Au, will simply be shifted in dose by their

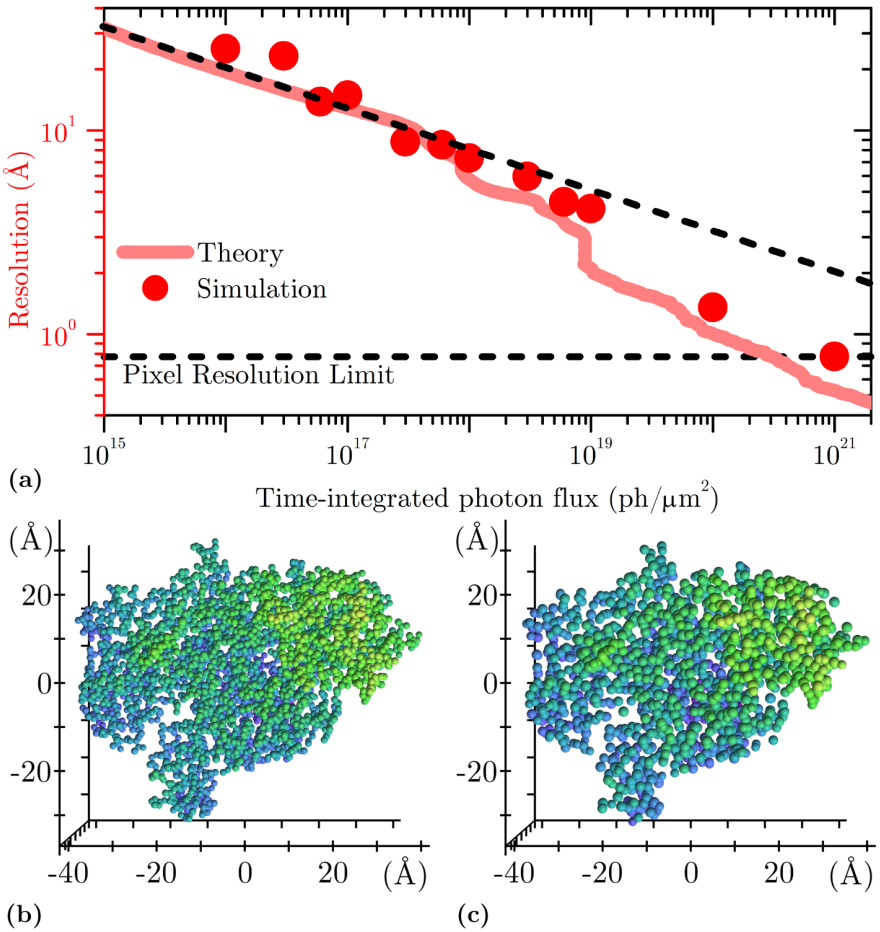


**Figure 4.5**: G-Actin particle. (a) Achievable resolution at various photon statistics, where the solid line is the theoretical model described by Eqn. 4.2 and circles are reconstructions using CXDI from simulated photon statistics. The horizontal dashed line indicated the pixel size, below which the current simulations cannot reach and the dashed line which follows much of the theoretical curve indicates the expected $\delta x^{-5}$ fall off for a uniform particle. The actual atomic position at the of the particle (b) are not recovered at the resolution limit of $1.5 \times 10^{17}$ ph/μm$^2$ (c) due to inter-atomic distance separation being smaller than twice the pixel size.

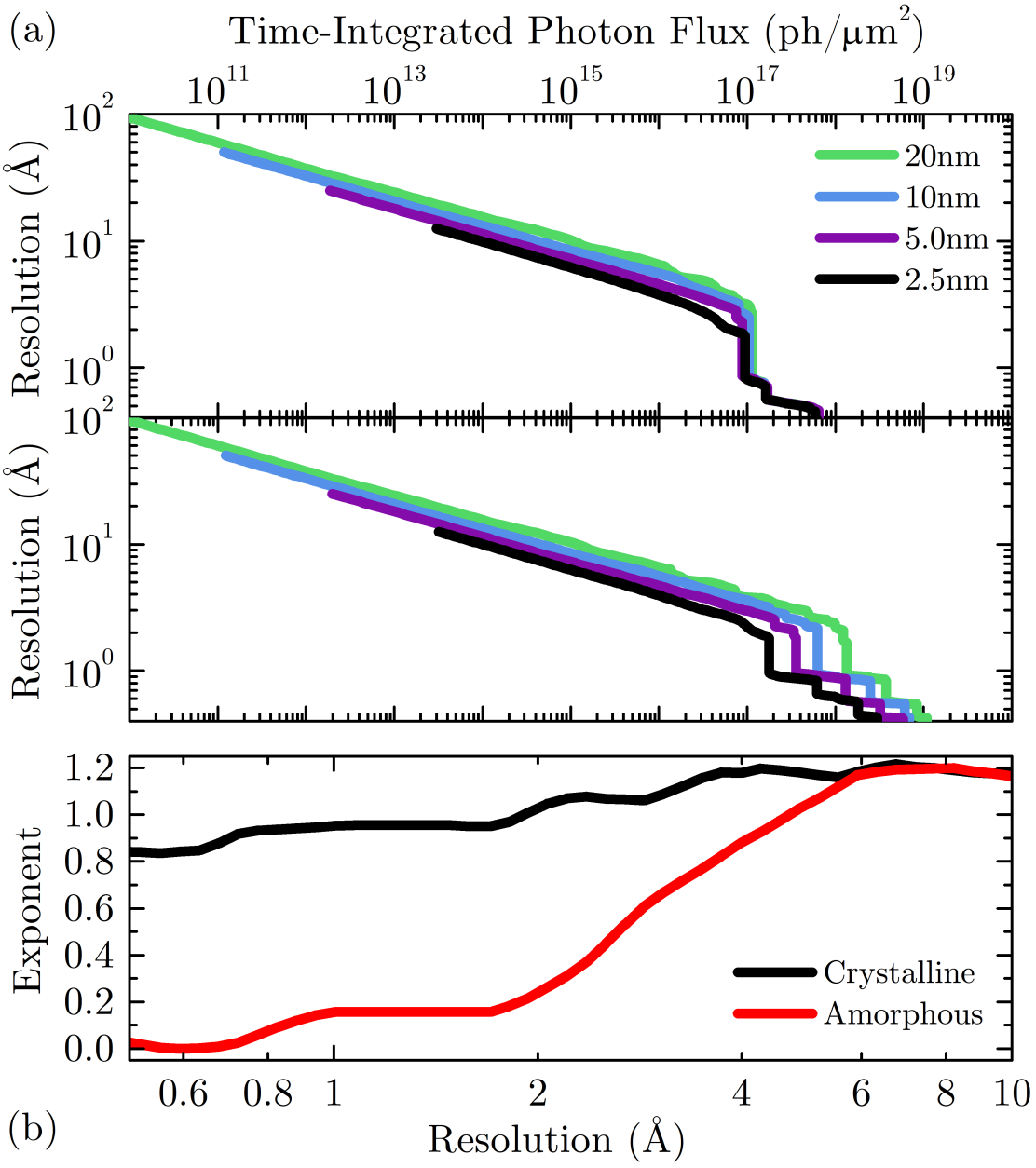


**Figure 4.6**: (a) Theoretical attainable resolution for amorphous Au particles (top panel) and crystalline Au particles (bottom panel) of different sizes; 20 nm (green), 10 nm (blue), 5 nm (purple), and 2.5 nm (black). Amorphous and crystalline Au are identical for resolutions greater than approximately 5 Å. (b) at large resolutions, both amorphous and crystalline particles require TIPF that is linearly proportional to particle size. At atomic resolution, the required TIPF becomes independent of size for amorphous particles.

ratio of electron density squared, in this case a factor of approximately 40. A very important, less obvious change in the scattering is due to the arrangement of atoms themselves. As has already been discussed, the disorder of amorphous materials spreads scattering in Fourier space, allowing a distinct advantage in achieving sufficient SNR for all required spatial frequencies. Real materials will fall between the case of a perfect crystal and ideal amorphous solid, which have been used as examples to illustrate their difference. The next most important change in scattering will occur due the finite size of the particle. Although the additional scattering due to more material will be exactly cancelled due to additional sampling required for larger particles, the scattering distribution is also slightly modified with particle size (fig. 4.6 (a)). As the particle size increases, Bragg peaks including the (000) become more narrow, assuming coherence length is given by the particle size. Thus, larger particles will require more TIPF to achieve the same resolution. the required TIPF to reach a particular resolution is proportional to $\Delta x^n$, where $n$ is the proportionality exponent to the particle size (fig. 4.6 (b)). The arrangement of atoms is unimportant for resolution significantly greater than the atomic scale, where the TIPF is observed to be directly proportional to particle size. Below atomic resolution, the TIPF becomes independent on particle size for amorphous materials, while for crystalline materials remains approximately linearly dependent. As was predicted (section 4.7), the TIPF reduction at atomic resolution is independent of particle size for crystalline materials. In the limit of small particles, the the crystalline and amorphous case become identical.

As mentioned previously, in real experiments a 3D Fourier data set will be created by mapping a series of 2D Fourier slices. Since the slices naturally form cylindrical sampling, a polar or pseudo-polar grid is a natural alternative to the Cartesian grid. In this case a 5 nm amorphous Au particle is reconstructed using the pseudo-polar fast Fourier transform (PPFFT) on a cylindrical grid and for comparison using the FFT on a Cartesian grid. A smaller sized particle is necessary here due to the speed reduction of the PPFFT compared to the FFT, even with highly optimized GPU-accelerated PPFFT code. The reconstructions are almost identical for the Cartesian and cylindrical coordinates, both resolutions are close

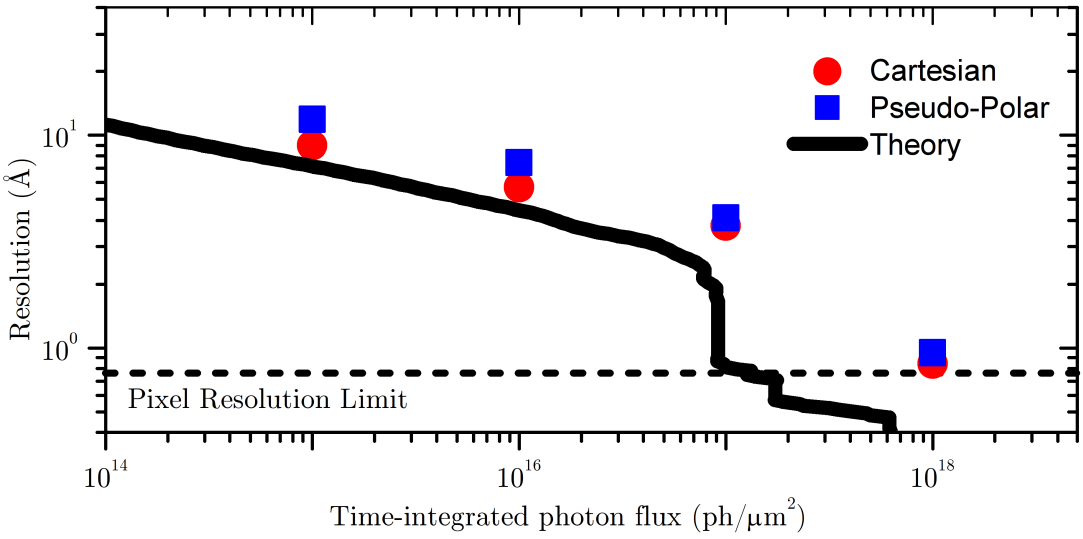


**Figure 4.7**: A 5 nm amorphous Au particle is reconstructed using fast Fourier transform on a Cartesian grid (red circles) and using the pseudo-polar fast Fourier transform on a cylindrical grid (blue squares). Both are close to the theoretical prediction (black solid line)

to the theoretical prediction (fig. 4.7). Although, the use of cylindrical coordinates may mitigate additional errors when mapping the 2D slices, computationally it is not recommended to use the PPFFT over the FFT for CXDI.

## 4.5 Conclusion

The realization of true atomic resolution using CXDI will require a number of technical problems to be resolved, including high dynamic range detectors with high quantum efficiency and low dead time to reduce waste of illuminating photons. Possibly the most challenging and costly requirement is to obtain sufficiently brilliant x-ray sources to perform experiments within reasonable time periods. Current third-generation sources such as APS, Spring-8, NSLS II, and Petra III have a Brilliance of $(5 \times 10^{13}$ to $2 \times 10^{15})$ ph/s μm$^2$ mrad$^2$ 0.1% near 10 keV [86]. Estimates of usable coherent flux suggests these sources require on the order of one year of measuring to reach atomic resolution for materials with high electron density. As an example, one of the best 2D resolutions achieved thus far is 3 nm for a

silver cube using $1 \times 10^{13}$ ph/µm$^2$ [76]. Adjusting for oversampling, electron density, photon energy, and volume fraction a similar measurement on a gold sphere could have achieved a 3D resolution of 2.1 nm using the same TIPF. This falls in line with predictions made by Eqn. 4.2 seen on [Fig. 4.3(a)]. Next generation sources, such as the proposed multi-bend achromat synchrotron and energy recovery linac will provide roughly two orders of magnitude increase in brilliance [87]. This makes achieving atomic resolution a real possibility under ideal conditions for radiation hard-samples. The necessity to increase brilliance of x-ray sources can be alleviated by using partially incoherent radiation for CXDI to increase the usable photons [52, 88]. Even when full atomic resolution cannot be achieved, any order will lower the flux requirement compared to the simple expected power law decay of an equivalent uniform sample. For instance, crystals with large unit cells produce Bragg peaks at low spatial frequencies [89], which can help to image defects on the length scale of the unit cell. We remark that this method of analysis is valid for any material, including organic samples that cannot be crystallized, which may one day be imaged using fast probes [90].

## 4.6 Condition of adequate signal-to-noise

We make use of the Shannon sampling theorem, which states that a band limited signal can be accurately described when sampled at the Nyquist rate [28, 29]. In other words, if a power spectrum is measured only up to some maximum frequency, $q_c$, the best expected average image resolution is $\delta x = \pi/q_c$. Strictly speaking, with the use of a discrete Fourier transform, this will be the pixel size. In order to separate two nearby objects, it is required that they are separated by at least two pixels, so the true image resolution may be thought of as twice the pixel resolution. Resolution numbers in this paper refer to the pixel size that adequately describes the signal of a band limited Fourier spectrum. Although the diffraction of real objects is never truly band limited, the power spectrum rapidly decreases for larger frequencies and a frequency cutoff can be defined for which higher frequencies can no longer be measured reliably within some noise.

In this case, we are not interested in an observer's ability to discern between a signal and noise and thus do not use signal detection theory [91] or the useful simplification of the Rose model [92]. Instead, we are only interested in the spatial frequency where noise significantly alters the power spectrum. In that respect, we look at the signal-to-noise ratio (SNR) averaged over shells of constant q,

$$\langle \mathrm{SNR(q)} \rangle = \langle \frac{\mu(q)}{\sigma(q)} \rangle = \frac{1}{4\pi} \int d\Omega \frac{\mu(\mathbf{q})}{\sigma(\mathbf{q})}. \tag{4.5}$$

Although, most materials are sufficiently isotropic to consider the azimuthal average only, it is possible to define the SNR and spatial resolution along any direction independently. By signal we mean the expected photons scattered from the object of interest captured by a detector of size $a$ with quantum efficiency $\eta$ during time $t$, $\mu(\mathbf{q}) = I(\mathbf{q})\eta a t$. This signal, sometimes referred to as contrast, excludes photons directly from the illumination function, sometimes referred to as unscattered photons in the language of the Born approximation. For CXDI, the object is illuminated approximately by a plane wave, which leads to unscattered photons only near q=0. This is different from traditional microscopy, where the measured photons across the entire image can have significant contribution from photons that do not contribute to the image signal contrast. The total noise, $\sigma(\mathbf{q}) = \sqrt{\mu(q) + \varsigma^2}$, is due to the Poisson statistics of photon shot noise and additional noise introduced by the detector, $\varsigma$. In the limiting case that $\varsigma^2 \ll \mu(q)$ then $\langle \mathrm{SNR(q)} \rangle \approx \langle \sqrt{\mu(q)} \rangle$, the average scattered photon amplitude. In the other case, when $\varsigma^2 \gg \mu(q)$, $\langle \mathrm{SNR(q)} \rangle \approx \frac{\langle \mu(\mathbf{q}) \rangle}{\varsigma}$. To continue further, we must assume that the sample scatters photons relatively isotropically, such that variations in $\mu(q)$ are small for constant $q$. Later, we will see that this is not strictly necessary.

$$\begin{aligned} \langle \mathrm{SNR(q)} \rangle &\approx \frac{\langle \mu(q) \rangle}{\langle \sigma(q) \rangle} = \\ &\frac{\langle \mu(q) \rangle}{\sqrt{\langle \mu(q) \rangle + \varsigma^2}} \langle \sqrt{1 + \frac{\mu(\mathbf{q}) - \langle \mu(q) \rangle}{\langle \mu(q) \rangle + \varsigma^2}} \rangle^{-1}. \end{aligned} \tag{4.6}$$

As we have already assumed, the variations in $\mu(q)$ are small; thus, $\frac{\mu(\mathbf{q}) - \langle \mu(q) \rangle}{\langle \mu(q) \rangle}$ is

also small and we may expand this term to first order to find,

$$\langle \mathrm{SNR(q)} \rangle \approx \frac{\langle \mu(q) \rangle}{\sqrt{\langle \mu(q) \rangle + \varsigma^2}} \left[ 1 - \frac{1}{2} \langle \frac{\mu(\mathbf{q}) - \langle \mu(q) \rangle}{\langle \mu(q) \rangle + \varsigma^2} \rangle \right]^{-1}$$
$$= \frac{\langle \mu(q) \rangle}{\sqrt{\langle \mu(q) \rangle + \varsigma^2}}. \tag{4.7}$$

We are interested in the maximum spatial frequency, $q_c$, for which the average SNR is above some threshold, $\gamma$, for all $q \leq q_c$. Using Eqn. 4.7, we find that

$$\langle I(q \leq q_c) \rangle \eta a t \geq \frac{\gamma^2}{2} \left[ 1 + \sqrt{1 + 4\frac{\varsigma^2}{\gamma^2}} \right] \tag{4.8}$$

Since we are interested in the smallest spatial frequency where the average SNR falls below some threshold, we are primarily concerned with regions of Fourier space to which few photons scatter. For non-isotropically scattering samples, such as crystals, it is the signal between Bragg peaks that will define $q_c$. Thus, Eqn. 4.8 holds even for scattering from crystals.

## 4.7 Crystalline discontinuities

For crystalline materials, it is possible to determine when the expected resolution will become discontinuous as a function of dose. Since, it is the regions of low SNR that determine the resolution, the cutoff frequency (Eqn. 4.8) will jump across regions of high SNR, such as Bragg peaks. Far from a Bragg peak, the asymptotic form of the scattered intensity can be used. Thus, the (000) contribution to the azimuthally averaged intensity is then,

$$\langle I_0 \rangle \propto \frac{Z^2}{q^4}, \tag{4.9}$$

where the atomic scattering factor, $f(q = 0) = Z$, is the atomic number. It is not important to know the absolute intensity, since only the ratio of two Bragg peak intensities will later be used. The contribution from any other Bragg peak at $q_b \neq 0$ to the azimuthally averaged intensity has the asymptotic form

$$\langle I_b \rangle \propto \frac{m_b |f(q_b)|^2}{4 q q_b (q - q_b)^2}, \tag{4.10}$$

where $m_b$ is the peak multiplicity, given by the number of symmetry-equivalent reflections. The first discontinuity will be due to a jump across the first non-forbidden Bragg peak, scaled by an additional factor of inverse wavevector due to rotation in three dimensions as seen in Eqn. 4.2. The start of this jump is determined by the minima in inter-peak intensity and is given by $\frac{\mathrm{d}}{\mathrm{d}q}\left[\frac{1}{q}\left(\langle I_0\rangle + \langle I_b\rangle\right)\right]|_{q_1} = 0$. Using Eqns. 4.9 and 4.10 a quadratic expression is obtained,

$$10\rho_{0,b}(q_b - q_1)^3 q_b = q_1^3(2q_1 - q_b), \tag{4.11}$$

where $\rho_{0,b} = \frac{Z^2}{m_b|f(q_b)|^2}$. This has four roots, one of which is the correct turnover point between $q = 0$ and $q_b$. Although the analytic roots can be written, they are generally far too complicated to be used directly. The recommendation is to find the numeric root. Nonetheless, an approximate analytic root can be found by looking near $q_b/2$, half way between the two Bragg peaks. Using a first-order Taylor series expansion, the approximate turn over point is given by

$$q_1 \approx \frac{q_b}{2}\left(\frac{40\rho_{0,b}+1}{30\rho_{0,b}+1}\right), \tag{4.12}$$

which is valid when $\rho_{0,b} \sim 10^{-1}$. The jump ends when the same intensity is reached on the other side of the first Bragg peak. Thus, if this Bragg peak is sufficiently separated from others, such that a low intensity region exists directly after the peak at $q_b$, then the end point is given by

$$q_2^2(q_2 - q_b)^2 = q_1^2(q_b - q_1)^2/\alpha, \tag{4.13}$$

where $\alpha = 1 + 4\rho_{0,b}\frac{q_b(q_b-q_1)^2}{q_1^3}$. This quadratic equation has analytic roots, but once again, it is simpler to calculated the solution numerically. It is also possible to estimate the end point by looking for a root near $2q_b - q_1$, which has the same separation as the start point to the Bragg center. By doing a first-order Taylor series expansion, the end point is given be

$$\begin{aligned} q_2 &\approx 2q_b - q_1 - \frac{(q_b - q_1)[(2q_b - q_1)^2 - q_1^2/\alpha]}{2(2q_b - q_1)(3q_b - 2q_1)} \\ &\approx \frac{18}{11}q_b - \frac{5}{8}q_1, \end{aligned} \tag{4.14}$$

where the second approximations assumes the intensity at $q_1$ is dominated by $\langle I_b\rangle$. By following the same method, the jumps across higher Bragg peaks can also be determined, but are not derived here.

## 4.8 Acknowledgments

This work was supported by U.S. Department of Energy, Office of Science, Office of Basic Energy Sciences, under Contract DE-SC0001805.

Chapter 4, in part, has been submitted for publication as it may appear in *J. Synchrotron Radiat.* (2015). S. H. Dietze and O. G. Shpyrko "Coherent diffractive imaging: Achieving atomic resolution." The dissertation author was the primary investigator and author of this paper.

# Chapter 5

# Magnetic Materials

## 5.1 Introduction

Understanding the electronic structure at the nanoscale is crucial to untangling fundamental physics puzzles, including emergent behaviour in 3d and 4f orbital systems. Such systems often display interesting magnetic order over various length scales. The magnetic domain formation and propagation is strongly influenced by defects and interfaces in the material, which are critical in influencing the design of magnetic memory [93] and use of giant magnetoresistance in spintronic technology [94].

Multilayer thin films are made of alternating magnetic layers, such as a rare-earths and a transition metals. Although each material is ferromagnetic, the two materials couple through a negative exchange and thus prefer to have their magnetic moments be anti-parallel. Since the magnetic moments are at least partially compensated, a lower demagnetization field can exist with the moments orientation out of the thin film plane, which gives rise to a perpendicular magnetic anisotropy (PMA). These films break up into a domain configuration with alternating up and down magnetization, whose characteristic width is determined by the strength of the intra-material exchange energy and demagnetization field energy. For instance, GdFe with nominal thickness of 100 nm will have domain widths on the order of 300 nm. Since the film thickness is still quite large, reducing the thickness will give smaller domains, until the dipolar length is reached [95, 96, 97]. The domains

are separated by domain walls, where magnetic moments smoothly rotate from one configuration at an edge to the opposite configuration at the other edge. The domain wall width is determined mostly by the intra-material exchange energy and magnetic anisotropy. Once, again for GdFe, the domain walls are approximately 30 nm thick.

The imaging of such nanoscale domain structures has been one of the driving forces to developing techniques such as magnetic force microscopy (MFM) and x-ray microscopy. Although MFM has a much higher availability, it suffers in many ways that x-rays do not. For instance, MFMs rely on stray magnetic fields near a surface that is scanned. Thus, magnetically compensated, buried structures, or materials with large thickness variations cannot be accessed, whereas x-rays can penetrate bulk materials to obtain a projected image with chemical sensitivity by using x-ray resonant edges. In addition, since magnetic domains can be "soft," the magnetic tip of an MFM can drag domain walls during scanning, altering the domain configuration.

Up until recently, the x-ray community has had a single tool—Scanning transmission x-ray microscopy (STXM)—to image magnetic domain configurations [98]. Even though it has had great success, it has several experimental limitations. STXM requires a high degree of circular polarization with the ability to switch helicity. In addition, it's biggest drawback is that it's resolution is due to the precise scanning of a highly focused beam. Therefore, it suffers from the usual problems in resolution, namely errors in alignment, motor position, field of view, and focal plane. These errors are virtually eliminated with the use of CDI. In section 5.2, the magnetic scattering contrast will be reviewed. Then, in section 5.3, it will be shown how CDI can be used to image magnetic thin films using only linear polarization.

## 5.2 X-ray resonant exchange scattering

As was briefly discussed in section 2.6, the scattering cross-section greatly increases near energies characteristic of the atomic electron energy levels, such that

a photon can be absorbed and an electron excited from a core shell to a higher level with a vacancy. An atom that is magnetized, has a net electron spin polarization and thus a difference in the available vacancies. The difference in occupancy results in a different cross section for various photon polarizations.

Although both the electric and magnetic multipole transitions contribute to the resonant exchange scattering, the electric dipole transition dominates the $M_{4,5}$ absorption edges. The resonant scattering factor can be written in the form [99],

$$f_{E1}^{XRES} = (\hat{\boldsymbol{\epsilon}}_0^* \cdot \hat{\boldsymbol{\epsilon}}_f)F^{(0)} - i(\hat{\boldsymbol{\epsilon}}_0^* \times \hat{\boldsymbol{\epsilon}}_f) \cdot \hat{\mathbf{m}}F^{(1)} + (\hat{\boldsymbol{\epsilon}}_0^* \cdot \hat{\mathbf{m}})(\hat{\boldsymbol{\epsilon}}_f \cdot \hat{\mathbf{m}})F^{(2)}, \tag{5.1}$$

where $\hat{\boldsymbol{\epsilon}}_0$ and $\hat{\boldsymbol{\epsilon}}_f$ are the incoming and outgoing photon polarization, respectively. The scattering factors, $F^{(1,2,3)}$, are linear combinations of the atomic oscillator strengths, which depend on the probability for a transition between two states at a particular energy, as given by Fermi's Golden rule. When relating these scattering factors to the complex index of refraction (eq. (2.18)), it becomes clear that $F^{(1)}$ and $F^{(2)}$ are the x-ray circular and linear dichroism, respectively. When the photon propagation is aligned with the magnetization moment, the good photon eigenstates are circularly polarized and the circular dichroism gives the Faraday effect in bulk material. Similarly, when the photon propagation is perpendicular to the magnetization moment, the good photon eigenstates are linearly polarized and the linear dichroism results in the Voigt effect.

## 5.3 Magnetic thin films

Since for thin films with PMA, most of the magnetic moments are oriented out of plane, the linear dichroism contribution from magnetization parallel to the film will be negligible for small angle scattering, normal to the surface. Thus, the non-zero contributions to the resonant scattering are

$$\begin{pmatrix} f_{E1}^{\pi\to\pi} \\ f_{E1}^{\pi\to\sigma} \end{pmatrix} = \begin{pmatrix} 1 \\ 0 \end{pmatrix} F^{(0)} - i \begin{pmatrix} 0 \\ 1 \end{pmatrix} \hat{\mathbf{m}}_\perp F^{(1)} + \mathcal{O}\left(\hat{\mathbf{m}}_\parallel^2\right) F^{(2)}. \tag{5.2}$$

It has been written in this way only to illustrate that charge scattering results in no polarization change when using linear polarized light, while magnetically scattered

photons due to circular dichroism become orthogonally polarized. This gives the possibility of separating these contributions when using linearly polarized light, given a detector that is sensitive to polarization. Since the good eigenstates are circularly polarized photons, the non-zero contributions to the resonant scattering can also be written as

$$\begin{pmatrix} f_{E1}^{+\to+} \\ f_{E1}^{-\to-} \end{pmatrix} = \begin{pmatrix} 1 \\ 1 \end{pmatrix} F^{(0)} + \begin{pmatrix} 1 \\ -1 \end{pmatrix} \hat{\mathbf{m}}_{\perp} F^{(1)} + \mathcal{O}\left(\hat{\mathbf{m}}_{\parallel}^2\right) F^{(2)}. \tag{5.3}$$

The contribution of circular dichroism is opposite for left-handed (indicated by the plus sign) and right-handed (indicated by the minus sign) circularly polarized light, as must be the case to maintain symmetry. Since the linear dichroism is generally weaker than the circular dichroism and since the scattering strength depends on the in-plane magnetization squared, only a small portion of domain walls and closure domains will contribute. Thus, the contribution from this can be safely ignored for thin films with PMA.

Using the Helmholtz propagation through a thin film (eq. (2.10)), the exit wavefield for each polarization is given by

$$\psi_{\pm}(\mathbf{r}_{\perp}) = P(\mathbf{r}_{\perp}) e^{-ia_l[f_l^0 + F_l^{(0)}] z_l(\mathbf{r}_{\perp})} e^{\mp i a_l F_l^{(1)} m_{\hat{\mathbf{z}},l}(\mathbf{r}_{\perp})}, \tag{5.4}$$

where $P(\mathbf{r}_{\perp})$ is the illumination function, $a_l = \lambda N_l r_e$ and $m_{\hat{\mathbf{z}},l}(\mathbf{r}_{\perp}) = \int_0^z \hat{\mathbf{m}}_{\hat{\mathbf{z}},l}(\mathbf{r})\, dz$ is the projection of the magnetization along the propagation direction. The constant phase factor due to free space propagation has been ignored, as it will be lost in the measured intensity regardless. The index represents the Einstein summation over all materials. Although, the resonant contributions can in general be from multiple materials at once, it is common for only a single contribution to be significant at any particular energy. The far-field intensity using linear polarization is

$$I(\mathbf{q}_{\perp}) = \tfrac{1}{2} \left| \mathscr{F}\left\{\psi_{+}(\mathbf{r}_{\perp})\right\} \right|^2 + \tfrac{1}{2} \left| \mathscr{F}\left\{\psi_{-}(\mathbf{r}_{\perp})\right\} \right|^2. \tag{5.5}$$

In the next section, special cases are explored, which can be used to more easily separate the contribution from charge and magnetic scattering.

## 5.4 Special cases of magnetic thin films

The scattering intensity from a thin film with PMA using linear polarization can in general be written as,

$$\begin{aligned} I(\mathbf{q}_\perp) &= \left|\mathscr{F}\left\{P(\mathbf{r}_\perp)C(\mathbf{r}_\perp)\cosh\left[iM(\mathbf{r}_\perp)\right]\right\}\right|^2 \\ &+ \left|\mathscr{F}\left\{P(\mathbf{r}_\perp)C(\mathbf{r}_\perp)\sinh\left[iM(\mathbf{r}_\perp)\right]\right\}\right|^2 \end{aligned}, \tag{5.6}$$

where $C(\mathbf{r}_\perp) = e^{-ia_l[f_l^0+F_l^{(0)}]z_l(\mathbf{r}_\perp)}$ can be considered the charge contribution and $M(\mathbf{r}_\perp) = a_l F_l^{(1)} m_{\hat{\mathbf{z}},l}(\mathbf{r}_\perp)$ can be considered the magnetic contribution. If the magnetic contribution is weak, $M(\mathbf{r}_\perp) \ll 1$, the intensity simplifies to

$$I(\mathbf{q}_\perp) = \left|\mathscr{F}\left\{P(\mathbf{r}_\perp)C(\mathbf{r}_\perp)\right\}\right|^2 + \left|\mathscr{F}\left\{P(\mathbf{r}_\perp)C(\mathbf{r}_\perp)M(\mathbf{r}_\perp)\right\}\right|^2. \tag{5.7}$$

As an example, rare-earth metals typically need to be significantly less than 20 nm for the maximum resonant contribution to be in this regime. This further simplifies when the thin film is of uniform thickness,

$$I(\mathbf{q}_\perp) = |C|^2\left(I_{\mathrm{WF}} + \left|\mathscr{F}\left\{P(\mathbf{r}_\perp)M(\mathbf{r}_\perp)\right\}\right|^2\right], \tag{5.8}$$

where $|C|^2$ is a constant attenuation factor and $I_{\mathrm{WF}} = \left|\mathscr{F}\left\{P(\mathbf{r}_\perp)\right\}\right|^2$ is the far field diffraction intensity from the illumination function without a sample, termed the white field. In this case, it is easy to separate the two contributions since the white field can easily be measured very accurately, allowing the magnetic domain structure to be directly reconstructed.

However, even if the film is not sufficiently thin, yet the magnetization is fully aligned in either of the directions parallel to the wavefield propagation, then $m_{\hat{\mathbf{z}},l} = \hat{\mathbf{m}}_{\hat{\mathbf{z}},l} z_l = \pm z_l$. In this case, $(m_{\hat{\mathbf{z}},l})^n = \hat{\mathbf{m}}_{\hat{\mathbf{z}},l}(z_l)^n$ when $n$ is odd and $(m_{\hat{\mathbf{z}},l})^n = (z_l)^n$ when $n$ is even. Therefore when the film is of uniform thickness and only a single resonant contribution exists

$$I(\mathbf{q}_\perp) = |C|^2\left(c_+ I_{\mathrm{WF}} + c_-\left|\mathscr{F}\left\{P(\mathbf{r}_\perp)\hat{\mathbf{m}}_z(\mathbf{r}_\perp)\right\}\right|^2\right], \tag{5.9}$$

where $c_\pm = \frac{1}{2}\cosh\left(2a\Im\left\{F^{(1)}\right\}z\right) \pm \frac{1}{2}\cos\left(2a\Re\left\{F^{(1)}\right\}z\right)$. Up to some scaling factors, this is identical to the weak scattering uniform thickness case. An approximate subtraction can also be made when the charge scattering is not completely

uniform. Consider the case where $z_l = \langle z \rangle_l + \delta z_l$, then

$$\begin{aligned} I(\mathbf{q}_\perp) \approx & \left|\langle C \rangle\right|^2 \left[ I_{\mathrm{WF}} + \left| \mathscr{F}\left\{ P(\mathbf{r}_\perp) M(\mathbf{r}_\perp) \right\} \right|^2 \right. \\ & \left. + 2\Re\left\{ \mathscr{F}\left\{ P(\mathbf{r}_\perp) \right\}^* \mathscr{F}\left\{ P(\mathbf{r}_\perp) \delta C(\mathbf{r}_\perp) \right\} \right\} + \mathcal{O}\left( \delta C^2, M \delta C \right) \right], \end{aligned} \tag{5.10}$$

where $\left|\langle C \rangle\right|^2 = \prod_l \exp\left( 2 a_l \Im\left\{ F_l^{(0)} \right\} \langle z \rangle_l \right)$ is the mean attenuation factor and $\delta C(\mathbf{r}) \approx -\sum_l i a_l [f_l^0 + F_l^{(0)}] \delta z_l(\mathbf{r}_\perp)$ is the variation in charge contribution. The error is expected to be small when the variations in thickness are truly small and the magnetic scattering is reasonably small. The charge variation and magnetic cross term is expected to be very small, as the magnetic scattering tends to occur at higher spatial frequencies due to finite domain width, where as charge scattering tends to be larger towards very low spatial frequencies. It is assumed that only a single element contributes to the magnetic scattering at any given energy. Then two measurements (eq. (5.10)) can be made at different energies near a resonant edge in order to make an approximate separation of the magnetic scattering,

$$\frac{I(E_1)}{\left|\langle O \rangle(E_1)\right|^2} - \frac{S I(E_2)}{\left|\langle O \rangle(E_2)\right|^2} + (S-1) I_{\mathrm{WF}} \approx \left| a \mathscr{F}\left\{ P m_{\hat{\mathbf{z}}} \right\} \right|^2 \left[ \left| F^{(1)}(E_1) \right|^2 - \left| F^{(1)}(E_2) \right|^2 \right], \tag{5.11}$$

where $S \approx \Re\left\{ \sum_l \frac{f_l^0 + F_l^{(0)}(E_1)}{f_l^0 + F_l^{(0)}(E_2)} \right\}$. Ideally, the magnetic scattering should be as different as possible for the two energies. In addition, the separation is most accurate when the ratio of the charge scattering is primarily real.

## 5.5 CDI of uniform thickness GdFe

GdFe multilayer, consisting of approximately 200 alternating layers of atomically thick Gd and Fe layers, was deposited uniformly onto a SiN window to allow transmission of x-rays through the sample. The sample is illuminated, normal to the thin film, with linearly polarized coherent x-rays several millimeters downstream from a 10 µm circular pinhole. The sample is illuminated in a 4 by 4 grid, with 3 µm steps, giving a field of view of 19 µm by 19 µm. When the photon energy is on the Gd $M_5$ resonant edge at 1189 eV, the scattering contains magnetic contribution as given by eq. (5.5) (fig. 5.1 (a)). Since the sample is uniform, the scattering simplifies to the special case such that the magnetic scattering can be

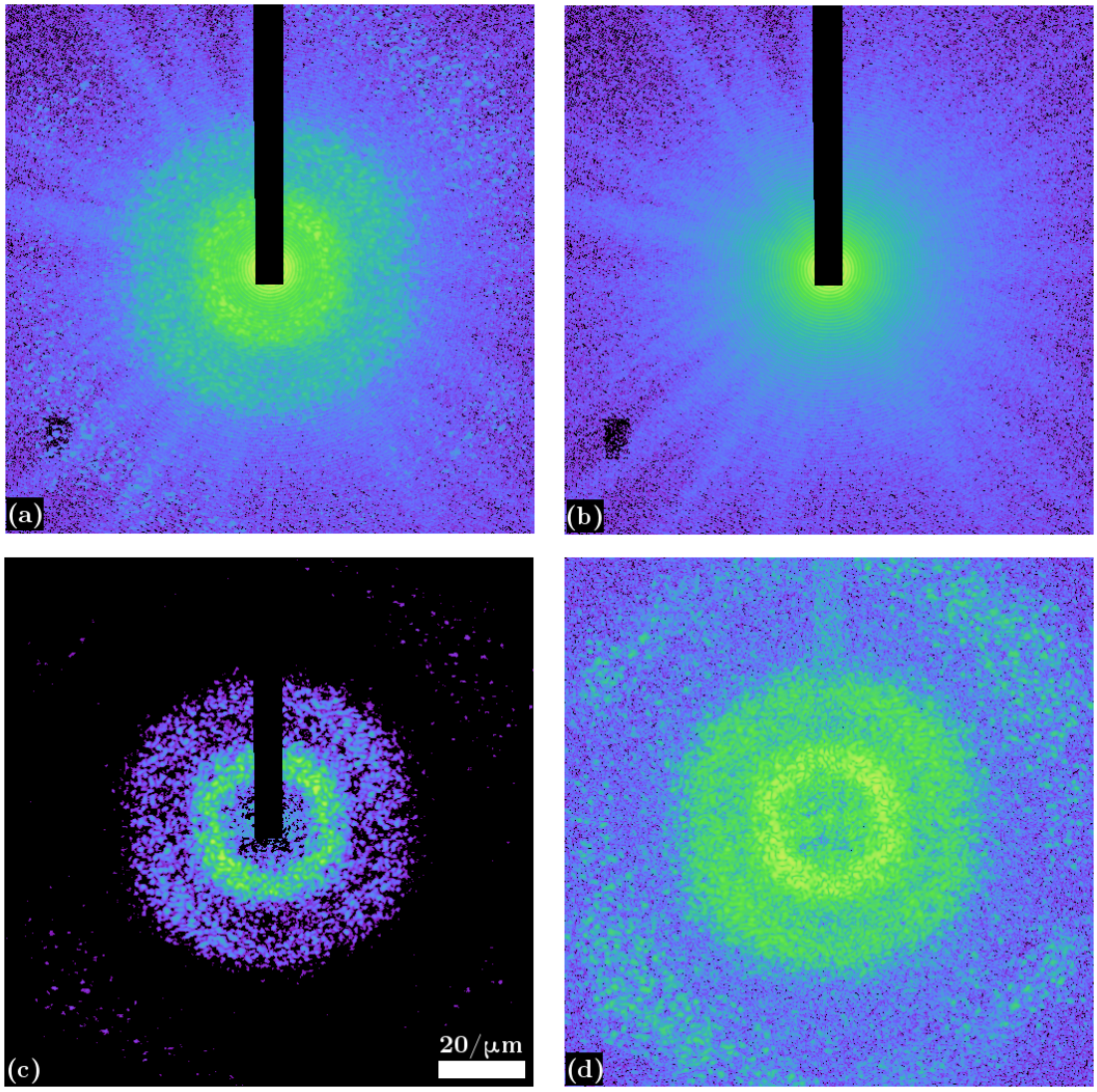


**Figure 5.1**: Scattering from uniform GdFe, where all patterns are diffraction amplitudes on log scale. (a) On resonance scattering at 1189 eV. Off resonance scattering at 1180 eV. (c) Magnetic scattering obtained by subtracting the scaled off resonance scattering from the on resonance scattering. (d) Diffraction amplitude with recovered part behind beamstop after phase retrieval.

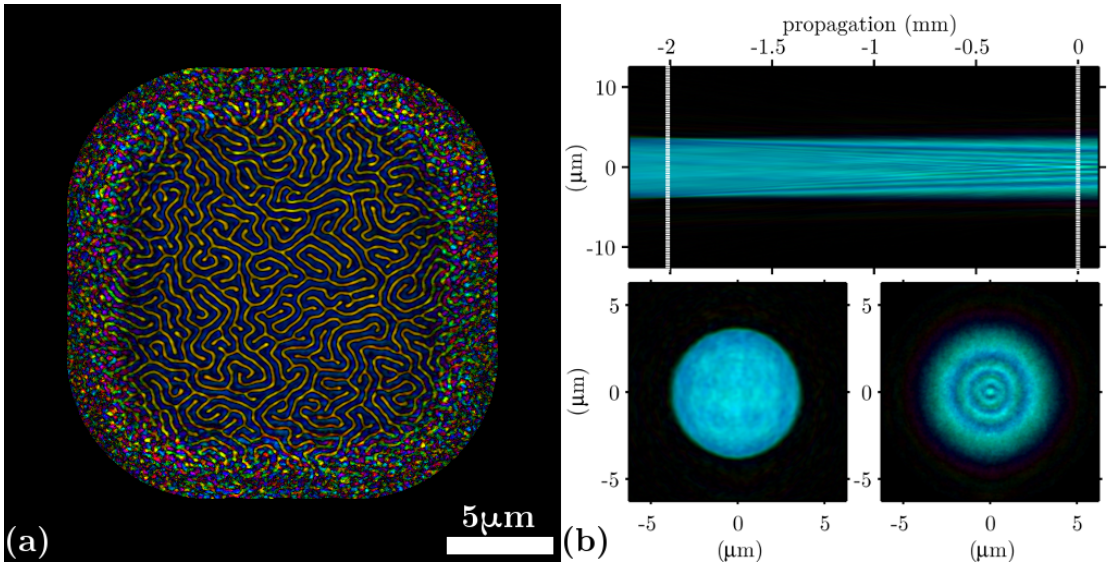


**Figure 5.2**: Reconstruction of the full complex field from a charge uniform sample of GdFe thin film. (a) The field is equated with scattering due to magnetic domains. The yellow and blue indicate magnetization in and out of the image plane. (b) Reconstructed probe at the sample plane (bottom right), that when propagated back 2 mm (top: slice through side view) gives a reasonable circular pinhole (bottom left).

separated (eq. (5.7)). When the sample is illuminated with photons just off the resonant edge at 1180 eV (fig. 5.1 (b)), there is no charge scattering contribution from the sample. The scattering is identical to the scattering from the pinhole without the sample in place, with uniform attenuation. The magnetic scattering (fig. 5.1 (c)) is obtained by subtracting a scaled version of the pinhole scattering from the sample scattering. In this case, the magnetic scattering is primarily real, as observed by the centrosymmetry in the diffraction pattern. Thus, some of the data behind the beamstop is filled in and used as a guide during the initial iterations of phase retrieval. Phase retrieval is performed on the set of 16 magnetic diffraction data. During this process, all of the data behind the beam stop is recovered (fig. 5.1 (d)).

An average of thirty reconstructions is shown in fig. 5.2. The object (fig. 5.2 (a)) shows essentially a two state system, with nearly constant amplitude and two phases, arbitrarily identified as 0 and $\pi$. Since any constant phase shifted solution is also correct, it is not possible to identify which of the two domains are along the

direction of the photon propagation versus opposite, until external magnetic field is applied to break the symmetry. The domain pattern shows labyrinth or maze order. This type of pattern is commonly found in a wide class of uniaxially modulated systems, including Langmuir monolayers, diblock copolymers, liquid crystals, and magnetic thin films [100]. The characteristic length scale corresponding to the width of the stripe is defined by the energetic balance between short range exchange interaction and long range dipolar field interaction. The majority phase domain width is (200 to 300) nm wide, while the minority phase is extremely consistent at 200 nm wide. The pattern shows only a few disclination, or Y-shaped branches leading to a "cul-de-sac." These tend to occur in the minority phase, as the sample is brought from magnetic saturation toward the remanence point, when the domain walls cannot collectively propagate quickly enough, due to pinning. Indeed, the magnetic domain pattern of this uniform GdFe is consistent with that from samples with very few defects [101, 102], even giving nematic order. Since the applied magnetic field evolution is always slow here, the domain configuration shows no "comb" structure that are typical during quenching [103, 104].

The probe used to illuminate the sample is simultaneously recovered (fig. 5.2 (b) bottom right). It shows a high degree of circular symmetry. The probe can be propagated (section 2.4), to find the wavefield in an arbitrary plane (slice seen in fig. 5.2 (b) top). When the probe is propagated backwards approximately 2 mm to the pinhole plane, it reveals a nearly uniform circular pinhole, as expected.

## 5.6 CDI of GdFe with patterned Au

Au:GdFe multilayer, consisting of Au patterns 10 nm tick of various lateral size deposited onto a SiN window to allow x-ray transmission through the sample. On top of the Au patterns is approximately 200 uniform alternating layers of atomically thick Gd and Fe layers. The sample is illuminated, normal to the thin film, with linearly polarized coherent x-rays several millimeters downstream from a 13 µm circular pinhole. The sample is illuminated in a 4 by 4 grid, with 3 µm steps, giving a field of view of 22 µm by 22 µm. When the photon energy is on

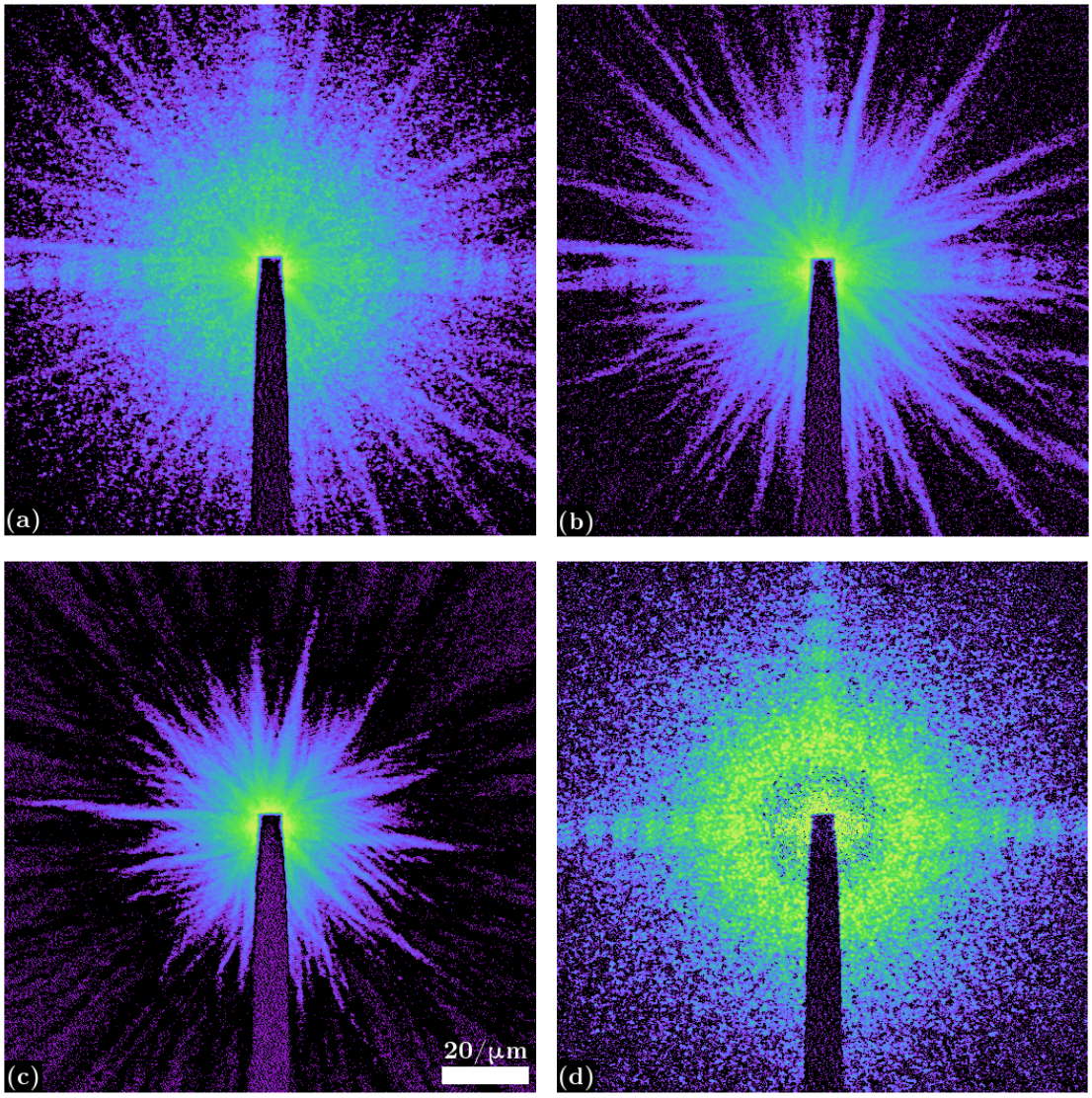


**Figure 5.3**: Scattering from GdFe with pattern Au, where all patterns are diffraction amplitudes on log scale. (a) On resonance scattering at 1189 eV. Off resonance scattering at 1180 eV. (c) Scattering from the pinhole without the sample in place. (d) Magnetic scattering obtained by subtracting the scaled off resonance and pinhole scattering from the on resonance scattering.

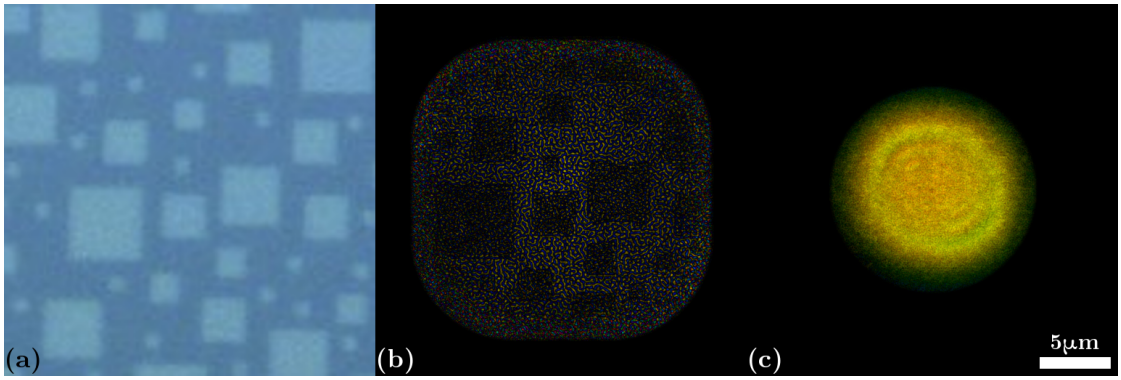


**Figure 5.4**: Partial reconstruction of the full complex field from a thin film sample of GdFe with Au structures. (a) Visible light microscope reveals the Au structure in the region of ptychography. (b) The recovered full complex field at the sample plane due to scattering from magnetic domains. The yellow and blue indicate magnetization in and out of the image plane. Variation in amplitude could structure variations and matches well the expected Au structure. (c) Reconstructed illumination function.

the Gd $M_5$ resonant edge at 1189 eV, the scattering contains magnetic and charge contribution as given by eq. (5.5) (fig. 5.3 (a)). When the sample is illuminated with photons just off the resonant edge at 1180 eV (fig. 5.3 (b)), there is a small contribution from the sample to charge scattering as compared to the scattering from the pinhole along (fig. 5.3 (c)). Since the sample charge scattering is so weak, an approximate magnetic scattering (fig. 5.3 (d)) can be obtained using eq. (5.11), where $S = 1.3$ was used. In this case, the magnetic scattering is primarily real, as observed by the centrosymmetry in the diffraction pattern. Thus, some of the data behind the beamstop is filled in and used as a guide during the initial iterations of phase retrieval. Since the primary error of the magnetic scattering occurs at low spatial frequencies due to strong charge scattering signal in this region, a high pass filter is used to dampen these spatial frequencies. This would not work in the case where the magnetic scattering is not contained within such a nice ring (i.e. with large degree of disorder). Phase retrieval is performed on the set of 16 magnetic diffraction data.

The large charge structure can be seen optically due to the high reflectivity of Au (fig. 5.4 (a)). In the region of the performed ptychography, the charge struc-

ture consists of squares in varying size from (1 to 5) µm, evenly distributed across the sample. The recovered magnetic object is an average of twenty reconstructions (fig. 5.4 (b)). The charge structure of squares can immediately be identified, seemingly as additional absorption or less projected magnetization in the region of magnetic squares. The addition of Au, however, only accounts for a maximum of 7 % absorption, significantly less than the amplitude variation observed. The magnetic reconstruction should also be entirely absent of the Au structure, if the subtraction of diffraction patterns was done appropriately. A second observation of the reconstruction is that the domain width within the region of Au structure is only approximately 75 nm, significantly smaller that outside of the Au structure where the domain width is approximately 125 nm. In fact, these smaller domains are at the limit of the pixel size and their repeatability between reconstructions is slightly lower than that for the larger domains. This in itself results in a slightly lower amplitude within the Au structure when an average is taken, yet still not sufficient to account for the observed amplitude change. This indicates that the projected Gd magnetic moment is lower, either due to partial misalignment of the moment or due to an overall less thickness of the GdFe layer. The lower thickness is consistent with a smaller domain size within the Au structure, however, the expected change in domains size should not be by a factor of two. Although bulk Au is diamagnetic, nanostructures of Au are known to become ferromagnetic [105, 106]. To account for the smaller domain width, it is possible that a significant portion of the Au moments are aligned with the Gd-Fe combined magnetic moment. Overall, the magnetic domains are far less consistent in width and have far more disclinations as compared to the uniform GdFe, suggesting that the patterning of Au structures results in variations in the sample for nucleation of domains and pinning of domain walls to occur.

The probe used to illuminate the sample is simultaneously recovered (fig. 5.4 (c)). Although it appears quite circular, it contains significant variation that break symmetry. When the probe is propagated backwards to the pinhole plane, it does not quite reveal a uniform circular pinhole. It is possible, the illumination function contains more than one coherent mode.

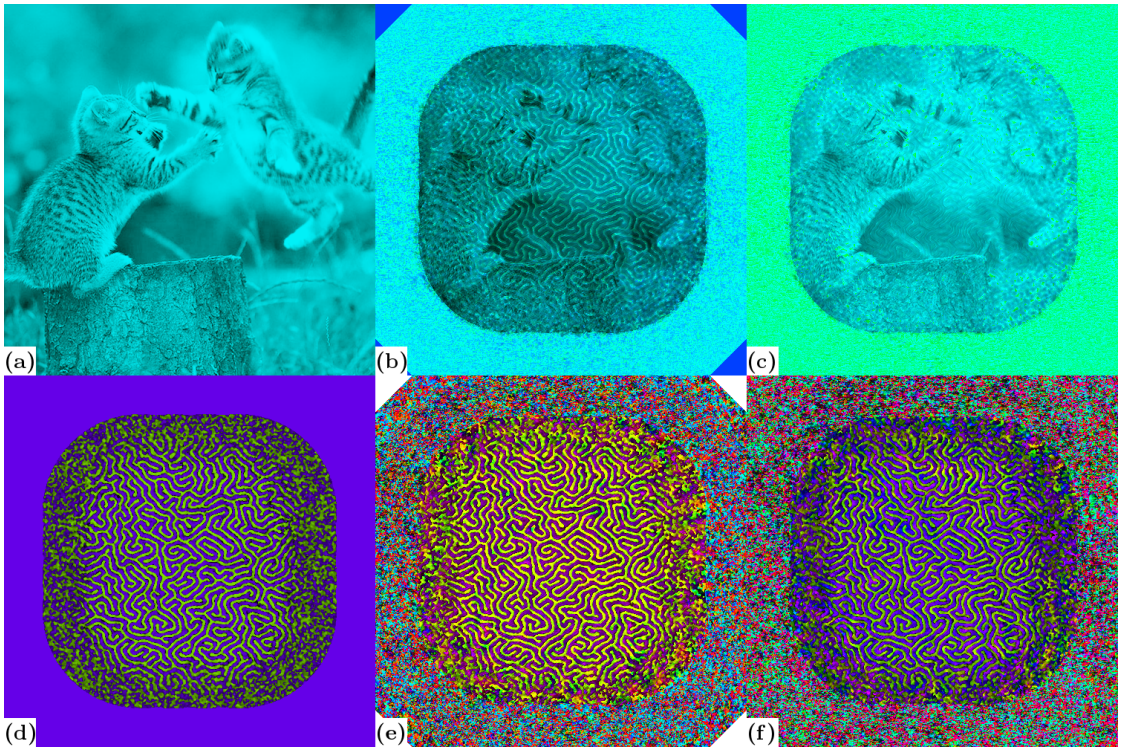


**Figure 5.5**: Reconstructions of simulated charge (a)-(c) and magnetic (d)-(f) contribution. The actual solution (a) and (d) are recovered up to constant phase shift, but mixed (b) and (e) when using no constraints on the solution. When the solution is periodically unmixed using the complex constraint, the final solution (c) and (f) are nearly separated completely.

## 5.7 Two mode: charge and magnetic

It is not necessary to use such special cases for PMA thin films, where the magnetic scattering can be subtracted and reconstructed on its own. Recall the scattering for linear polarization from magnetic thin film (eq. (5.5)) is the result of two views, namely from right hand polarization and left hand polarization components of the illumination function (eq. (5.4)). In fact, the two coherent modes from any elliptically polarized illumination is an ideal candidate for use with the multi-mode method (section 3.9).

As an example, consider a sample with charge and magnetic contribution (fig. 5.5), such that the object as seen by left-handed and right-handed circularly polarized photons can be written as, $O_{\pm}(\mathbf{r}_{\perp}) = e^{C(\mathbf{r}_{\perp})}e^{\pm M(\mathbf{r}_{\perp})}$. The charge

contribution, different from previous definition, is proportional to the object thickness, $z(\mathbf{r}_\perp)$, represented by two kittens (fig. 5.5 (a)). As before, the magnetic contribution is proportional to the projected magnetization, represented by the magnetization that is recovered from the uniform GdFe sample in section 5.5. The simultaneous reconstruction of these two modes will lead to an arbitrary mixing (section 3.10), when no addition constraints are used. In general, the reconstructed charge and magnetism are mixed and related to the actual by

$$2C'(\mathbf{r}_\perp) = 2C(\mathbf{r}_\perp) + \ln\left[\frac{(1+\epsilon e^{-2M(\mathbf{r}_\perp)})(1-\epsilon^* e^{2M(\mathbf{r}_\perp)})}{1+|\epsilon|^2}\right], \tag{5.12a}$$

$$2M'(\mathbf{r}_\perp) = 2M(\mathbf{r}_\perp) + \ln\left[\frac{1+\epsilon e^{-2M(\mathbf{r}_\perp)}}{1-\epsilon^* e^{2M(\mathbf{r}_\perp)}}\right]. \tag{5.12b}$$

The reconstructed charge (fig. 5.5 (b)) is contaminated with the magnetism. However, the reconstructed magnetism is recognizable. It is possible to separate the solution by minimizing an error related to physical constraints on the solution. As a possibility, the complex constraint [41] can be used, where the error is the variation in ratio between the real and imaginary parts of the charge and/or magnetism as a function of the mixing parameter. When this is used, the reconstructed charge (fig. 5.5 (c)) and magnetism (fig. 5.5 (f)) are nearly separated. An exact separation requires a stronger constraint or manual separation.

## 5.8 Two mode: GdFe with patterned Au

The Au:GdFe can also be reconstructed directly from the total scattering (fig. 5.3 (a)) using the two mode method. As in section 5.7, the reconstruction is unmixed using the complex constraint and an average of fifteen reconstructions is taken. The charge contribution (fig. 5.6 (a)) is almost entirely uniform. It's only variations are those from the magnetic contribution that have not been completely unmixed and low frequency modes that can arise in the recovered intensity behind the beamstop due to the periodic step taken in the ptychographic scan. It is expected that the Au charge structure is not recovered, as it's contribution to the scattering is very weak in comparison to the magnetic scattering on the resonant edge. Similarly, the magnetic contribution contains low frequency modes

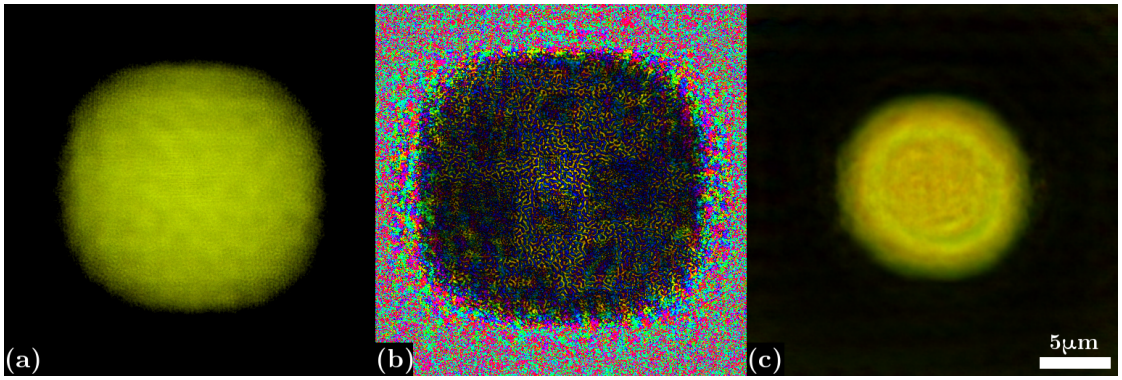


**Figure 5.6**: Au:GdFe reconstruction using the two mode method. (a) Recovered charge contribution, (b) recovered magnetic contribution, (c) recovered illumination function.

(fig. 5.3 (b)), however, the overall domains are almost identical to the magnetic reconstruction of section 5.6. The illumination function (fig. 5.3 (c)) is also very similar to the one recovered in section 5.6.

This shows that the two mode method is a viable technique for imaging the charge and magnetic structure of PMA thin films simultaneously using linear polarization. Thus, a much wider range of interesting samples can be images, such as pattern induced confinement and interaction between boundaries and layers.

# Chapter 6

# X-ray induced persistent photoconductivity in vanadium dioxide

## 6.1 Introduction

Metal oxides exhibit diverse ground states and phenomena including high-temperature superconductivity [107], colossal magnetoresistance [108], charge density waves [109], Verwey transitions [110], and metal-insulator transitions (MIT) [111]. Significant attention has been given to the deceptively simple MIT, which has to date been driven with temperature, electric field [112], pressure [113], chemical doping [114], ultrafast laser excitation [115], and ionizing radiation [116]. The MIT in $VO_2$ occurs above room temperature (340 K) with a simultaneous structural phase transition (SPT), changing from a semiconductor with a monoclinic lattice to a metal with a tetragonal lattice [111, 117, 118]. There is a variation of MIT temperatures between $VO_2$ grains, even for high quality samples [119]. Thus, metallic inclusions exist well below the bulk MIT temperature. The band bending at these metal-insulator interfaces can extend the lifetime of photogenerated electron-hole pairs, which contribute to conductivity [120].

Persistent photoconductivity (PPC) has been intensely studied in semi-

conductors [121, 122], superconductors [123], and metal oxides [116]. PPC is an increase in carrier concentration or mobility that is induced by electromagnetic radiation and remains for an extended period of time after illumination has ceased [124]. A long-lived photoinduced conversion to the metallic phase was previously observed in tungsten doped vanadium dioxide, but only below 50 K [125]. Additionally, a short-lived photoconductivity, decaying within tens of seconds, has been observed in vanadium oxide nano-devices [126, 127, 128]. However, long-lived photoconductivity has not been induced in pure $VO_2$ at room temperature until now. In addition, it was unclear if photoconductivity in $VO_2$ is coupled with the MIT and SPT. To better understand the driving mechanism of PPC in $VO_2$, we explored the relationship between crystal structure and PPC using localized x-ray radiation at room temperature. In this article, we show that photoillumination produced a large increase in conductance lasting for hours after illumination had ceased. Furthermore, we demonstrate that this dramatic change in conductance did not modify the metal-insulator transition temperature or change the crystal structure at the current resolution. Finally, to explain this effect we discuss and refute several possibilities, suggesting two well established models as candidates for PPC in $VO_2$.

## 6.2 Setup and sample

The vanadium dioxide ($VO_2$) thin film was prepared on an r-plane sapphire substrate by reactive RF magnetron sputtering. The target used in the deposition was a $V_2O_3$ pressed and sintered powder ceramic (1.5" diameter, >99.7%, ACI Alloys, Inc.). The sample was prepared in a high vacuum deposition system with a base pressure of $10^{-7}$ torr. A mixture of ultra high purity Ar and $O_2$ gases were used for sputtering. The total pressure during deposition was 4.0 mtorr, and the oxygen partial pressure was optimized to $3.4 \times 10^{-4}$ torr (8.5% of the total pressure). The substrate temperature was 600 °C and the RF magnetron power was 100 W. The film reported here is 80 nm and was deposited at a rate of 0.17 Å/s. Due to the substrate interaction, the thin film grows polycrystalline, with grains

randomly oriented in-plane, but with the (100) monoclinic direction out-of-plane.

The sample was cooled at a rate of 13°C/min in the same $Ar/O_2$ background gas of the deposition. On top of the $VO_2$ film, rectangular metallic electrodes were deposited with 10 µm separation and 7 µm width using electron-beam lithography. A set of leads, for electrical connections, were patterned on top of the small electrodes using photolithography. The leads and electrodes were made by sputtering 50 nm vanadium, which acts as an adhesion layer, and 100 nm of gold to assure that the electrode resistance is lower than that of the metallic $VO_2$.

This sample exhibited three-orders magnitude resistance change when going through the metal-insulator transition (MIT), reaching a high-temperature resistance of approximately 25 Ω. Below 325 K, the resistance followed Mott insulating behaviour with an activation energy of $(330 \pm 10)$ meV. With an expected band gap of 600 meV [129], this is a good indication that our sample was only weakly doped with impurities.

The sample was mounted on a stage with a heater able to reach 400 K and a Pt100 RTD to measure temperature immediately adjacent to the sample. The stage is mounted to a Newport 6-circle Kappa diffractometer. A Princeton Quad-RO CCD is used to measure the (200) x-ray diffraction peak in the low-temperature monoclinic phase and the (101) peak in the high-temperature tetragonal phase. Both of these reflections are near the substrate normal direction and thus accessible for all grains in the film. A Vortex-EX x-ray fluorescence detector is used to locate the $VO_2$ device regions between the gold contacts. These gold contacts are used to measure resistance across the device by applying a voltage (V) referenced to ground and measuring the current (I). To ensure that no significant distortion of the electronic density of states occurred, we applied a small 50 V/cm electric field for our measurements [130]. We approximate the device resistance as V/I from this two-terminal measurement.

Primary measurements were performed at Sector 2-ID-D insertion device (micro-diffraction) beamline of the Advanced Photon Source. X-rays were produced via an undulator tuned to 10.3 keV and monochromatized by a Si (111) double-Bragg crystal. A pinhole was used in series with a zone plate to select only

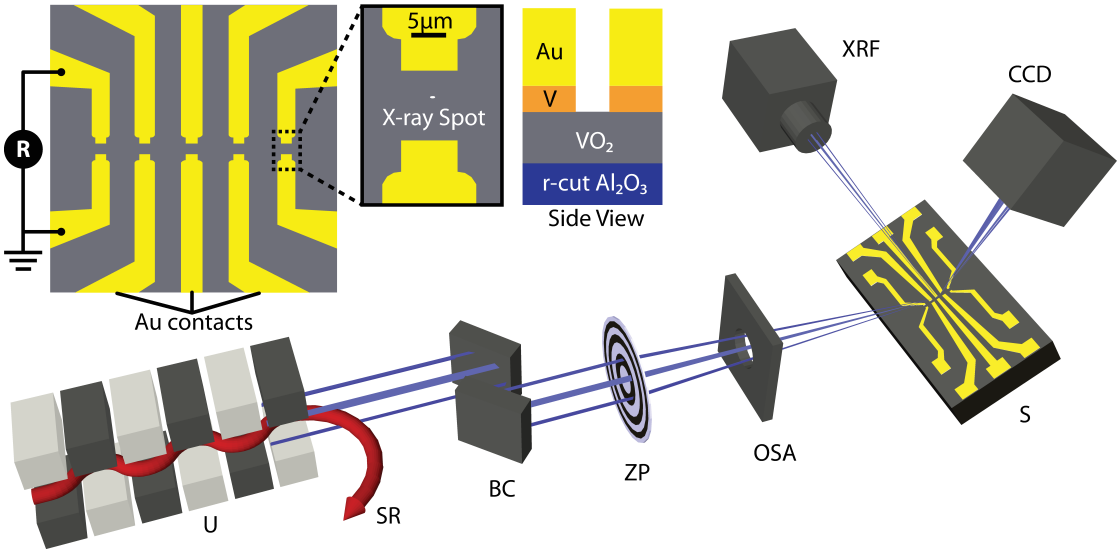


**Figure 6.1**: Top Left: Structure of $VO_2$ devices showing arrangement of gold contacts on $VO_2$ film and two-terminal probe to measure resistance. Bottom: Experimental setup at Sector 2-ID-D beamline of Advanced Photon Source. X-rays are generated by electrons from the Synchrotron Storage Ring (SR) in an Undulator (U), monochromatized by Si (111) double Bragg Crystal (BC), and focused by a Fresnel zone plate (ZP). The first-order is select by a 15 $\mu$m pinhole (OSA), giving a 250 nm by 950 nm beam spot on the sample (S). X-rays are measured via Fluorescence (XRF) detector and a charge coupled device (CCD).

the first order focus. The focusing and incident angle gives a 250 nm × 950 nm x-ray footprint on the sample that determines the horizontal and vertical spatial resolution, respectively. The total photon flux is approximately $10^9$ photons/second. All measurements were made in air at atmospheric pressure.

## 6.3 Results

We probed a $VO_2$ device at room temperature (300 K) using focused x-rays. The illumination induced a photoconductance, which we define here as the measured conductance minus the conductance before x-ray illumination. The observed increases in photoconductance correlate with x-ray illumination of the device (Figure 6.2). After the x-ray illumination ceased, the photoconductance gradually decreased and returned to zero within a week at room temperature. In addition, the x-ray exposure did not alter the MIT temperature. Heating the device through the MIT showed a sharp drop in resistance at the same temperature as before x-ray illumination (Fig. 6.3 (a)). This is in contrast to high-$T_c$ cuprates, where illumination induces photoconductivity in the semiconducting state and modifies the superconducting transition temperature [122].

In a separate experiment, we illuminated the same device with a 650 nm (1.9 eV) laser focused to 100 µm × 100 µm. We estimate the device region was irradiated with $10^{14}$ ph/s or 30 µW power, which is over three orders of magnitude more power compared to the total x-ray power absorbed into the $VO_2$ film. The laser did not elicit a conductance change, indicating that any deep level impurities within the 0.6 eV band gap are not the cause for PPC in $VO_2$ [129]. This is in contrast with usual photoconductance in semiconductors, where a donor-complex model is often used [121].

A change in conductance due to the MIT is directly associated with the SPT and results in a change of the lattice parameters, which shows up as a shift in the location of the Bragg diffraction peaks. We have mapped the structural phase of the device, define by the gold contact pads (Fig. 6.3(b)), with and without photoconductance (Fig. 6.3(1c) to (3c)). We present these maps as the difference in

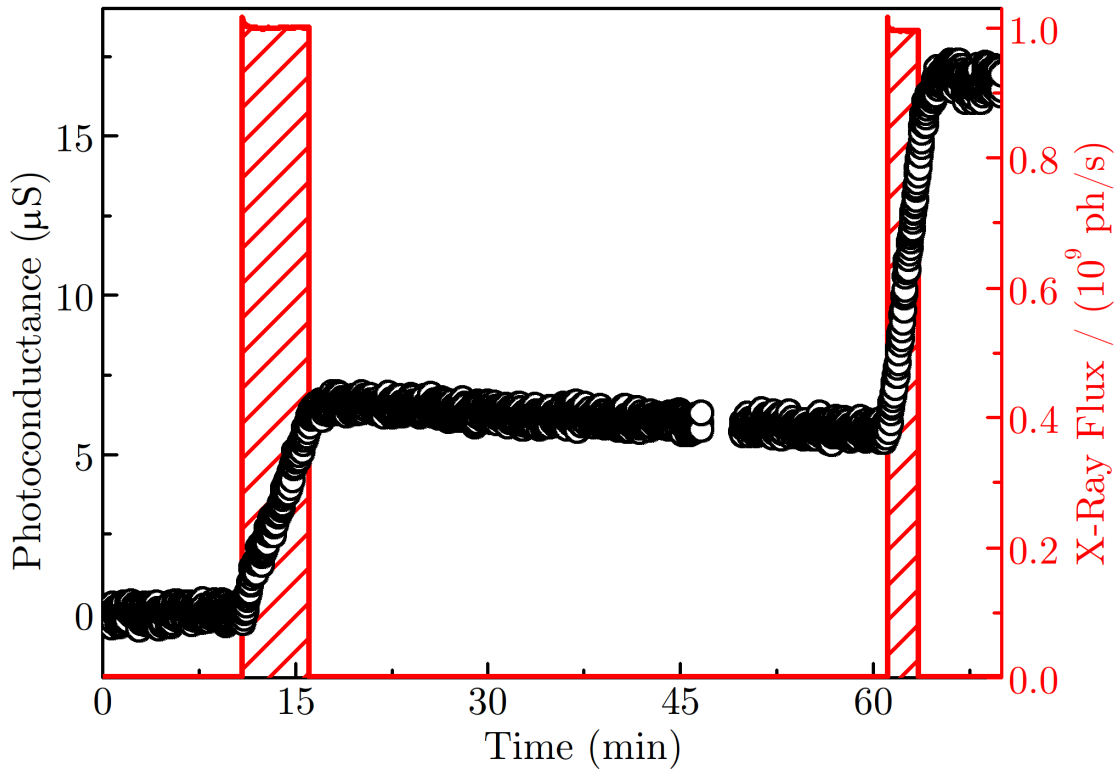


**Figure 6.2**: Photoconductance (black circles) of the $VO_2$ device at 300 K, showing rapid increase during x-ray illumination (dashed red region) as well as slow decrease after the x-ray illumination was turned off.

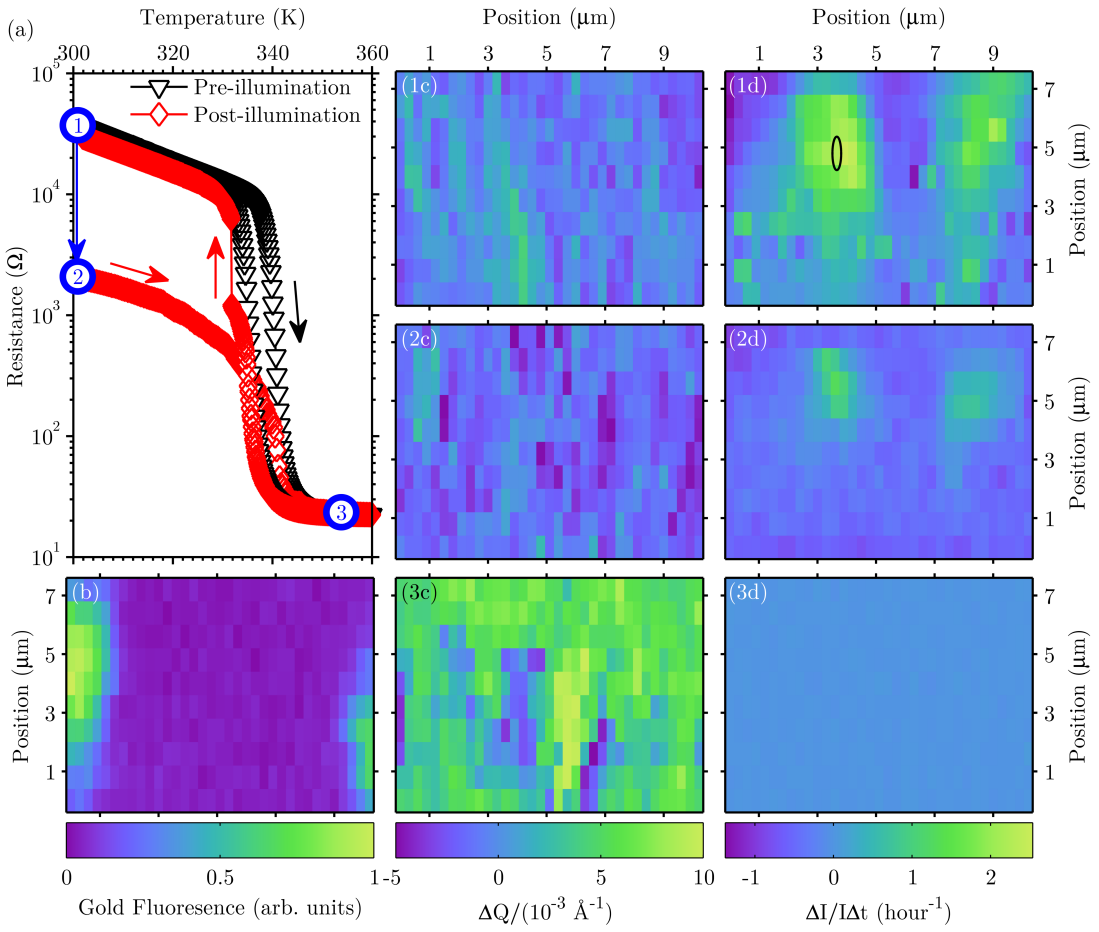


**Figure 6.3**: (a) The resistance is reduced by over one-order of magnitude at room temperature (point 1 to 2) by illuminating the device with x-rays at the indicated location in (1d) by the black ellipse. The resistance versus temperature hysteresis shows that the thermal component of the insulator-metal transition occurs at the same temperature for post-illumination (red diamonds) as no x-ray exposure (black down-pointing triangles). The original state is recovered by annealing the sample at 400 K and returning to room temperature. The device maps (b) to (d) are generated by scanning x-rays starting from the bottom-left corner proceeding in a series of horizontal lines. (b) Gold fluorescence intensity indicates the electrodes that define the device area. (c) Change in out-of-plane Bragg peak as compared to monoclinic phase and (d) normalized change in conductance induced by x-ray exposure for (1) 300 K and 40 kΩ resistance before significant x-ray exposure in the monoclinic phase with $\langle Q \rangle_M = 2.590\,\text{Å}^{-1}$ and $\langle \Delta I/I\Delta t \rangle_M = +0.3\,\text{h}^{-1}$; (2) 300 K and 2 kΩ resistance after x-ray exposure with $\langle Q \rangle_{PPC} = 2.589\,\text{Å}^{-1}$ and $\langle \Delta I/I\Delta t \rangle_{PPC} = -0.3\,\text{h}^{-1}$; (3) 354 K and 25 Ω resistance in the tetragonal phase with $\langle Q \rangle_R = 2.594\,\text{Å}^{-1}$ and $\langle \Delta I/I\Delta t \rangle_R = 0.0\,\text{h}^{-1}$.

the location of the measured Bragg peak and the mean Bragg peak of the low-temperature monoclinic phase, $\Delta Q = Q - \langle Q \rangle_M$. These maps show local variation due to strain of individual grains, common of thin films. At 300 K and 40 kΩ resistance, before significant x-ray exposure (Fig. 6.3(1c)), the out-of-plane Bragg peak was found in the monoclinic phase with $\langle Q \rangle_M = 2.590\,\text{Å}^{-1}$. For comparison, at 354 K and 25 Ω resistance (Fig. 6.3(3c)), the out-of-plane Bragg peak was found at $\langle Q \rangle_R = 2.594\,\text{Å}^{-1}$. This is the expected $4 \times 10^{-3}\,\text{Å}^{-1}$ shift between the monoclinic phase at 300 K and the tetragonal phase at 354 K [131]. Near the MIT, a coexistence of the high- and low-temperature phases is known to occur [132, 133, 119]. After approximately 45 minutes of x-ray exposure at the location indicated by the black ellipse in Fig. 6.3(1d), the room temperature resistance dropped from 40 kΩ to 2 kΩ (point 1 to 2 on Fig. 6.3(a)). However, the sample was not modified toward the high-temperature (tetragonal) structure, having a mean out-of-plane Bragg peak of $\langle Q \rangle_{PPC} = 2.589\,\text{Å}^{-1}$.

Although, a change in conductance can be induced by x-ray illumination of a single location and did not require any scanning of the device, the photoresponse varied across the device (Fig. 6.3(1d) to (3d)). By photoresponse we mean a change in conductance during a short eight second period of localized illumination. We scanned the device using continuous illumination. Thus, it is possible to observe a negative photoresponse due to relaxation of photoconductance induced at previously scanned locations. The relaxation is approximately $-1.3\,\text{h}^{-1}$, shown in Fig. 6.2, during no illumination, matching well to the minimum observed of $-1.4\,\text{h}^{-1}$ for some regions, suggesting there is no actual negative photoresponse but only decay of previously generated photoconductance. Initially, the photoresponse was very strong in two large regions of the device, with a maximum of $+2.5\,\text{h}^{-1}$ and mean of $+0.3\,\text{h}^{-1}$ (Fig. 6.3 (1d)). Although these variations in photoresponse to some extent agree with the variations in high-temperature structural phase, the correlation is weak. There is no statistically significant difference in the crystal structure for regions exhibiting strong and weak photoresponse. After significant illumination, the strong photoresponse regions shrank in size, now with maximum of $+1.3\,\text{h}^{-1}$ (Fig. 6.3 (2d)). Most of the region can no longer sustain

the immediate photoconductance giving a mean photoresponse of $-0.3\,\mathrm{h}^{-1}$. For comparison, at 354 K in the metallic state (25 Ω), the conductance is stable and no photoresponse is observed (Fig. 6.3 (3d)).

At 330 K, just below the MIT temperature, we observed a slow decay of photoconductance after x-ray illumination is stopped (Fig. 6.4). Given that the photoconductance decays continuously to zero, an accurate fit was made by using a stretched exponential of the form,

$$G_0 \exp\left[-(t/\tau)^{\beta}\right]. \tag{6.1}$$

This function is commonly used to describe relaxation toward equilibrium in a wide variety of systems including those exhibiting PPC due to random local-potential fluctuations [124, 134] and discrete random traps [135]. The stretched exponential fit agrees with the observed photoconductance decay over the entire range. We extract a time constant of $\tau = (54 \pm 1)\,\mathrm{h}$ and a stretching exponent of $\beta = 0.69 \pm 0.01$. This gives a mean relaxation time of $(69 \pm 1)\,\mathrm{h}$.

The PPC relaxation time was significantly reduced by thermal cycling the $VO_2$ well above the MIT temperature. After annealing the device at 400 K for 20 minutes without illumination, it recovered the original resistance upon cooling (red diamond curve of Fig. 6.3(a)).

## 6.4 Discussion

The persistent nature of the photoconductance is not consistent with a thermally induced MIT. The x-ray power used was 1.6 µW, only 1.5% of which is absorbed into the 80 nm thick sample, calculated from the attenuation coefficient and the illumination angle. The $Al_2O_3$ substrate has a much smaller attenuation coefficient and a much larger thermal conductivity compared to $VO_2$ and thus acts as a thermal sink. From the heat transport equation and known thermal properties of $VO_2$ at room temperature, we calculate that at equilibrium the x-ray heat loading of the entire device was less than 0.1 mK. This does not account for further losses due to atmosphere, which would further reduce this number. Since, the sample temperature is stabilized approximately 35 K below the MIT temperature,

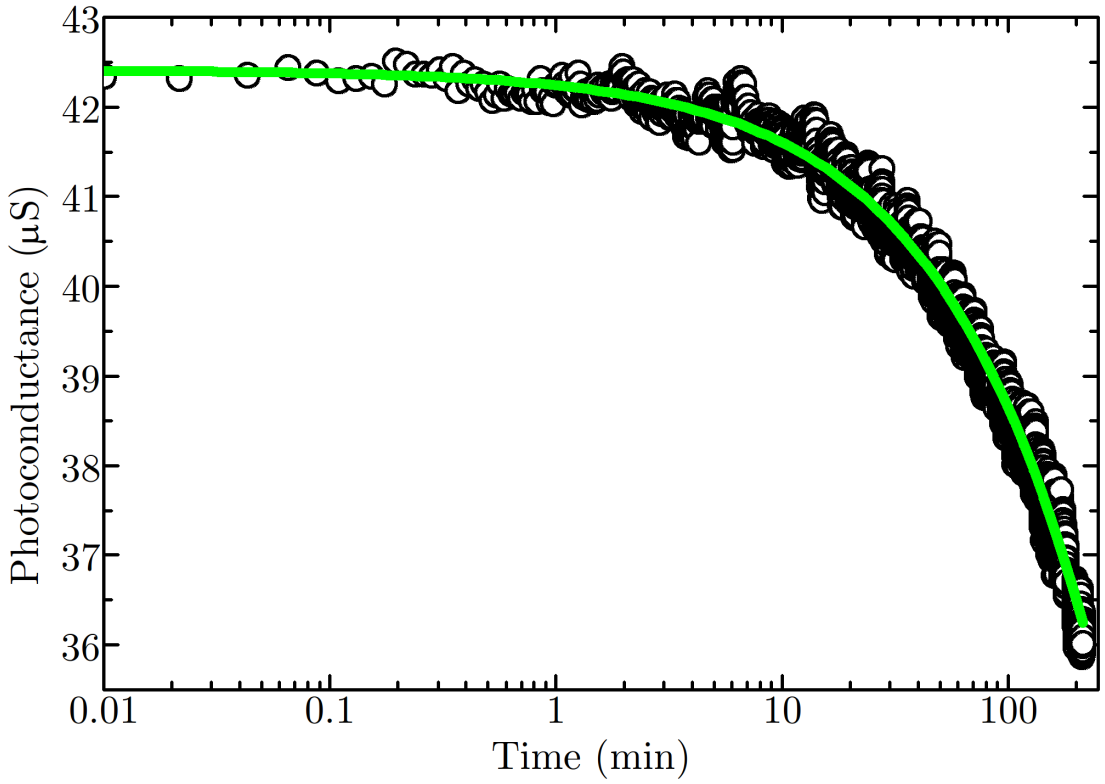


**Figure 6.4**: Decay of photoconductance at 330 K post-illumination. The green line is a fit using a stretched exponential with the additional information that the photoconductance eventually returns to zero. The mean relaxation time is 69 hours.

the x-ray power is insufficient to raise the temperature of the device to cause a significant change in the measured resistance. Since the x-ray beam was highly focused, a thermoelectric current could result from localized heating near the gold contacts that are used for electrical transport measurements. However, a positive thermoelectric current due to heating near one contact would mean a negative thermoelectric current at the opposite contact [136]. We did not see this asymmetric response during localized illumination across the device (Fig. 6.3 (1d) and (2d)).

A previous observation of x-ray induced conductance increase in tungsten doped $VO_2$ was due to the formation of metallic puddles that exhibit the high-temperature (tetragonal) crystal structure [125]. It is suggested that each ionizing photon causes the dissociation of many V-V dimers, effectively converting the insulating phase to metal. A conversion to the metallic phase via the above process is expected to nucleate near the illuminated volume and spread isotropically, possibly in a random-resistor network fashion due to variations in the sample. To account for the one-order magnitude decrease in resistance that we have observed, our $VO_2$ device would need to be at least 37% volume metal fraction. Since we have observed no appreciable shift in the Bragg diffraction peak towards the tetragonal structure post-illumination (Fig. 6.3 (2c)), the generation of metallic puddles cannot be the cause for PPC in our $VO_2$ device.

It is noteworthy, that a metallic surface or filaments could also lead to the observed increase in conductance. In this case, the metal fraction would be a minimum of 1.2% of the device volume, if they extend uniformly from one electrode to the other. The diffraction signal would then mostly be indistinguishable from the insulating phase. However, a metallic surface created by a change in vanadium oxidation state, similar to PPC in ZnO [137, 138], is not likely. To observe an increase in conductance, $VO_2$ would need to be reduced [139]. Since the beam is well localized, yet a large portion of the surface must participate to account for the photoconductance, a significant oxygen mobility would be required, which is only seen for layered or amorphous materials [140]. Therefore, if the observed PPC is associated with a structural transition, it must come in the form of a large number of narrow metallic filaments, since a single filament of the minimum

required 85 nm width would still be detected. For instance, it is possible that a change in conductance is primarily confined to grain boundaries or other extended defects, however at the current resolution this cannot be determined.

An estimated total of $10^{10}$ photons were absorbed into the $VO_2$ film when we observed a one-order magnitude decrease in resistance at room temperature (300 K). If one photocarrier is generated per photon, such carriers would need a mobility of $0.1\,\mathrm{cm}^2/(\mathrm{V\,s})$ to account for the resistance change. This is within the known range of electron mobility in the insulating phase for $VO_2$ [141] of $(0.1 \text{ to } 1)\,\mathrm{cm}^2/(\mathrm{V\,s})$. This indicates that an increase in carrier concentration is the cause for the change in conductance.

The long recombination time of photoinduced carriers is generally explained by phonon-assisted hopping or tunneling of potential barriers [142]. Using the simple Arrhenius model, the time for hopping of a potential barrier is given by,

$$t = t_0 \exp\left(\frac{E}{k_B T}\right), \tag{6.2}$$

where $t_0$ is the inverse of the electron-hole recombination attempt rate, $E$ is the activation energy (potential barrier), $k_B$ is the Boltzmann constant and $T$ is the temperature of the system. Since, systems exhibiting local-potential fluctuations do not strictly follow the expected temperature dependent decay time [126], we shall estimate the potential barrier by using the standard attempt rate of 1 THz induced by phonons [143]. We thus calculate the average effective activation energy as $(1.1 \pm 0.2)\,\mathrm{eV}$, where the error is given by using a three order magnitude deviation of the attempt rate (i.e. 1 GHz to 1 PHz). This is almost twice as large as the 0.6 eV $VO_2$ band gap [129]. Other oxides, such as ZnO, also show an activation energy of roughly 1 eV [137]. This is in contrast to the donor-complex model used for semiconductors, as the barrier is always less than the band gap. For example, both $Al_{0.3}Ga_{0.7}As$ and $Zn_{0.3}Cd_{0.7}Se$ have approximately 0.1 eV barriers with a direct band gap of 1.9 eV and 2.0 eV, respectively [144, 121, 134, 145, 146, 147]. The large energy barrier observed could be due to a number of things including $VO_x$ phase boundaries, where the conduction bands can change significantly or due to a much smaller variation in $VO_{2+\delta}$, but requiring a collective electron/hole hopping.

A number of models have been developed to describe persistent photocon-

ductivity in various materials. It is known that even high quality $VO_2$ thin films exhibit inhomogeneities, such as nonstoichiometry and grain boundaries, which are responsible for the microscopic phase coexistence far below the bulk MIT temperature [132, 133, 119]. Photogenerated electron-hole pairs can be separated due to band bending at these metal-insulator phase boundaries. The long recombination time is likely the result of random local-potential fluctuations and/or a random distribution of discrete recombination sites, due to these inhomogeneities [134, 135]. With discrete sites, the relaxation becomes stretched [148]. However, our observed value of $\beta = 0.69$ is slightly larger than the expected value of $\frac{3}{5}$ for 3-dimensional systems [149]. This increase is often observed near and above the MIT temperature where electron correlations are reduced and simple (Debye) exponential relaxation is recovered [150].

## 6.5 Conclusion

Although we have reported on only one $VO_2$ device, we have carefully measured and consistently found residual photoconduction in five samples, prepared by various growers from different laboratories. Focused x-ray radiation reversibly altered the device conductance without modifying the MIT transition temperature or high-temperature resistance. In addition, the structural transition was not induced for any sizable convex region as compared to the imaging resolution. Two distinct geometric possibilities exist to explain this. In the first case, a relatively weak additional conductance channel is created over a large portion of the device. This channel would be completely decoupled from the MIT and SPT. In the second case, illumination causes a stable transition to the metallic state along narrow filaments, likely along grain boundaries. These two cases could be distinguished by using local conductance measurements.

The mechanism for long-term stability of photoconductivity is still open for discussion. To further the understanding of PPC in $VO_2$, it should be confirmed that the photoconductivity is indeed an increase in carrier concentration. This could be done by obtaining the mobility of carriers from Hall measurements pre-

and post-illumination [151].

## 6.6 Acknowledgments

This work was supported by AFOSR FA9550-12-1-0381. Use of the Advanced Photon Source, an Office of Science User Facility operated for the U.S. Department of Energy (DOE) Office of Science by Argonne National Laboratory, was supported by the U.S. DOE under Contract No. DE-AC02-06CH11357. X-ray microscopy measurements are supported by U.S. Department of Energy, Office of Science, Office of Basic Energy Sciences, under Contract DE-SC0001805.

Chapter 6, in large part, is a reprint of the material as it appears in S. H. Dietze, M. J. Marsh, Siming Wang, J.-G. Ramírez, Z.-H. Cai, J. R. Mohanty, Ivan K. Schuller, and O. G. Shpyrko. "X-ray-induced persistent photoconductivity in vanadium dioxide." *Phys. Rev. B* **90**, 165109 (2014) [1]. The dissertation author was the primary investigator and author of this paper.

# Bibliography


[1] S. H. Dietze, M. J. Marsh, S. Wang, J.-G. Ramírez, Z.-H. Cai, J. R. Mohanty, I. K. Schuller, and O. G. Shpyrko *Phys. Rev. B*, vol. 90, p. 165109, Oct 2014.

[2] J. D. Jackson, *Classical Electrodynamics*. Hoboken, NJ: John Wiley and Sons, 3rd ed., 1999.

[3] G. R. Fowles, *Introduction to Modern Optics*. Dover, New York, 1989.

[4] J. W. Goodman, *Introduction to Fourier Optics*. McGraw-Hill, 2nd ed., 1996.

[5] M. Born, "Quantenmechanik der stovorgnge," *Zeitschrift fr Physik*, vol. 38, no. 11-12, pp. 803–827, 1926.

[6] C. Huygens, *Trait de la Lumiere*. Pieter van der Aa, 1690.

[7] M. A. Fresnel, "Memoire sur la diffraction de la lumiere," *Annales de chimie et de physique*, vol. 1, no. 1, p. 239, 1816.

[8] G. Kirchhoff, "Zur theorie der lichtstrahlen," *Annalen der Physik*, vol. 254, no. 4, pp. 663–695, 1883.

[9] A. Sommerfeld, *Lectures on Theoretical Physics: Optics*, vol. 4. Academic Press, 1964.

[10] D. Mendlovic, Z. Zalevsky, and N. Konforti, "Computation considerations and fast algorithms for calculating the diffraction integral," *Journal of Modern Optics*, vol. 44, no. 2, pp. 407–414, 1997.

[11] D. Mas, J. Garcia, C. Ferreira, L. M. Bernardo, and F. Marinho, "Fast algorithms for free-space diffraction patterns calculation," *Optics Communications*, vol. 164, no. 46, pp. 233 – 245, 1999.

[12] F. Shen and A. Wang, "Fast-fourier-transform based numerical integration method for the rayleigh-sommerfeld diffraction formula," *Appl. Opt.*, vol. 45, pp. 1102–1110, Feb 2006.

[13] J. García, D. Mas, and R. G. Dorsch, "Fractional-fourier-transform calculation through the fast-fourier-transform algorithm," *Appl. Opt.*, vol. 35, pp. 7013–7018, Dec 1996.

[14] J. J. Sakurai, *Modern Quantum Mechanics*. Addison-Wesley, revised ed., 1994.

[15] J. D. Jackson, *Classical Electrodynamics*. John Wiley and Sons, 3rd ed., 1998.

[16] R. D. L. KRONIG, "On the theory of dispersion of x-rays," *J. Opt. Soc. Am.*, vol. 12, pp. 547–556, Jun 1926.

[17] N. W. Ashcroft and N. D. Mermin, *Solid State Physics*. Thomson Learning, 1976.

[18] J. W. Goodman, *Statistical Optics*. John Wiley and Sons, wiley classics library ed., 2000.

[19] P. van Cittert, "Die wahrscheinliche schwingungsverteilung in einer von einer lichtquelle direkt oder mittels einer linse beleuchteten ebene," *Physica*, vol. 1, no. 16, pp. 201–210, 1934.

[20] F. Zernike, "The concept of degree of coherence and its application to optical problems," *Physica*, vol. 5, no. 8, pp. 785–795, 1938.

[21] I. A. Vartanyants and A. Singer, "Coherence properties of hard x-ray synchrotron sources and x-ray free-electron lasers," *New Journal of Physics*, vol. 12, no. 3, p. 035004, 2010.

[22] O. Klein and Y. Nishina, "ber die streuung von strahlung durch freie elektronen nach der neuen relativistischen quantendynamik von dirac," *Zeitschrift fr Physik*, vol. 52, no. 11-12, pp. 853–868, 1929.

[23] J. H. Hubbell, W. J. Veigele, E. A. Briggs, R. T. Brown, D. T. Cromer, and R. J. Howerton, "Atomic form factors, incoherent scattering functions, and photon scattering cross sections," *Journal of Physical and Chemical Reference Data*, vol. 4, no. 3, pp. 471–538, 1975.

[24] J. Als-Nielsen and D. McMorrow, *Elements of Modern X-ray Physics*. John Wiley and Sons, 2nd ed., 2011.

[25] S. K. Sinha, "Theory of inelastic x-ray scattering from condensed matter," *Journal of Physics: Condensed Matter*, vol. 13, no. 34, p. 7511, 2001.

[26] Z. Wu, H. Hong, R. Aburano, P. Zschack, P. Jemian, J. Tischler, H. Chen, D.-A. Luh, and T.-C. Chiang, "Pattern of x-ray scattering by thermal phonons in si," *Phys. Rev. B*, vol. 59, pp. 3283–3286, Feb 1999.

[27] M. Holt, Z. Wu, H. Hong, P. Zschack, P. Jemian, J. Tischler, H. Chen, and T.-C. Chiang, "Determination of phonon dispersions from x-ray transmission scattering: The example of silicon," *Phys. Rev. Lett.*, vol. 83, pp. 3317–3319, Oct 1999.

[28] C. E. Shannon, "Communication in the presence of noise," *Proceedings of the IRE*, vol. 37, no. 1, pp. 10–21, 1949. Rpt. in Proceedings of the IEEE 86, 447 (1998).

[29] H. Nyquist, "Certain topics in telegraph transmission theory," *American Institute of Electrical Engineers, Transactions of*, vol. 47, no. 2, pp. 617–644, 1928. Rpt. in Proceedings of the IEEE 90, 280 (2002).

[30] N. Wiener, "Generalized harmonic analysis," *Acta Mathematica*, vol. 55, no. 1, pp. 117–258, 1930.

[31] A. Khintchine, "Korrelationstheorie der stationren stochastischen prozesse," *Mathematische Annalen*, vol. 109, no. 1, pp. 604–615, 1934.

[32] R. Bates, "Fourier phase problems are uniquely solvable in more than one dimension. i: Underlying theory," *Optik*, vol. 61, no. 3, pp. 247–262, 1982.

[33] D. Sayre, "The squaring method: a new method for phase determination," *Acta Crystallographica*, vol. 5, pp. 60–65, Jan 1952.

[34] J. Miao, D. Sayre, and H. N. Chapman, "Phase retrieval from the magnitude of the fourier transforms of nonperiodic objects," *J. Opt. Soc. Am. A*, vol. 15, pp. 1662–1669, Jun 1998.

[35] Y. M. Bruck and L. G. Sodin, "On the ambiguity of the image reconstruction problem," *Optics Communications*, vol. 30, no. 3, pp. 304–308, 1979.

[36] R. Bates, "Uniqueness of solutions to two-dimensional fourier phase problems for localized and positive images," *Computer Vision, Graphics, and Image Processing*, vol. 25, no. 2, pp. 205–217, 1984.

[37] A. M. J. Huiser and P. van Toorn, "Ambiguity of the phase-reconstruction problem," *Opt. Lett.*, vol. 5, pp. 499–501, Nov 1980.

[38] T. R. Crimmins, J. R. Fienup, and B. J. Thelen, "Improved bounds on object support from autocorrelation support and application to phase retrieval," *J. Opt. Soc. Am. A*, vol. 7, pp. 3–13, Jan 1990.

[39] J. R. Fienup, B. J. Thelen, M. F. Reiley, and R. G. Paxman, "3d locator sets of opaque objects for phase retrieval," vol. 3170, pp. 88–96, 1997.

[40] S. Marchesini, H. He, H. N. Chapman, S. P. Hau-Riege, A. Noy, M. R. Howells, U. Weierstall, and J. C. H. Spence, "X-ray image reconstruction from a diffraction pattern alone," *Phys. Rev. B*, vol. 68, p. 140101, Oct 2003.

[41] J. N. Clark, C. T. Putkunz, M. A. Pfeifer, A. G. Peele, G. J. Williams, B. Chen, K. A. Nugent, C. Hall, W. Fullagar, S. Kim, and I. McNulty, "Use of a complex constraint in coherent diffractive imaging," *Opt. Express*, vol. 18, pp. 1981–1993, Feb 2010.

[42] J. R. Fienup, "Phase retrieval algorithms: a comparison," *Appl. Opt.*, vol. 21, pp. 2758–2769, Aug 1982.

[43] V. Elser, "Phase retrieval by iterated projections," *J. Opt. Soc. Am. A*, vol. 20, pp. 40–55, Jan 2003.

[44] J. M. Rodenburg and H. M. L. Faulkner, "A phase retrieval algorithm for shifting illumination," *Applied Physics Letters*, vol. 85, no. 20, pp. 4795–4797, 2004.

[45] P. Thibault, M. Dierolf, A. Menzel, O. Bunk, C. David, and F. Pfeiffer, "High-resolution scanning x-ray diffraction microscopy," *Science*, vol. 321, no. 5887, pp. 379–382, 2008.

[46] A. M. Maiden and J. M. Rodenburg, "An improved ptychographical phase retrieval algorithm for diffractive imaging," *Ultramicroscopy*, vol. 109, no. 10, pp. 1256 – 1262, 2009.

[47] P. Thibault, V. Elser, C. Jacobsen, D. Shapiro, and D. Sayre, "Reconstruction of a yeast cell from X-ray diffraction data," *Acta Crystallographica Section A*, vol. 62, pp. 248–261, Jul 2006.

[48] I. Christov, "Propagation of partially coherent light pulses," *Optica Acta: International Journal of Optics*, vol. 33, no. 1, pp. 63–72, 1986.

[49] L.-g. Wang, Q. Lin, H. Chen, and S.-y. Zhu, "Propagation of partially coherent pulsed beams in the spatiotemporal domain," *Phys. Rev. E*, vol. 67, p. 056613, May 2003.

[50] H. Lajunen, J. Tervo, and P. Vahimaa, "Overall coherence and coherent-mode expansion of spectrally partially coherent plane-wave pulses," *J. Opt. Soc. Am. A*, vol. 21, pp. 2117–2123, Nov 2004.

[51] H. Lajunen, J. Tervo, and P. Vahimaa, "Theory of spatially and spectrally partially coherent pulses," *J. Opt. Soc. Am. A*, vol. 22, pp. 1536–1545, Aug 2005.

[52] P. Thibault and A. Menzel, "Reconstructing state mixtures from diffraction measurements," *Nature*, vol. 494, no. 7435, pp. 68–71, 2013.

[53] W. L. Bragg, "The structure of some crystals as indicated by their diffraction of x-rays," *Proceedings of the Royal Society of London A: Mathematical, Physical and Engineering Sciences*, vol. 89, no. 610, pp. 248–277, 1913.

[54] G. W. Stinton and J. S. O. Evans, "Parametric rietveld refinement," *Journal of Applied Crystallography*, vol. 40, no. 1, pp. 87–95, 2007.

[55] A. M. T. Bell, C. M. B. Henderson, R. F. Wendlandt, and W. J. Harrison, "Rietveld refinement of sr(5)(aso(4))(3)cl from high-resolution synchrotron data," *Journal of Applied Crystallography*, vol. 65, no. 3, pp. 16–17, 2009.

[56] J. D. Watson and F. H. C. Crick, "Molecular structure of nucleic acids: A structure for deoxyribose nucleic acid," *Nature*, vol. 171, no. 4356, pp. 737–738, 1953.

[57] D. Crowfoot, C. W. Bunn, B. W. Rogers-Low, and A. Turner-Jones, "X-ray crystallographic investigation of the structure of penicillin," in *Chemistry of Penicillin* (H. T. Clarke, J. R. Johnson, and R. Robinson, eds.), pp. 310–367, Princeton University Press, 1949.

[58] A. S. Foster, C. Barth, A. L. Shluger, and M. Reichling, "Unambiguous interpretation of atomically resolved force microscopy images of an insulator," *Phys. Rev. Lett.*, vol. 86, pp. 2373–2376, Mar 2001.

[59] R. Schweinfest, S. Köstlmeier, F. Ernst, C. Elsäser, T. Wagner, and M. W. Finnis, "Atomistic and electronic structure of al/mgal2o4 and ag/mgal2o4 interfaces," *Philosophical Magazine A*, vol. 81, no. 4, pp. 927–955, 2001.

[60] D. Weiß, G. Schneider, B. Niemann, P. Guttmann, D. Rudolph, and G. Schmahl, "Computed tomography of cryogenic biological specimens based on x-ray microscopic images," *Ultramicroscopy*, vol. 84, no. 34, pp. 185–197, 2000.

[61] G. A. Johansson, T. Tyliszczak, G. E. Mitchell, M. H. Keefe, and A. P. Hitchcock, "Three-dimensional chemical mapping by scanning transmission x-ray spectromicroscopy," *Journal of Synchrotron Radiation*, vol. 14, pp. 395–402, Sep 2007.

[62] P. J. Withers, "X-ray nanotomography," *Materials Today*, vol. 10, no. 12, pp. 26 – 34, 2007.

[63] J. R. Fienup, "Iterative method applied to image reconstruction and to computer-generated holograms," *Optical Engineering*, vol. 19, no. 3, pp. 193297–193297, 1980.

[64] M. C. Newton, S. J. Leake, R. Harder, and I. K. Robinson, "Three-dimensional imaging of strain in a single zno nanorod," *Nature Mater*, vol. 9, no. 2, pp. 120–124, 2010.

[65] A. Ulvestad, H. M. Cho, R. Harder, J. W. Kim, S. H. Dietze, E. Fohtung, Y. S. Meng, and O. G. Shpyrko, "Nanoscale strain mapping in battery nanostructures," *Applied Physics Letters*, vol. 104, no. 7, pp. 1–5, 2014.

[66] J. W. Kim, S. Manna, S. H. Dietze, A. Ulvestad, R. Harder, E. Fohtung, E. E. Fullerton, and O. G. Shpyrko, "Curvature-induced and thermal strain in polyhedral gold nanocrystals," *Applied Physics Letters*, vol. 105, no. 17, pp. 1–5, 2014.

[67] J. Miao, C.-C. Chen, C. Song, Y. Nishino, Y. Kohmura, T. Ishikawa, D. Ramunno-Johnson, T.-K. Lee, and S. H. Risbud, "Three-dimensional GaN-$ga_2o_3$ core shell structure revealed by x-ray diffraction microscopy," *Phys. Rev. Lett.*, vol. 97, p. 215503, Nov 2006.

[68] H. N. Chapman, A. Barty, S. Marchesini, A. Noy, S. P. Hau-Riege, C. Cui, M. R. Howells, R. Rosen, H. He, J. C. H. Spence, U. Weierstall, T. Beetz, C. Jacobsen, and D. Shapiro, "High-resolution ab initio three-dimensional x-ray diffraction microscopy," *J. Opt. Soc. Am. A*, vol. 23, pp. 1179–1200, May 2006.

[69] A. Tripathi, J. Mohanty, S. H. Dietze, O. G. Shpyrko, E. Shipton, E. E. Fullerton, S. S. Kim, and I. McNulty, "Dichroic coherent diffractive imaging," *Proceedings of the National Academy of Sciences*, vol. 20, no. 33, pp. 13393–13398, 2011.

[70] Q. Shen, I. Bazarov, and P. Thibault, "Diffractive imaging of nonperiodic materials with future coherent X-ray sources," *Journal of Synchrotron Radiation*, vol. 11, pp. 432–438, Sep 2004.

[71] D. Starodub, P. Rez, G. Hembree, M. Howells, D. Shapiro, H. N. Chapman, P. Fromme, K. Schmidt, U. Weierstall, R. B. Doak, and J. C. H. Spence, "Dose, exposure time and resolution in serial x-ray crystallography," *Journal of Synchrotron Radiation*, vol. 15, no. 1, pp. 62–73, 2008.

[72] M. Howells, T. Beetz, H. Chapman, C. Cui, J. Holton, C. Jacobsen, J. Kirz, E. Lima, S. Marchesini, H. Miao, D. Sayre, D. Shapiro, J. Spence, and D. Starodub, "An assessment of the resolution limitation due to radiation-damage in x-ray diffraction microscopy," *Journal of Electron Spectroscopy and Related Phenomena*, vol. 170, no. 13, pp. 4–12, 2009.

[73] A. E. Burgess, "The rose model, revisited," *J. Opt. Soc. Am. A*, vol. 16, pp. 633–646, Mar 1999.

[74] R. Hegerl and W. Hoppe, "Influence of electron noise on three-dimensional image reconstruction," *Zeitschrift fur Naturforschung A*, vol. 31, no. 12, pp. 1717–1721, 1976.

[75] B. F. McEwen, K. H. Downing, and R. M. Glaeser, "The relevance of dose-fractionation in tomography of radiation-sensitive specimens," *Ultramicroscopy*, vol. 60, no. 3, pp. 357 – 373, 1995.

[76] Y. Takahashi, Y. Nishino, R. Tsutsumi, H. Kubo, H. Furukawa, H. Mimura, S. Matsuyama, N. Zettsu, E. Matsubara, T. Ishikawa, and K. Yamauchi, "High-resolution diffraction microscopy using the plane-wave field of a nearly diffraction limited focused x-ray beam," *Phys. Rev. B*, vol. 80, p. 054103, Aug 2009.

[77] E. R. Jette and F. Foote, "Precision determination of lattice constants," *The Journal of Chemical Physics*, vol. 3, no. 10, pp. 605–616, 1935.

[78] C.-Y. Lee, Z. H. Stachurski, and T. R. Welberry, "The geometry, topology and structure of amorphous solids," *Acta Materialia*, vol. 58, no. 2, pp. 615 – 625, 2010.

[79] D. Waasmaier and A. Kirfel, "New analytical scattering-factor functions for free atoms and ions," *Acta Crystallographica Section A*, vol. 51, pp. 416–431, May 1995.

[80] L.-M. Peng, G. Ren, S. L. Dudarev, and M. J. Whelan, "Debye–Waller Factors and Absorptive Scattering Factors of Elemental Crystals," *Acta Crystallographica Section A*, vol. 52, pp. 456–470, May 1996.

[81] V. Rasche, R. Proksa, R. Sinkus, P. Börnert, and H. Eggers, "Resampling of data between arbitrary grids using convolution interpolation," *IEEE Transactions on Medical Imaging*, vol. 18, pp. 385–392, May 1999.

[82] A. Averbuch, R. Coifman, D. Donoho, M. Elad, and M. Israeli, "Fast and accurate polar fourier transform," *Applied and Computational Harmonic Analysis*, vol. 21, no. 2, pp. 145–167, 2006.

[83] M. Fenn, S. Kunis, and D. Potts, "On the computation of the polar {FFT}," *Applied and Computational Harmonic Analysis*, vol. 22, no. 2, pp. 257–263, 2007.

[84] J. R. Fienup and A. M. Kowalczyk, "Phase retrieval for a complex-valued object by using a low-resolution image," *J. Opt. Soc. Am. A*, vol. 7, pp. 450–458, Mar 1990.

[85] M. Guizar-Sicairos, S. T. Thurman, and J. R. Fienup, "Efficient subpixel image registration algorithms," *Opt. Lett.*, vol. 33, pp. 156–158, Jan 2008.

[86] D. H. Bilderback, J. D. Brock, D. S. Dale, K. D. Finkelstein, M. A. Pfeifer, and S. M. Gruner, "Energy recovery linac (erl) coherent hard x-ray sources," *Nature Photonics*, vol. 12, pp. 1–27, March 2010.

[87] M. Eriksson, L.-J. Lindgren, M. Sjstrm, E. Walln, L. Rivkin, and A. Streun, "Some small-emittance light-source lattices with multi-bend achromats," *Nuclear Instruments and Methods in Physics Research Section A: Accelerators, Spectrometers, Detectors and Associated Equipment*, vol. 587, no. 2–3, pp. 221 – 226, 2008.

[88] B. Abbey, L. W. Whitehead, H. M. Quiney, D. J. Vine, G. A. Cadenazzi, C. A. Henderson, K. A. Nugent, E. Balaur, C. T. Putkunz, A. G. Peele, W. J., and I. McNulty, "Lensless imaging using broadband x-ray sources," *Nature Photonics*, vol. 5, pp. 420–424, July 2011.

[89] P. Shirage, K. Kihou, C. Lee, H. Kito, H. Eisaki, and A. Iyo, "Discovery of the $ca_4al_2o_6fe_2pn_2$ "al-42622(pn)" and $ca_3al_2o_5fe_2pn_2$ "al-32522(pn)" (pn=as, p) superconductors," *Physica C: Superconductivity*, vol. 484, no. 0, pp. 12 – 15, 2013. Proceedings of the 24th International Symposium on Superconductivity (ISS2011).

[90] R. Neutze, R. Wouts, D. van der Spoel, E. Weckert, and J. Hajdu, "Potential for biomolecular imaging with femtosecond x-ray pulses," *Nature*, vol. 406, pp. 752–757, Aug 2000.

[91] W. Peterson, T. Birdsall, and W. Fox, "The theory of signal detectability," *Information Theory, Transactions of the IRE Professional Group on*, vol. 4, pp. 171–212, September 1954.

[92] A. Rose, "The sensitivity performance of the human eye on an absolute scale," *J. Opt. Soc. Am.*, vol. 38, pp. 196–208, Feb 1948.

[93] R. Sbiaa, H. Meng, and S. N. Piramanayagam, "Materials with perpendicular magnetic anisotropy for magnetic random access memory," *physica status solidi (RRL) Rapid Research Letters*, vol. 5, no. 12, pp. 413–419, 2011.

[94] D. Bedau, H. Liu, J.-J. Bouzaglou, A. D. Kent, J. Z. Sun, J. A. Katine, E. E. Fullerton, and S. Mangin, "Ultrafast spin-transfer switching in spin valve nanopillars with perpendicular anisotropy," *Applied Physics Letters*, vol. 96, no. 2, p. 022514, 2010.

[95] C. Kittel, "Physical theory of ferromagnetic domains," *Rev. Mod. Phys.*, vol. 21, pp. 541–583, Oct 1949.

[96] Y. Kawada, M. Onose, R. Tojo, T. Komine, and R. Sugita, "Magnetic domain structure in thin copt perpendicular magnetic anisotropy films," *EPJ Web of Conferences*, vol. 40, p. 07002, 2013.

[97] O. Hellwig, A. Berger, J. B. Kortright, and E. E. Fullerton, "Domain structure and magnetization reversal of antiferromagnetically coupled perpendicular anisotropy films," *Journal of Magnetism and Magnetic Materials*, vol. 319, no. 12, pp. 13–55, 2007.

[98] J. C. Lang, D. R. Lee, D. Haskel, and G. Srajer, "Imaging spiral magnetic domains in ho metal using circularly polarized bragg diffraction," *Journal of Applied Physics*, vol. 95, no. 11, pp. 6537–6539, 2004.

[99] J. P. Hannon, G. T. Trammell, M. Blume, and D. Gibbs, "X-ray resonance exchange scattering," *Phys. Rev. Lett.*, vol. 61, pp. 1245–1248, Sep 1988.

[100] M. Seul and D. Andelman, "Domain shapes and patterns: The phenomenology of modulated phases," *Science*, vol. 267, no. 5197, pp. 476–483, 1995.

[101] C. Kooy and U. Enz, "Experimental and theoretical study of the domain configuration in thin layers of $BaFe_{12}O_{19}$," *Philips Res. Repts.*, vol. 15, pp. 7–29, 1960.

[102] M. Seul and R. Wolfe, "Evolution of disorder in magnetic stripe domains. i. transverse instabilities and disclination unbinding in lamellar patterns," *Phys. Rev. A*, vol. 46, pp. 7519–7533, Dec 1992.

[103] M. Seul and R. Wolfe, "Evolution of disorder in magnetic stripe domains. ii. hairpins and labyrinth patterns versus branches and comb patterns formed by growing minority component," *Phys. Rev. A*, vol. 46, pp. 7534–7547, Dec 1992.

[104] M. Seul and R. Wolfe, "Evolution of disorder in two-dimensional stripe patterns: "smectic" instabilities and disclination unbinding," *Phys. Rev. Lett.*, vol. 68, pp. 2460–2463, Apr 1992.

[105] G. L. Nealon, B. Donnio, R. Greget, J.-P. Kappler, E. Terazzi, and J.-L. Gallani, "Magnetism in gold nanoparticles," *Nanoscale*, vol. 4, pp. 5244–5258, 2012.

[106] F. Michael, C. Gonzalez, V. Mujica, M. Marquez, and M. A. Ratner, "Size dependence of ferromagnetism in gold nanoparticles: Mean field results," *Phys. Rev. B*, vol. 76, p. 224409, Dec 2007.

[107] M. K. Wu, J. R. Ashburn, C. J. Torng, P. H. Hor, R. L. Meng, L. Gao, Z. J. Huang, Y. Q. Wang, and C. W. Chu, "Superconductivity at 93 k in a new mixed-phase y-ba-cu-o compound system at ambient pressure," *Phys. Rev. Lett.*, vol. 58, pp. 908–910, Mar 1987.

[108] A. J. Millis, "Lattice effects in magnetoresistive manganese perovskites," *Nature*, vol. 392, pp. 147–150, Mar 1998.

[109] S. Cox, J. Singleton, R. D. McDonald, A. Migliori, and P. B. Littlewood, "Sliding charge-density wave in manganites," *Nature*, vol. 7, pp. 25–30, Jan 2008.

[110] J. P. Attfield, A. M. T. Bell, L. M. Rodriguez-Martinez, J. M. Greneche, R. J. Cernik, J. F. Clarke, and D. A. Perkins, "Electrostatically driven charge-ordering in fe$_2$obo$_3$," *Nature*, vol. 396, pp. 655–658, May 1998.

[111] F. J. Morin, "Oxides which show a metal-to-insulator transition at the neel temperature," *Phys. Rev. Lett.*, vol. 3, pp. 34–36, Jul 1959.

[112] H.-T. Kim, B.-G. Chae, D.-H. Youn, G. Kim, K.-Y. Kang, S.-J. Lee, K. Kim, and Y.-S. Lim, "Raman study of electric-field-induced first-order metal-insulator transition in vo$_2$-based devices," *Appl. Phys. Lett.*, vol. 86, no. 24, p. 242101, 2005.

[113] E. Arcangeletti, L. Baldassarre, D. Di Castro, S. Lupi, L. Malavasi, C. Marini, A. Perucchi, and P. Postorino, "Evidence of a pressure-induced metallization process in monoclinic vo$_2$," *Phys. Rev. Lett.*, vol. 98, p. 196406, May 2007.

[114] W. Burkhardt, T. Christmann, S. Franke, W. Kriegseis, D. Meister, B. Meyer, W. Niessner, D. Schalch, and A. Scharmann, "Tungsten and fluorine co-doping of {VO2} films," *Thin Solid Films*, vol. 402, no. 1, pp. 226–231, 2002.

[115] A. Cavalleri, C. Tóth, C. W. Siders, J. A. Squier, F. Ráksi, P. Forget, and J. C. Kieffer, "Femtosecond structural dynamics in vo$_2$ during an ultrafast solid-solid phase transition," *Phys. Rev. Lett.*, vol. 87, p. 237401, Nov 2001.

[116] V. Kiryukhin, D. Casa, J. P. Hill, B. Keimer, A. Vigliante, Y. Tomioka, and Y. Tokura, "An X-ray-induced insulator-metal transition in a magnetoresistive manganite," *Nature*, vol. 386, no. 10, pp. 813–815, 1997.

[117] J. B. Goodenough, "The two components of the crystallographic transition in vo$_2$," *J. Solid State Chem.*, vol. 3, no. 4, pp. 490–500, 1971.

[118] A. Zylbersztejn and N. F. Mott, "Metal-insulator transition in vanadium dioxide," *Phys. Rev. B*, vol. 11, pp. 4383–4395, Jun 1975.

[119] J.-G. Ramírez, A. Sharoni, Y. Dubi, M. E. Gómez, and I. K. Schuller, "First-order reversal curve measurements of the metal-insulator transition in vo$_2$: Signatures of persistent metallic domains," *Phys. Rev. B*, vol. 79, p. 235110, Jun 2009.

[120] C. Miller, M. Triplett, J. Lammatao, J. Suh, D. Fu, J. Wu, and D. Yu, "Unusually long free carrier lifetime and metal-insulator band offset in vanadium dioxide," *Phys. Rev. B*, vol. 85, p. 085111, Feb 2012.

[121] D. V. Lang, R. A. Logan, and M. Jaros, "Trapping characteristics and a donor-complex (dx) model for the persistent-photoconductivity trapping center in te-doped $al_xga_{1-x}as$," *Phys. Rev. B*, vol. 19, no. 2, pp. 1015–1030, 1979.

[122] G. Nieva, E. Osquiguil, J. Guimpel, M. Maenhoudt, B. Wuyts, Y. Bruynseraede, M. B. Maple, and I. K. Schuller, "Photoinduced enhancement of superconductivity," *Appl. Phys. Lett.*, vol. 60, no. 17, pp. 2159–2161, 1992.

[123] A. Hoffmann, J. Hasen, D. Lederman, T. Endo, Y. Bruynseraede, and I. K. Schuller, "Persistent photoinduced superconductivity," *J. Alloys Compd.*, vol. 251, no. 1, pp. 87–93, 1997.

[124] M. K. Sheinkman and A. Y. Shik, "Long-term relaxation and residual conductivity of semiconductors (review)," *Sov. Phys. Semicond.*, vol. 10, no. 2, pp. 128–143, 1976. [Fiz. Tekh. Poluprovodn. **10**, 209 (1976)].

[125] K. Shibuya, D. Okuyama, R. Kumai, Y. Yamasaki, H. Nakao, Y. Murakami, Y. Taguchi, T. Arima, M. Kawasaki, and Y. Tokura, "X-ray induced insulator-metal transition in a thin film of electron-doped $vo_2$," *Phys. Rev. B*, vol. 84, p. 165108, Oct 2011.

[126] J. Park, E. Lee, K. W. Lee, and C. E. Lee, "Electrical transport and quasipersistent photocurrent in vanadium oxide nanowire networks," *Appl. Phys. Lett.*, vol. 89, no. 18, p. 183114, 2006.

[127] H. Kweon, K. W. Lee, and C. E. Lee, "Photoinduced reentrant insulator-metal-insulator transitions in vanadium oxide nanotubes," *Appl. Phys. Lett.*, vol. 93, no. 4, p. 043105, 2008.

[128] K. W. Lee, H. Kweon, J. Park, and C. E. Lee, "Charge and spin dynamics in vo[sub 2] nanorods," *Appl. Phys. Lett.*, vol. 94, no. 23, p. 233111, 2009.

[129] H. W. Verleur, A. S. Barker, and C. N. Berglund, "Optical properties of $vo_2$ between 0.25 and 5 ev," *Rev. Mod. Phys.*, vol. 40, pp. 737–737, Oct 1968.

[130] P. Boriskov, A. Velichko, A. Pergament, G. Stefanovich, and D. Stefanovich, "The effect of electric field on metal-insulator phase transition in vanadium dioxide," *Tech. Phys. Lett.*, vol. 28, pp. 406–408, 2002.

[131] K. D. Rogers, "An x-ray diffraction study of semiconductor and metallic vanadium dioxide," *Powder Diffr.*, vol. 8, pp. 240–244, 12 1993.

[132] M. M. Qazilbash, M. Brehm, B.-G. Chae, P.-C. Ho, G. O. Andreev, B.-J. Kim, S. J. Yun, A. V. Balatsky, M. B. Maple, F. Keilmann, H.-T. Kim, and D. N. Basov, "Mott transition in $vo_2$ revealed by infrared spectroscopy and nano-imaging," *Science*, vol. 318, no. 5857, pp. 1750–1753, 2007.

[133] M. M. Qazilbash, A. Tripathi, A. A. Schafgans, B.-J. Kim, H.-T. Kim, Z. Cai, M. V. Holt, J. M. Maser, F. Keilmann, O. G. Shpyrko, and D. N. Basov, "Nanoscale imaging of the electronic and structural transitions in vanadium dioxide," *Phys. Rev. B*, vol. 83, p. 165108, Apr 2011.

[134] H. X. Jiang and J. Y. Lin, "Percolation transition of persistent photoconductivity in ii-vi mixed crystals," *Phys. Rev. Lett.*, vol. 64, pp. 2547–2550, May 1990.

[135] D. L. Huber, "Statistical model for stretched exponential relaxation in macroscopic systems," *Phys. Rev. B*, vol. 31, pp. 6070–6071, May 1985.

[136] J. Cao, W. Fan, H. Zheng, and J. Wu, "Thermoelectric effect across the metal-insulator domain walls in $vo_2$ microbeams," *Nano Lett.*, vol. 9, no. 12, pp. 4001–4006, 2009.

[137] S. A. Studenikin, N. Golego, and M. Cocivera, "Carrier mobility and density contributions to photoconductivity transients in polycrystalline zno films," *J. Appl. Phys.*, vol. 87, no. 5, pp. 2413–2421, 2000.

[138] Q. H. Li, T. Gao, Y. G. Wang, and T. H. Wang, "Adsorption and desorption of oxygen probed from zno nanowire films by photocurrent measurements," *Appl. Phys. Lett.*, vol. 86, no. 12, pp. 123117–123119, 2005.

[139] C. C. Kwan, C. Griffiths, and H. Eastwood, "Transport and structural properties of vo2 films," *Appl. Phys. Lett.*, vol. 20, no. 2, pp. 93–95, 1972.

[140] V. I. Kudinov, I. L. Chaplygin, A. I. Kirilyuk, N. M. Kreines, R. Laiho, E. Lähderanta, and C. Ayache, "Persistent photoconductivity in $yba_2cu_3o_{6+x}$ films as a method of photodoping toward metallic and superconducting phases," *Phys. Rev. B*, vol. 47, pp. 9017–9028, Apr 1993.

[141] C. N. Berglund and H. J. Guggenheim, "Electronic properties of $vo_2$ near the semiconductor-metal transition," *Phys. Rev.*, vol. 185, pp. 1022–1033, Sep 1969.

[142] M. Ben-Chorin, Z. Ovadyahu, and M. Pollak, "Nonequilibrium transport and slow relaxation in hopping conductivity," *Phys. Rev. B*, vol. 48, pp. 15025–15034, Nov 1993.

[143] F. Gervais and W. Kress, "Lattice dynamics of oxides with rutile structure and instabilities at the metal-semiconductor phase transitions of $nbo_2$ and $vo_2$," *Phys. Rev. B*, vol. 31, pp. 4809–4814, Apr 1985.

[144] D. V. Lang and R. A. Logan, "Large–lattice–relaxation model for persistent photoconductivity in compound semiconductors," *Phys. Rev. Lett.*, vol. 39, no. 10, pp. 635–639, 1977.

[145] H. X. Jiang, G. Brown, and J. Y. Lin, "Persistent photoconductivity in ii-vi and iii-v semiconductor alloys and a novel infrared detector," *J. Appl. Phys.*, vol. 69, no. 9, pp. 6701–6703, 1991.

[146] M. El Allali, C. B. Sørensen, E. Veje, and P. Tidemand-Petersson, "Experimental determination of the gaas and $ga_{1-x}al_xas$ band-gap energy dependence on temperature and aluminum mole fraction in the direct band-gap region," *Phys. Rev. B*, vol. 48, pp. 4398–4404, Aug 1993.

[147] J. Ye, T. Yoshida, Y. Nakamura, and O. Nittono, "Optical activity in the vacancy ordered $iii_2vi_3$ compound semiconductor $(ga_{0.3}in_{0.7})_2se_3$," *Appl. Phys. Lett.*, vol. 67, pp. 3066–3068, Nov 1995.

[148] R. Friedberg and J. M. Luttinger, "Density of electronic energy levels in disordered systems," *Phys. Rev. B*, vol. 12, pp. 4460–4474, Nov 1975.

[149] J. C. Phillips, "Stretched-exponential carrier relaxation in semiconductors," *Phys. Rev. B*, vol. 52, pp. R8637–R8639, Sep 1995.

[150] G. Beadie, E. Sauvain, A. S. L. Gomes, and N. M. Lawandy, "Temperature dependence of carrier relaxation in semiconductor doped glasses," *Phys. Rev. B*, vol. 51, pp. 2180–2187, Jan 1995.

[151] M. C. Tarun, F. A. Selim, and M. D. McCluskey, "Persistent photoconductivity in strontium titanate," *Phys. Rev. Lett.*, vol. 111, p. 187403, Oct 2013.